Thomas Indlekofer

The dynamic nature of self-excited azimuthal modes in annular combustors

Thomas Indlekofer

Doctoral thesis

Doctoral theses at NTNU, 2021:209

NTNU
Norwegian University of
Science and Technology
Thesis for the degree of
Philosophiae Doctor
Faculty of Engineering
Department of Energy and Process Engineering

■ **NTNU**
Norwegian University of
Science and Technology

■ **NTNU**
Norwegian University of
Science and Technology

■ NTNU

Thomas Indlekofer

The dynamic nature of self-excited azimuthal modes in annular combustors

Thesis for the degree of Philosophiae Doctor

Trondheim, June 2021

Norwegian University of Science and Technology
Faculty of Engineering
Department of Energy and Process Engineering

◻ NTNU
Norwegian University of
Science and Technology

PRINTED IN
NORWAY
NO - 1598

NORDIC SWAN ECOLABEL

Printed matter
2041 0731

Abstract

Hydrogen fired gas turbines can play a vital role in the transition towards a low emission energy sector by providing grid stability and thereby enabling increased penetration of intermittent renewable energies. One of the main factors limiting the operating range of modern gas turbine combustors are thermoacoustic instabilities, which result from a constructive coupling between acoustics, flow and heat release. In modern annular combustors these instabilities are manifested by the propagation of acoustic waves in azimuthal direction which often exhibit a dynamic time-varying nature. This means that the modes can intermittently switch between being of standing nature, thereby having a fixed nodal line position, or of spinning nature, thereby having a nodal line which spins around the annulus at the speed of sound.

The first part of this work uses an existing nominally symmetric atmospheric annular combustion chamber with bluff body stabilized flames. Experiments are performed over a wide range of operating conditions revealing several interesting features of azimuthal combustion instabilities. For a fixed power, the combustor features a supercritical Hopf-bifurcation with an increasing amplitude when the equivalence ratio is increased. The increase in amplitude is accompanied by a characteristic transition from standing to switching and eventually to purely spinning modes. A system of coupled first order differential equations based on a quaternion description of the azimuthal mode, giving a state-space representation of the system, is used to investigate the modal dynamics. The model is fed with parameters extracted by a system identification approach applied to the experimental data and is able to recreate the dynamics of the system. Despite the nominal symmetry of the combustor, two symmetry breaking effects are observed. First,

a rotational symmetry breaking leads to preferred and repeatable anti-nodal line positions of the mode. Second, a spontaneous symmetry breaking effect prevents the mode from switching its spinning direction when the noise is not sufficiently large to allow sporadic escape from the attractor. The calibrated set of equations allows to study a wider parameter space than observed in the experiments and to explore the complete phase space topology of the system which shows unimodal, bimodal, single torus and double tori probability density functions of the state vector.

The second part of the work introduces a novel pressurized annular combustion chamber with swirl stabilized flames, enabling the study of azimuthal instabilities at more realistic boundary conditions and chamber pressures up to 3.5 bar. The combustor features a wide range of instabilities. The dynamics of the instabilities are substantially different from the dynamics observed in the atmospheric combustor as they feature significant harmonic components in the pressure signal and very strong spinning states. The harmonic component is amplitude dependent and a cut-on amplitude is identified along with a quadratic relationship between the harmonic components. While strong harmonic components distort the pressure phase space, the integrated heat release rate can be well described by the fundamental component only. This can be exemplified by the Rayleigh index, which does not change significantly upon inclusion of the higher harmonics. A thorough characterization of the boundary conditions is performed to position the combustor as a benchmark case for numerical simulations.

As a successful bridging technology, gas turbines need to be able to respond quickly to fluctuations in the electricity demand. Hence, dynamic operation is crucial. The third part of this thesis studies the effect of transient operating conditions on azimuthal combustion instabilities in both the atmospheric and the pressurized experimental setup. The dynamic operation is simulated by linearly increasing/decreasing the equivalence ratio for a fixed power. Different types of hysteresis are observed affecting both the amplitudes and nature of the modes and the stable operating range of the combustor.

Preface

This thesis is submitted to the Norwegian University of Science and Technology (NTNU) for partial fulfillment of the requirements for the degree of philosophiae doctor. The doctoral work has been carried out in the Thermo Fluids Group at the Department of Energy and Process Engineering (EPT), from January 2018 to March 2021. The work has been supervised by Professor James R. Dawson and co-supervised by Associate Professor Nicholas A. Worth.

The thesis is made up of four chapters and seven scientific papers. The first three chapters introduce the field and review literature, explain the theory and the experimental setups and diagnostics. The research articles are summarized in Chapter 4, and included in full text at the end of the thesis. The articles are grouped in terms of their topics, with the first two articles reporting a combined experimental/low-order modelling approach investigating an atmospheric annular combustor. The second group consists of three articles presenting experimental investigations of a novel pressurized annular combustor. The last two articles investigate transient operating conditions. A list of the publications with the contributions of the authors is presented in the following:

Article I

Spontaneous and explicit symmetry breaking of thermoacoustic eigenmodes in annular geometries
Thomas Indlekofer, Abel Faure-Beaulieu, Nicolas Noiray, James Dawson
Under consideration for publication in Physical Review Letters.

Author's contributions: Thomas Indlekofer and Abel Faure-Beaulieu performed the experiments together. Thomas Indlekofer evaluated the results, Abel Faure-Beaulieu derived the model and provided post processing routines. Thomas Indlekofer, Abel Faure-Beaulieu and Nicolas Noiray wrote the draft manuscript. James Dawson read and reviewed the manuscript and provided technical and editorial guidance.

Article II

Experiments and low-order modelling of intermittent transitions between clockwise and anticlockwise spinning thermoacoustic modes in annular combustors
Abel Faure-Beaulieu, Thomas Indlekofer, James Dawson, Nicolas Noiray
Proceedings of the Combustion Institute, in press.

Author's contributions: Thomas Indlekofer and Abel Faure-Beaulieu performed the experiments together and evaluated the results, Abel Faure-Beaulieu derived the model and wrote the draft manuscript. Thomas Indlekofer, James Dawson and Nicolas Noiray read and reviewed the manuscript and provided technical and editorial guidance.

Article III

Self-excited longitudinal and azimuthal modes in a pressurized annular combustor
Marek Mazur, Yi Hao Kwah, Thomas Indlekofer, James Dawson, Nicholas A. Worth
Proceedings of the Combustion institute, in press.

Author's contributions: Marek Mazur designed and commissioned the setup. Marek Mazur, Yi-Hao Kwah and Thomas Indlekofer performed the experiments. Marek Mazur analyzed the results and wrote the draft manuscript. Thomas Indlekofer, James Dawson and Nicholas A. Worth read and re-

viewed the manuscript and provided technical and editorial guidance.

Article IV

The effect of hydrogen addition on the amplitude and harmonic response of azimuthal instabilities in a pressurized annular combustor
Thomas Indlekofer, Byeonguk Ahn, Samuel Wiseman, Yi Hao Kwah, Marek Mazur, James Dawson, Nicholas A. Worth
Combustion and Flame, Volume 228, June 2021, Pages 385-387.

Author's contributions: Thomas Indlekofer modified the setup and commissioned it with Samuel Wiseman and Yi-Hao Kwah. Thomas Indlekofer and Byeonguk Ahn performed the experiments together. Thomas Indlekofer analyzed the results and wrote the draft manuscript. James Dawson and Nicholas A. Worth read and reviewed the manuscript and provided technical and editorial guidance.

Article V

The role of fundamental and harmonic heat release rate components in self-excited azimuthal instabilities in a pressurized annular combustor with methane/hydrogen flames
Byeonguk Ahn, Thomas Indlekofer, James Dawson, Nicholas A. Worth
To be submitted to Combustion and Flame.

Author's contributions: Thomas Indlekofer and Byeonguk Ahn performed the experiments together. Byeonguk Ahn analyzed the results and wrote the draft manuscript with Thomas Indlekofer. James Dawson and Nicholas A. Worth read and reviewed the manuscript and provided technical and editorial guidance.

Article VI

The effect of dynamic operating conditions on the thermoacoustic response of hydrogen rich flames in an annular combustor
Thomas Indlekofer, Abel Faure-Beaulieu, Nicolas Noiray, James Dawson
Combustion and Flame, Volume 223, January 2021, Pages 284-294.

Author's contributions: Thomas Indlekofer and Abel Faure-Beaulieu performed the experiments together. Thomas Indlekofer evaluated the results, performed the data analysis and wrote the draft manuscript. Abel Faure-Beaulieu, Nicolas Noiray and James Dawson read and reviewed the manuscript and provided technical and editorial guidance.

Article VII

Transient thermoacoustic responses of methane/hydrogen flames in a pressurized annular combustor
Byeonguk Ahn, Thomas Indlekofer, James Dawson, Nicholas A. Worth
Accepted for publication at ASME 2021

Author's contributions: Thomas Indlekofer and Byeonguk Ahn performed the experiments together. Byeonguk Ahn analyzed the results and wrote the draft manuscript with Thomas Indlekofer. James Dawson and Nicholas A. Worth read and reviewed the manuscript and provided technical and editorial guidance.

Trondheim, 26.03.21

Thomas Indlekofer

Acknowledgements

Reflecting on the last three years, there are many individuals to whom I owe great gratitude and thanks.

First of all, I would like to thank my supervisors, James Dawson and Nicholas Worth, for all the guidance and support I have gotten throughout the last years. Your doors have always been open, and your insights and ideas have been extremely valuable. I would also like to acknowledge Nicolas Noiray who made it possible for me to come to ETHZ for a research stay, and who initiated a very fruitful collaboration.

I appreciate the support of the technical staff and the administration at NTNU, who made it possible for me to focus on academic problems.

I was fortunate to have an amazing group of PhD students and post docs around me who provided a great social and academic environment. Special thanks go to my office mates, Eirik and Håkon, who had no choice but to endure my mood swings, and to Yi Hao, Sam and Luk who shared much of their knowledge and time in the combustion lab with me. Also to Philip and Ben, who never failed to take me out climbing whenever there was too much work to do.

I owe great gratitude to my family and friends in Germany, who I didn't see as much as I wished in the last years.

Finally, I want to thank Anna, for making me feel home in Norway and making the last three years the most enjoyable of my life to this point.

Contents

List of Figures

Nomenclature

The nomenclature describes abbreviations, physical parameters and notation used throughout the introductory part of the thesis. In the individual publications, which are appended at the end of the thesis, the nomenclature might differ slightly.

Abbreviations

1D	1 dimensional
3D	3 dimensional
CCW	Counterclockwise
CH_4	Methane
CO_2	Carbon dioxide
CW	Clockwise
FDF	Flame describing function
FTF	Flame transfer function
GHG	Greenhouse gas
IPA	Intermediate pressure annular
IPCC	Intergovernmental panel on climate change
LES	Large eddy simulation

MFC Mass flow controller

NOx Nitrous oxides

OH* Hydroxyl radical

PMT Photo multiplier tube

Physical parameters

α Acoustic damping

χ Nature angle

ϵ Emissivity

Γ White Gaussian noise

γ Heat capacities ratio

κ Cubic saturation constant

ν Linear growth rate

ω Angular frequency, $\omega = 2\pi f$

ϕ Phase of the FTF

ρ Density

τ Time delay

Θ Azimuthal coordinate

θ Azimuthal position of the anti-nodal line

φ Slowly varying phase of the quaternion formalism

$\xi_{1,2}$ Orthogonal eigenmodes

A Amplitude of the quaternion formalism

a, b, m Calibration coefficients of the hot wire

$A^{+,-}$ Slowly varying amplitude of the spinning mode projection

A_w Hot wire surface

A_{sp} Total amplitude of the spinning mode projection

B Stochastic part

$B^{+,-}$ Downstream and upstream travelling wave in the injector pipe

C C indicator

c Speed of sound

D, d Diameter

E Voltage

F Deterministic part

f Oscillation frequency

f_s Sampling frequency of the microphones

$f_{s,cam}$ Sampling frequency of the high speed camera

H Length of the combustor

h Heat transfer coefficient

$k^{+,-}$ Wave number of the downstream and upstream travelling wave

L_i Damping processes

M Mach number

n Azimuthal mode order

n_c Interaction index in the $n - \tau$ model

P Probability

p Pressure

q Heat release

R Mean radius of the combustor

$S_{i,j}$ Coefficients of the scattering matrix

SR Spin ratio

T Period of the oscillation

t Time

T_r Ramp duration

u Velocity

V Volume

Y Set of slow flow variables

Z Acoustic impedance

$\mathbf{x}$ Position vector $\mathbf{x}=\{x,y,z\}$

CR   Contraction ratio

Notation

$\dots'$ Fluctuating value

$\dot{\dots}$ First time derivative

$\hat{\dots}$ Fourier transform

$\mathcal{H}(\dots)$ Hilbert transform

$\overline{\dots}$ Temporal mean value

i, j, k Quaternion imaginary units

Chapter 1

Introduction

1.1 Background

The first significant advances towards the design of modern gas turbines were made by Franz Stolze in the late 19th century. In his patents and publications, Stolze came up with convincing concepts which had great similarity with the gas turbines in use today. Even though his test plant, built in 1904, failed to generate any power due to the low efficiency of compressor and turbine, gas turbines came to play an important role in todays industry [Eckhardt 2014].

The two major applications of gas turbines are aviation and electric power generation. In 2016 the International Air Transport Association (IATA) expected air travel to double until 2037 [IATA 2016]. Even though the current COVID-19 pandemic led to the largest decline in air travel and current projections don't expect air travel to return to 2019 levels before 2023, the aviation industry is expected to continue growing in the long term [Garrow and Lurkin 2021]. With no alternative propulsion technology in sight for commercial air travel, as well as the compelling combination of fluctuating renewable energy sources with flexible gas turbines, gas turbines are expected to play an important role in the future [Breeze 2019].

According to the reports of the Intergovernmental Panel on Climate Change (IPCC) *"human influence on the climate system is clear and continued emissions of greenhouse gases (GHGs) will cause further warming and changes in all components of the climate system"* [IPCC 2013a]. There is no doubt that GHGs constitute the dominant factor increasing the radiative forcing,
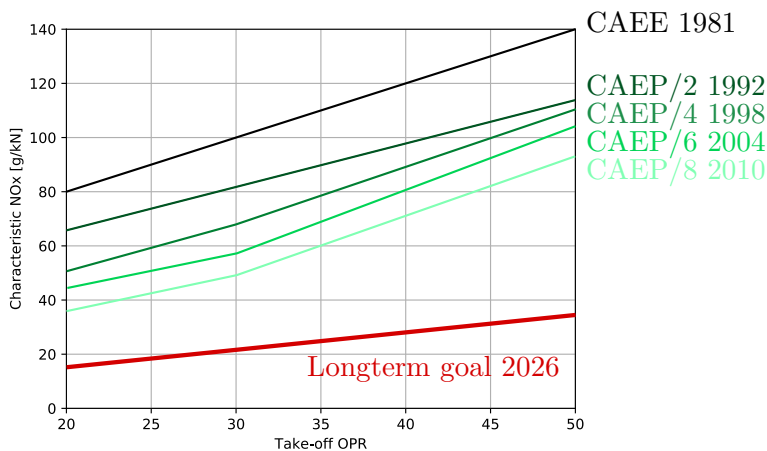
Figure 1.1: Development of NOx emission standards and long term technology goals of aircraft engines imposed by the Committee on Aircraft Engine Emissions (CAEE) and after 1983 by the Committee on Aviation Environmental Protection (CAEP) by the International Civil Aviation Organization (ICAO). Adapted from Dickson [2014].

which quantifies the earth's energy balance. Especially the emission of carbon dioxide (CO_2) but also unburnt hydrocarbons or nitrous oxides (NOx) are driving this change in atmospheric gas composition [IPCC 2013b]. To limit global warming and the related negative effects, strong reductions in emissions are needed.

Gas turbines can emit all of the previously named pollutants, but recent emission regulations focused on NOx reduction, which, in addition to its effect on climate change, is known to cause health issues such as respiratory illness or headaches [EPA 2016]. In terms of aircraft engines, the emissions are regulated by the International Civil Aviation Organization (ICAO) and based on a standardized landing take-off cycle. The development of the the NOx emission standard, described by the emitted NOx per thrust ratio for such a cycle is shown in Fig. 1.1. Similar trends in the NOx emission standards are also in place for land based power generation gas turbines.

While regulators continue to lower emission requirements, gas turbine manufacturers face the challenge to create low emission solutions, while simultaneously maintaining or even improving the efficiency and operability of their engines. A major part of the produced NOx is of thermal origin, meaning that it is a function of the temperature and the residence time [Breeze

2019, Eckhardt 2014]. Therefore, a very effective strategy is to reduce hot spots in the combustion chamber and to decrease the residence time of the hot gases in the combustor. In modern engines, this is achieved by the combustion of lean premixed fuel-air mixtures, relatively close to the lean limit. Therefore, the fuel and air are mixed with excess air before being burned which results in lower temperatures.

Another promising way to reduce GHG emissions is to use carbon-free fuels, e.g. to introduce modest quantities of bio-fuels produced from agricultural products or so called green hydrogen which describes hydrogen produced from renewable energies without emitting GHGs. This conversion is one of the pathways of the *Power-to-X* approach which uses surplus electricity and converts it to be used in another sector, like transport, or simply allows storing it in the form of for example hydrogen or ammonia (see Fig. 1.2). Compared to the storage of electricity in batteries, the storage of large quantities of these fuels is feasible. The produced green hydrogen can be used in several ways. During peak load times or times with little wind or sun, the fuels can be burned in gas turbines to cover the electricity demand. *Power-to-X* is expected to play a major role in the integration of renewable energies and the substitution of fossil fuels which still make up the major part of our energy use [Koj et al. 2019]. Subsequently a lot of effort is put into research and development of relevant technologies

The introduction of hydrogen into the fuel mixture of gas turbine combustors (usually CH_4) can increase the flammability limit and therefore allow lower fuel/air ratios [Bothien et al. 2019]. Other alternatives like syngases or ammonia can have a wide range of characteristics influencing the combustion efficiency and emissions. However, low emission burners are usually designed to operate with a specified fuel and can, if operated outside of the specified conditions, suffer from excess emissions, combustion instabilities or even failure [Nemitallah et al. 2018].

Figure 1.2: *Power-to-X* pathways to decarbonize energy with green hydrogen. Adapted from [sie 2019].

1.2   Combustion instabilities

Self-excited thermoacoustic instabilities constitute one of the main factors limiting the operating range of gas turbines [Poinsot 2017]. These instabilities result from a constructive coupling between acoustics, flow and the fluctuating heat release rate in the combustor.
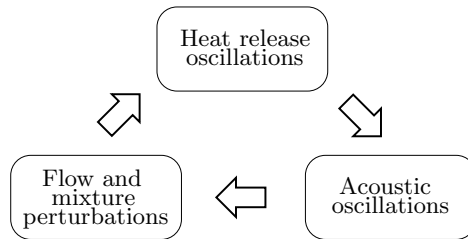
Figure 1.3: Thermoacoustic feedback loop. Adapted from Lieuwen and Yang [2005].

The generic feedback loop behind this phenomenon is shown in Fig. 1.3 and is driven by the unsteady heat release that is generated by turbulent flames in a combustor. The unsteady heat release excites acoustic oscilla-

tions through the expansion of the hot gases. The generated acoustic waves travel in the geometry of the combustor and cause velocity or mixture fluctuations which affect the heat release and close the feedback loop [Lieuwen and Yang 2005].

The most prominent occurrence of combustion instabilities was during the race for the first manned mission to the moon. During the development of the F-1 engine for the Apollo program, of which five were used to power the first stage of the launch, significant challenges due to high-frequency oscillations had to be faced. The need to eliminate them and to enhance the level of fundamental understanding initiated an enormous research program during which more than 2000 full-scale tests were conducted until the engine eventually received the qualification for manned missions [Oefelein and Yang 1993].

Even though the endeavour during the development of the F-1 engine might be the most prominent case of combustion instabilities, the phenomenon has been known for a long time. In 1878, the well known Rayleigh criterion [Lord Rayleigh 1878]

$$\int p'(t)q'(t)dt > 0 \qquad (1.1)$$

was stated. It describes the correlation of the heat release oscillations q' and the pressure oscillations p', and is positive if the phase difference between the respective oscillations is below $\pi/2$. In that case the heat release is increasing the net energy of the acoustic field [Chu 1965, Nicoud and Poinsot 2005]. The Rayleigh criterion was also derived and interpreted in the frequency domain and its sensitivity investigated through adjoint analysis [Magri et al. 2019]. In general, the criterion emphasizes the importance of time lags in the field of combustion instabilities. Time lags were found to be critical in combustion instabilities occurring in the development of rocket engines in the 1950s [Crocco 1951, Crocco et al. 1960]. To relate the heat release rate fluctuation $\dot{q}'$ to an incident velocity perturbation u', Crocco and Cheng [1956] formulated the well-known $n - \tau$ model $\dot{q}' = n_c u'(t - \tau)$, where n_c describes the interaction index and τ a time delay. Thinking in terms of the Rayleigh criterion, τ controls the phase relationship between the heat release rate and the acoustics, and thereby controls the Rayleigh index.

While this model is still relevant today, it constitutes only a very rough approximation for flames in gas turbine combustors whose response is strongly dependent on the frequency [Candel 2002]. Flames tend to act as a low pass filter and damp out high-frequency disturbances while they are more sensitive to low-frequency disturbances [Schuller et al. 2020]. The cut-off

frequency is governed by the flame length and the flow velocity. Nowadays, the flame response is characterized by the flame transfer function (FTF) [Ducruix et al. 2000, Lieuwen 2003, Schuller et al. 2020]

$$\text{FTF}(\omega) = \frac{\hat{q}'(\omega)/\overline{q}}{\hat{u}'/\overline{u}}, \tag{1.2}$$

which is dependent on the angular frequency ω. The hatted quantities $(\cdot\hat{\cdot})$ thereby describe oscillations in frequency space while the overbar $(\overline{\cdots})$ describes a temporal mean. It can be retrieved theoretically [Dowling 1999, Schuller et al. 2003], numerically [Jaensch et al. 2018] or most commonly through experiments [Æsøy et al. 2020, Bellows et al. 2007, Hirsch et al. 2005, Kim et al. 2010, Schuller et al. 2003]. However, while the FTF is independent of the forcing level $\hat{u}/\overline{u}$ for low amplitudes, it saturates for large amplitudes due to non-linear effects. The FTF can be extended to the Flame Describing Function (FDF) [Noiray et al. 2008]

$$\text{FDF}(\omega, \hat{u}'/\overline{u}) = \frac{\hat{q}'(\omega, \hat{u}'/\overline{u})/\overline{q}}{\hat{u}'/\overline{u}}, \tag{1.3}$$

which adds an amplitude dependence. Figure 1.4 shows experimental measurements of FTFs for different forcing levels. Several interesting features can be deduced from the figure: First, the transfer function of premixed flames is unity at zero frequency as this corresponds to a slow change in fuel flow rate and therefore heat release rate [Polifke and Lawn 2007]. Second, the response of the heat release depends on the forcing level which shows the saturation of the heat release fluctuations for large amplitudes. Also, one notes the earlier mentioned low pass filter of the flame as the response drops significantly for higher frequencies. The reason for this lies in the decrease of convective compactness for increased frequencies, leading to destructive interference along the flame front [Ducruix et al. 2000].

The right side of Fig. 1.4 shows the phase which evolves in a quasi linear fashion. This is related to the time lag between a velocity perturbation at the reference position and the response of the flame, which is controlled by the flame length and the flow velocity. For one forcing level this time lag is usually constant, which results in a phase lag that depends linearly on the frequency $\phi = \omega\tau_c$ [Noiray et al. 2008]. However, the time lag can be affected by the forcing level.

In combination with acoustic networks these flame response descriptions can be used to determine the linear stability of a combustor (if using a FTF) and even the limit cycle behavior if the FDF framework is used [Han et al. 2015, Laera et al. 2017].
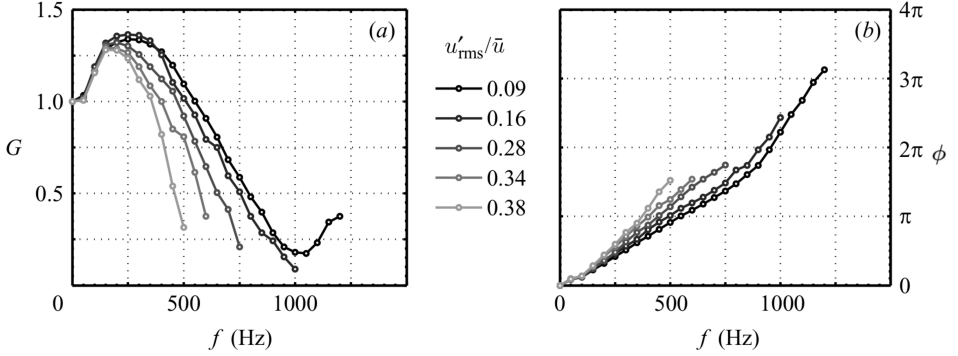
Figure 1.4: Experimental flame transfer functions for different forcing levels. (a) Gain G and (b) Phase ϕ. Adapted from Noiray et al. [2008].

Taking one step back, one has to note that the Rayleigh criterion is only necessary, as it exclusively evaluates the driving of the system through the interaction of the acoustics and the heat release. However, the driving component also has to overcome the damping components, which exist in every combustor and keep the combustor stable if they are large enough. Zinn and Lieuwen [2005] summarize this statement as

$$\underbrace{\int_V \int_T p'(x,t)q'(x,t)dtdV}_{\text{Driving}} > \underbrace{\int_V \int_T \sum L_i(x,t)dtdV}_{\text{Damping}} \qquad (1.4)$$

where V, T, L_i are the volume of the combustor, the period of the oscillations and the different processes constituting the acoustic losses of the system. In gas turbine engines there are several sources of damping like losses through the inlets and outlets of the combustor, the sound absorbing effect of cooling holes [Hughes and Dowling 1990], passive control techniques which include perforated plates and Helmholtz resonators [Bellucci et al. 2004, Dupere and Dowling 2005] or quarter-wave tubes which are typically used to damp certain critical frequencies in a narrow band.

The thermoacoustic stability of combustors tends to be decreased when operated in the lean-premixed regime. The two dominant reasons for this are the reduced acoustic damping by removing secondary air inlets and the increased sensitivity of lean flames towards perturbations [O'Connor et al. 2015]. Inducing pressure and velocity oscillations, thermoacoustic instabilities are highly unwanted as they can result in severe mechanical oscillations and thermal stresses or increased blow off or flashback risk and thereby eventually lead to catastrophic failure of the gas turbine [Poinsot

2017]. An example of the damage by instability induced flashback in a model annular gas turbine combustor is shown in Fig. 1.5 where longitudinal oscillations led to a penetration of the flame into the injector and the flame eventually anchored downstream of the swirler where it melted the bluff bodies.

Figure 1.5: Damaged bluff bodies that were subject to instability induced flashback in a pressurized model annular combustor [Mazur et al. 2020].

Receiving air by the compressor, a gas turbine combustion chamber usually has multiple burners arranged around the central axis of the engine and their shared exhaust feeding the turbine. Nowadays annular combustion chambers are the most common among modern gas turbine engines [Jansohn 2016]. In contrast to other combustor types, annular combustors have only one liner instead of one liner per burner. This leads to a homogeneous temperature exit profile (reducing NOx emissions) and a compact design with the better thrust to weight ratio which is crucial for aero engines [Lefebvre and Ballal 2010].

Self-excited oscillations manifest themselves as pronounced peaks at the resonance frequency of the combustor. These resonance frequencies can be associated with any of the three-dimensional eigenfunctions of the combustor geometry. As the perimeter of an annular combustor can be in the order of its length [Poinsot 2017], unstable azimuthal modes exist in the same frequency range as longitudinal modes. However, azimuthal modes feature several characteristics that differentiate them from longitudinal modes. They induce non-axisymmetric perturbations on the flow [Æsøy et al. 2021] and on the flame [O'Connor et al. 2015]. Also, the nature of the mode can change instantaneously from spinning to standing or vice versa. Over the last decade, the nature of azimuthal modes has received significant atten-

tion from the scientific community and is continuing to do so. Even though they have been observed in industrial engines early this century [Krebs et al. 2002], experimental results were not reported until quite recently [Bourgouin et al. 2013, Worth and Dawson 2013a,b]. To improve our fundamental understanding of the phenomenon of azimuthal combustion instabilities and to validate theoretical and numerical investigations further experimental work is needed. This is where the motivation for this work stems from.

1.2.1   Combustion instabilities in annular combustors

Nowadays, a wide range of tools to study combustion instabilities is available. An overview is given in Fig. 1.6 and differs between modelling and experimental approaches. Full engine tests are extremely costly and the gathered data is usually confidential. Experiments allow the replication of fragments of real engines and the investigation of specific phenomena in a controlled environment. In combination with low-order models or theory, experiments are a powerful approach to improve our understanding of combustion instabilities in annular combustors.

Recently several reviews relevant to this thesis have been published. The author would like to emphasize the detailed work by O'Connor et al. [2015] on transverse combustion instabilities which also includes annular combustors, the work by Poinsot [2017] targeting the prediction and control of combustion instabilities in real engines and the book by Lieuwen and Yang [2005] that gathers experiences made by companies in the early years of this century. Even though all of these works touch the topic of this thesis, none solely focuses on annular combustors. Two reviews that focus on annular geometries are the review about theoretical and analytical investigation of combustion instabilities by Bauerheim et al. [2016] and the work on combustion dynamics of annular systems by Vignat et al. [2020]. However, many developments have been made over the last few years that have not been covered by the previously named works, specifically concerning modal dynamics of azimuthal combustion instabilities. This introduction aims to review the literature concerning azimuthal combustion instabilities, and puts the emphasis on modal dynamics and mode selection.

1.2.2   Early work

The drive to reduce emissions of gas turbines exposed combustion dynamics as a critical area of research in the 1990s [Hsiao et al. 1998]. However, corporate confidentiality and the absence of lab scale experimental setups meant the complexity of combustion instabilities in annular geometries were
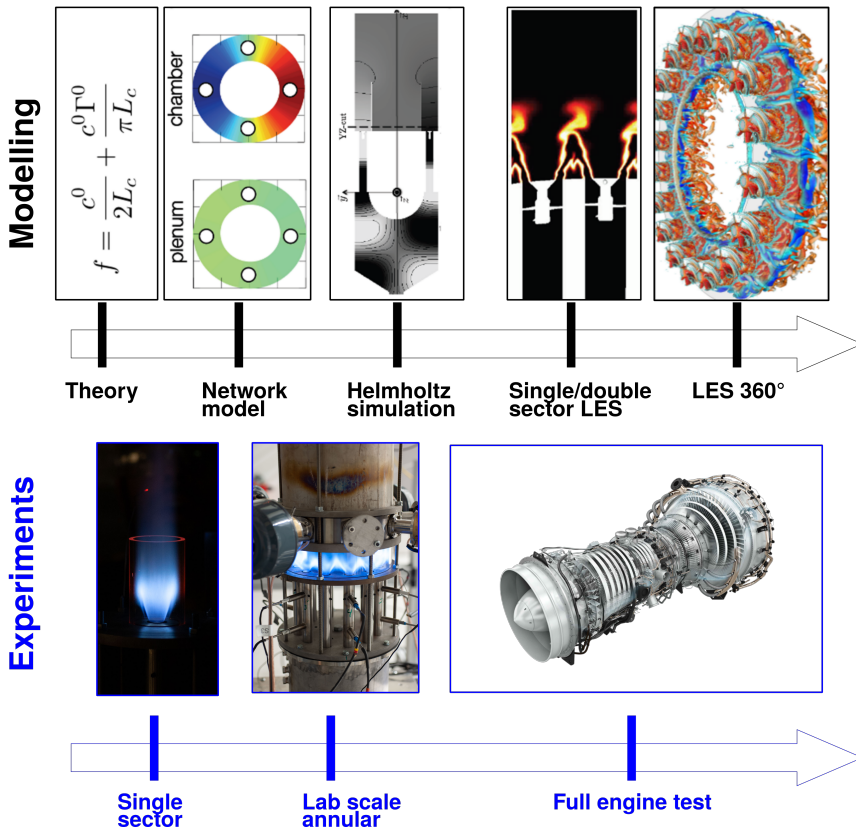
Figure 1.6: Overview of methods and tools to investigate and predict combustion instabilities. The top part of the image shows modelling approaches and is adapted from Bauerheim et al. [2016]. The bottom shows experimental investigations: From left to right the figures show laboratory single-sector [Æsøy et al. 2020] and annular combustors [Nygård et al. 2019] as well as a Siemens SGT-A35 RB industrial engine.

merely understood. It was not until Siemens started reporting on their experiences after introducing an annular combustor in their 3A series [Krebs et al. 1999, 2002, Seume et al. 1998] that the number of investigations started to increase. In their work, the burner time lag was identified as a crucial parameter of thermoacoustic stability [Krebs et al. 1999]. Based on this finding, Siemens reacted by mounting a cylindrical extension to the standard burner (which was originally not developed for the annular configuration) and was thereby able to increase the time lag, resulting in an extension of the thermoacoustically stable operating envelope by 10 % [Krebs et al. 2002].

During the first years of investigation of annular combustion chambers, the focus was primarily on methods to damp combustion instabilities when they arose. This gave rise to the development of active control strategies [McManus et al. 1993, Seume et al. 1998], which consist in the continuous perturbation of combustion parameters to suppress resonant oscillations. However, those approaches proved to be costly and too complex to certify especially for aero applications. This led to a modified approach that consists of building engines that are stable by design and a wide use of Helmholtz resonators, rather than controlling the oscillations [Poinsot 2017]. Therefore the scientific understanding had to be improved, which sparked renewed interest in this topic.

1.2.3   Modal dynamics

An astonishing feature is the transient behavior of the acoustic modes observed in annular combustors. This was not seen in single-sector tests of lab flames which focused on longitudinal modes. In contrast to longitudinal modes, azimuthal waves can travel around an annulus periodically as there are no acoustic boundary conditions in the azimuthal direction. This leads to the existence of clockwise (CW) and counterclockwise (CCW) waves whose nodal lines rotate around the combustor with the speed of sound. Due to the azimuthal symmetry, standing, spinning and mixed modes, which constitute combinations of a standing and a spinning mode, can be excited and we currently cannot predict them. The different states of the modes will hereafter be referred to as the nature of the mode.

In the strongly turbulent and noisy environment of an annular combustor, these modes were found to transition spontaneously or periodically between different states even if the operating conditions were kept constant. The transient nature of azimuthal combustion instabilities, which is usually described as *modal dynamics*, was first observed in industrial engines [Krebs et al. 2002] and then confirmed by LES [Wolf et al. 2012]. Eventually, two lab scale annular combustors [Bourgouin et al. 2013, Worth and Dawson 2013a,b], which are shown in Fig. 1.7, were introduced and allowed experimental investigations of the phenomenon. The two combustors were developed independently and were shown to exhibit self-excited azimuthal modes. The MICCA combustor was also shown to excite both longitudinal modes and the slanted mode, which describes the excitation of a longitudinal and an azimuthal mode with the same frequency at the same time [Bourgouin et al. 2015]. A pressure time series illustrating continuous transitions between standing and spinning modes is shown in Fig. 1.8.
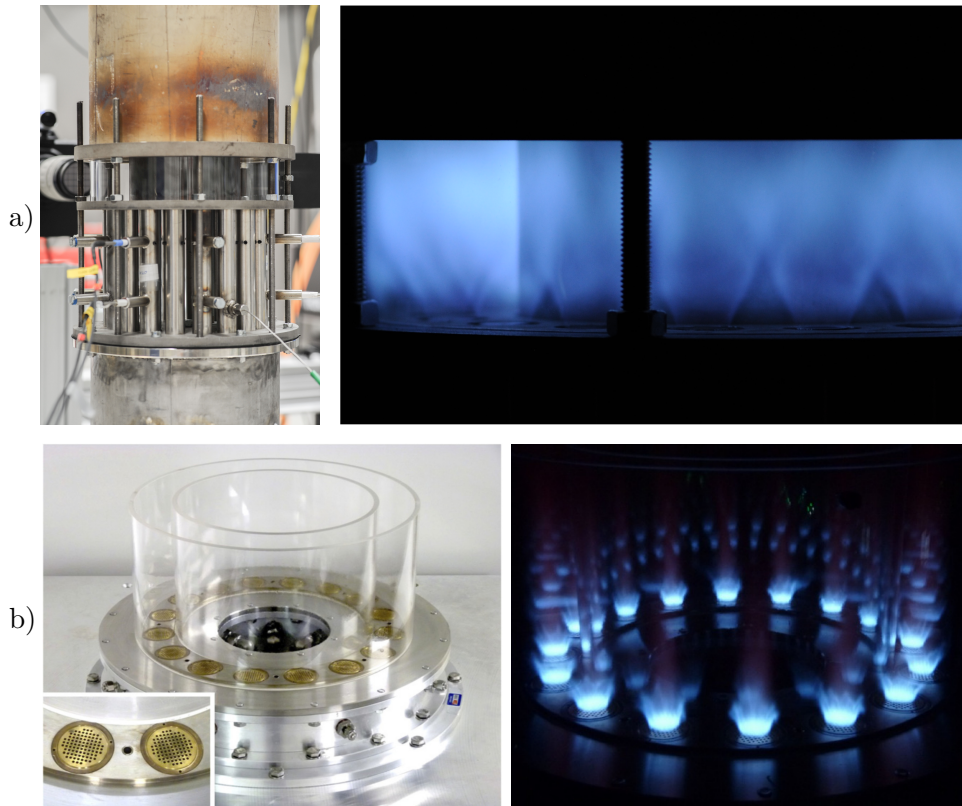
Figure 1.7: The atmospheric annular combustor at NTNU [Worth and Dawson 2013a,b] in a) and the MICCA combustor at EM2C [Bourgouin et al. 2013] with matrix injectors in b) which were the first annular lab-scale combustors to exhibit self-excited azimuthal thermoacoustic instabilities.
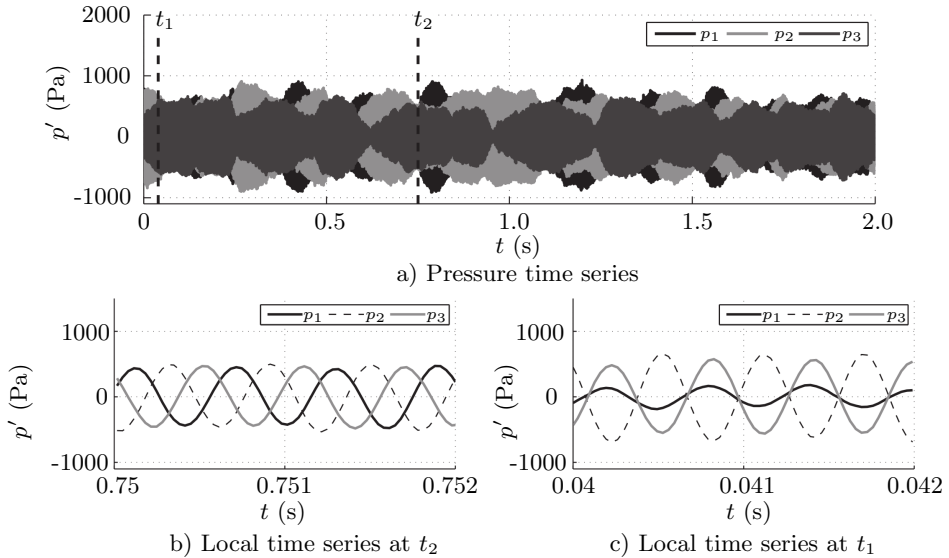
Figure 1.8: Pressure time series measured at $0, 120, 240°$ and the same axial location. The time series illustrates continuous transitions between spinning and standing states. (a) Shows a full 2 s interval. (b) and (c) show local time-series at t_2 and t_1 corresponding to a spinning and a standing mode. The figure is adapted from Worth and Dawson [2013a].

Noise

In reality, gas turbine engines constitute a highly noisy environment due to turbulent combustion. Theoretically it has been shown that the random forcing of the noise influences azimuthal combustion instabilities in two main ways [Faure-Beaulieu and Noiray 2020, Ghirardo and Gant 2019, Noiray and Schuermans 2013].

Firstly, the background noise leads to stochastic trajectories in the phase space with transitions between different mode states as discussed earlier. Therefore, even though modes are usually described as for example standing or spinning, azimuthal combustion instabilities actually exhibit statistically preferred modes which linger around a certain state. This has been shown by Worth and Dawson [2013a] who investigated a lab scale annular combustor experimentally. Figure 1.9 compares the joint probability density functions of two cases. On the left side, one identifies a stochastic distribu-

tion around a standing and a spinning/mixed state which the mode switches between if all swirlers are oriented in the same way. If the combustor is alternately equipped with CW and CCW swirlers the combustor features a stochastic distribution around a standing mode. Similar distributions were also reported and reproduced with a set of nonlinear differential equations for industrial engines [Bothien et al. 2015, Noiray and Schuermans 2013].
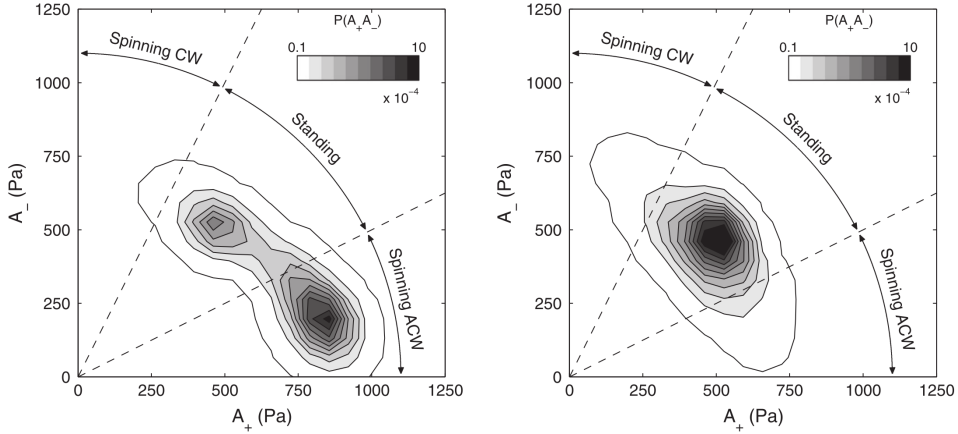
Figure 1.9: Joint PDFs of the mode state in terms of the wave amplitudes of the CW (A_+) and ACW (A_-) spinning waves in a modal annular combustor. Left side: ACW swirlers. Right side: Alternating swirl. Figure adapted from Worth and Dawson [2013a].

Secondly, background noise pushes the mode away from spinning states. With an increasing ratio of the noise intensity to the amplitude of the instability, the attractors of the system transition from spinning, to mixed and eventually to standing modes [Ghirardo and Gant 2019]. This finding is supported by observations of azimuthal combustion instabilities in the lab scale combustor at NTNU/UCAM [Mazur et al. 2019, Worth and Dawson 2013b] and the MICCA combustor equipped with swirl-stabilized flames [Bourgouin et al. 2013] or more recently spray flames [Vignat et al. 2019]. Those combustors show a preference towards standing or mixed modes for low amplitude instabilities. In contrast, the MICCA combustor with matrix burners featuring laminar flames and subsequently a low level of noise features both standing and strongly spinning modes with very little variation around the attracted state [Bourgouin et al. 2014, Laera et al. 2017]. Conclusively one can say that theoretical approaches compare well with experiments, keeping in mind that currently no parametric studies of azimuthal modes with changing noise levels are available [Ghirardo and Gant

2019].

Symmetry breaking effects

The introduction of asymmetry into the combustor through different burners [Morgans and Stow 2007, Parmentier et al. 2012] or fuel staging [Bothien et al. 2015, Schuermans et al. 2003] was investigated in several publications. It was found that equipping an industrial engine with burners with a different FTF can lead to a significant reduction of the oscillations [Berenbrink and Hoffmann 2000].

Noiray et al. [2011] used a dynamical system based on coupled Van der Pol oscillators to investigate the dynamic nature of azimuthal modes theoretically. A wave equation was combined with a Galerkin approach (pressure field expanded in a series of orthogonal basis functions of standing modes) and a nonlinear cubic saturation model describing the heat release. Asymmetry was introduced through a variation of the linear gain along the annulus. This resulted in a nonlinear model of a 1D waveguide describing the modal dynamics if one azimuthal mode is dominant. If the asymmetry vanished, the mode was of spinning nature, while increasing asymmetry leads to mixed and eventually standing modes. Similar results were reported by Hummel et al. [2017a,b] who projected the eigenmodes in the annulus on CW and CCW spinning modes. This shows some agreement with experimental investigations which investigated the effect of alternating swirlers [Worth and Dawson 2013a] and baffles [Dawson and Worth 2015] in a model annular combustion chamber. Both modifications locked the nodal line of the mode and promoted standing modes, while the introduction of three or more baffles also led to damping of the amplitude.

One has to note that asymmetries can be as subtle as manufacturing tolerances which makes it impossible to study a *perfectly* symmetric combustor experimentally. A further complication arises from the initial conditions. In a symmetric annular combustor, the geometry is periodic, so counter propagating azimuthal waves with the same wavelength have no prescribed phase relationship. Therefore, any observed preferred orientation of the nodal line indicates that small asymmetries are present which may be due to non-uniform geometry or flow conditions that can be induced through manufacturing tolerances [Ghirardo et al. 2016, Noiray and Schuermans 2013]. These asymmetries lead to differences in air and fuel flow which affect the flame response. An example can be found in the experimental study on the nominally symmetric laboratory annular combustor at NTNU without swirlers [Mazur et al. 2019], which nonetheless features predominant and

repeatable nodal line positions and mode states. Similar results in terms of the predominance of certain nodal line positions have been shown with laminar flames [Bourgouin et al. 2014].

Another type of asymmetry can be introduced by the flow, for example through swirled injectors. Swirled combustion is a common approach to reduce flame length and improve the flame stability in gas turbine combustors [Syred and Beér 1974] but it also induces a mean azimuthal velocity. This break in reflectional symmetry splits the degenerate eigenvalues of a symmetric case into two counter-rotating modes [Humbert et al. 2020] whose frequencies and linear growth rates might differ [Bauerheim et al. 2014, 2015, Crawford and Knobloch 1991]. If the eigenvalue is split, the spinning mode rotating against the swirl direction was found to be the dominant mode until a critical Mach number is overcome and it becomes the only solution [Faure-Beaulieu and Noiray 2020]. In general, swirl is found to increase the damping [Humbert et al. 2020] which usually reduces the amplitude of the self-excited oscillations.

Ghirardo et al. [2020] identify another symmetry breaking mechanism affecting azimuthal combustion instabilities which is based on recent experimental investigations by Nygård et al. [2019]. In an acoustically forced annular combustor equipped with swirl burners, the flame response was observed to be stronger for CCW spinning modes than for CW spinning modes. The dependence on the spinning direction of the mode manifested in a larger amplitude for the CCW spinning mode. An explanation for this was found in the transverse forcing which an azimuthal mode induces onto a flame and whose direction relative to the swirl leads to a redistribution of the heat release in the annulus and subsequently a differing heat release response. Subsequently Nygård et al. [2021] introduced an azimuthal FDF which highlights the different flame responses in dependence of the spinning direction of the mode in an annular combustor. It is argued that this effect is linked to the use of swirl and the finite curvature and width of the annulus and should therefore not apply for symmetric flames without swirl.

Transverse forcing

The flame response depends on the position of the flame in the acoustic field in the annulus. At a pressure antinode, the flame is not excited transversely and responds in an axisymmetric way, while it responds asymmetrically at the velocity antinode [Worth and Dawson 2013a,b]. Several experimental investigations of single-sector test rigs mimicking a sector of an annular combustor have investigated the effect of transverse forcing [Hauser et al.

2010, O'Connor and Lieuwen 2011, 2012, Saurabh and Paschereit 2013, Saurabh et al. 2014] which remains a topic under discussion.

A systematic review of transverse oscillations can be found in [O'Connor et al. 2015] and concludes that in most cases the dominant heat release oscillations are caused by indirect axial flow disturbances induced by the transverse wave motions. It is therefore common to exclude the effect of the transverse acoustic velocity in modelling approaches for premixed flames which is a good approximation for small amplitudes or spinning modes [Acharya and Lieuwen 2014, Acharya et al. 2012, Ghirardo et al. 2016]. While it usually does not affect the linear stability, it was shown that the transverse acoustic oscillations can have an effect on the modal dynamics of an annular combustor which are dominated by nonlinear dynamics. Ghirardo and Juniper [2013] show that even a symmetric annular combustor can display stable spinning solutions through the influence of the transverse excitation on the nature of the mode in contrast to other works which do not include transverse excitation [Hummel et al. 2017a, Noiray and Schuermans 2013, Paschereit et al. 2006].

However, recent investigations by Saurabh and Paschereit [2017, 2018] who used a setup where a flame can be forced by axial and transverse speakers individually, renewed the interest in transverse forcing. They show that the phase difference between an axial and a transverse perturbation, which in an annular combustor is dependent on the nature and nodal line position of the mode, is a critical parameter to describe the flame response for swirled flames. Therefore, Saurabh and Paschereit [2018] conclude that flame response studies need to be revised and include transverse forcing for technical flame configurations with swirl.

1.2.4   Dynamic operation of gas turbine combustors

With the increasing exploitation of intermittent renewable power sources, gas turbines face the need to provide grid stability through dynamic operation (varying load). However, the occurrence of combustion instabilities under transient operating conditions has received little attention until recently, when several investigations on single-sector setups were reported.

Knoop et al. [1997] investigated a dump combustor for different equivalence ratios. Hysteresis, which describes the dependence of the state of a system on its history and which can occur when a bifurcation parameter is changed (in this case the equivalence ratio), was exploited by means of active control and showed potential to increase the operating limits of the combustor. In

the hysteresis region, two states, a low and high amplitude state, were observed depending on the operating history of the combustor. By injecting a short pulse of secondary fuel, a transition to the low amplitude state was caused, demonstrating a possible control method for combustion instabilities.

In an afterburner, increasing the rate of change of the air flow rate during dynamic operation lead to an earlier onset of instability [Manikandan and Sujith 2020]. Bonciolini et al. [2019a] investigated a swirl stabilized laboratory combustor which for intermediate equivalence ratios featured a large amplitude instability. This situation is quite common for combustion chambers as they usually only feature instabilities for a limited set of operating conditions, while they remain stable otherwise. By investigating different ramp speeds, they revealed that it is possible to bypass the instability island and remain below a critical amplitude level for sufficiently fast equivalence ratio ramps (see Fig. 1.10), displaying a possible operating strategy for real gas turbines. Thermal effects also affected the system response under transient load [Bonciolini et al. 2019b].
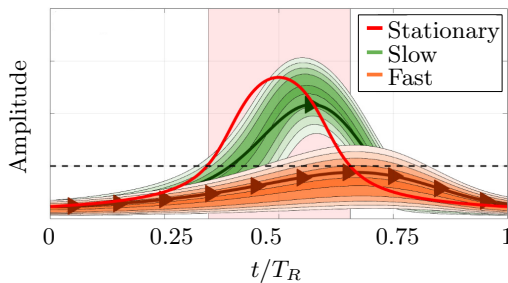
Figure 1.10: Possibility of dodging large amplitude instabilities through fast changes of the bifurcation parameter [Bonciolini et al. 2019a].

The first investigation of transient operation in an annular combustor was reported by Prieur et al. [2017] on the matrix burner configuration of the MICCA combustor at EM2C. Hysteresis was shown to alter the stability map of the combustor, which was manifested by the occurrence of a dual mode region where the nature of the excited mode depended on the initial conditions. Starting from rich operating conditions the combustor featured a chugging mode until it eventually settled into a standing mode, while it settled into a spinning mode if the initial operating condition was lean. The chugging mode could be used as a precursor as the trajectories in phase space already indicated the arising mode's nature. Recently, the characteristics of the dynamical states when a combustor becomes unstable were investigated

in a similar experimental setup [Roy et al. 2020, Singh et al. 2020] but with turbulent flames. It has to be noted that this combustor only features longitudinal modes. The combustor underwent two bifurcations when the equivalence ratio was ramped. The first one occurred from stable to low amplitude unstable via a state of intermittency and the second one occurred to the high amplitude instability. The authors quantify the synchronization of the flames and show that the flames feature significant phase difference during instability in the intermittency regime while the flames are perfectly synchronized at maximum amplitude.

1.3 Research goals

Recent years brought significant progress in our understanding of azimuthal combustion instabilities. Nonetheless, several aspects are still not understood or even investigated. The aim of this thesis is to tackle some of these aspects through experimental investigations in combination with low-order modelling:

i Modal dynamics have been under investigation for several years but a detailed analysis for a range of stationary operating conditions from linearly stable to self-excited thermoacoustic modes has not been reported before. Therefore, experiments over a wide range of operating conditions have been performed in a laboratory annular combustor. An existing low order model is calibrated with the experimental data to investigate the modal dynamics from a state space perspective.

ii Real engines operate at high pressures and power densities. Most available laboratory annular combustors operate at atmospheric conditions and feature complex boundaries which are troublesome for numerical simulations. Therefore, this work introduces a pressurized annular combustor which enables the investigation of azimuthal combustion instabilities at more realistic operating conditions.

iii The effect of dynamic operation on combustion instabilities has received little attention so far, despite the importance of flexible gas turbines to stabilize the future electric grid which is expected to feature a major share of renewable fluctuating energies. Therefore, this work aims to investigate the modal dynamics and hysteresis phenomena in a laboratory combustor subject to azimuthal combustion instabilities. The effect of operating conditions such as ramping speed or power will be assessed along with the effect of transient operation on the stability borders.

iv The push towards zero carbon fuel is important and its effect on azimuthal combustion instabilities is studied through the introduction of highly reactive hydrogen into the fuel mixture.

Chapter 2

Theory

This chapter introduces basic theory of thermoacoustic instabilities in annular combustion chambers, and indicators that are commonly used to describe azimuthal modes.
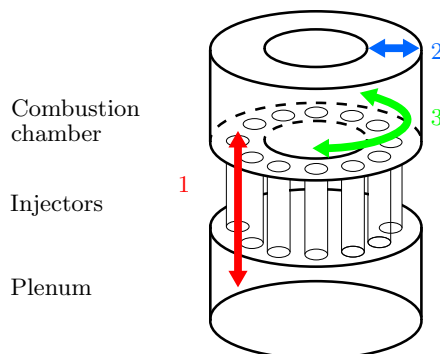
Figure 2.1: Schematic of an annular combustor with possible mode shapes, (1) longitudinal, (2) radial and (3) azimuthal.

In Fig. 2.1 a schematic of an annular combustor similar to the laboratory annular setups is presented. Three different mode shapes can be expected in an annular geometry:

- Longitudinal modes (red), inducing perturbations along the direction of the rig.

- Radial modes (blue), inducing perturbations in radial direction.

- Azimuthal modes (green), inducing perturbations along the circumference on which the burners are arranged, and on which we focus in this work.

In reality, the observed mode shapes are often coupled modes. An example of a self-excited mode observed in the lab-scale combustor is shown on the left side of Fig. 2.2. The plotted data corresponds to the mode shape predicted by an acoustic solver [JulHoltz et al.] which is in good agreement with the experimental data (see supplemental material in [Indlekofer et al. 2021b]). The mode is a coupled azimuthal/longitudinal mode. One notes that the maximum amplitude is reached in the injector pipes and that the amplitude drops towards the atmospheric exit.
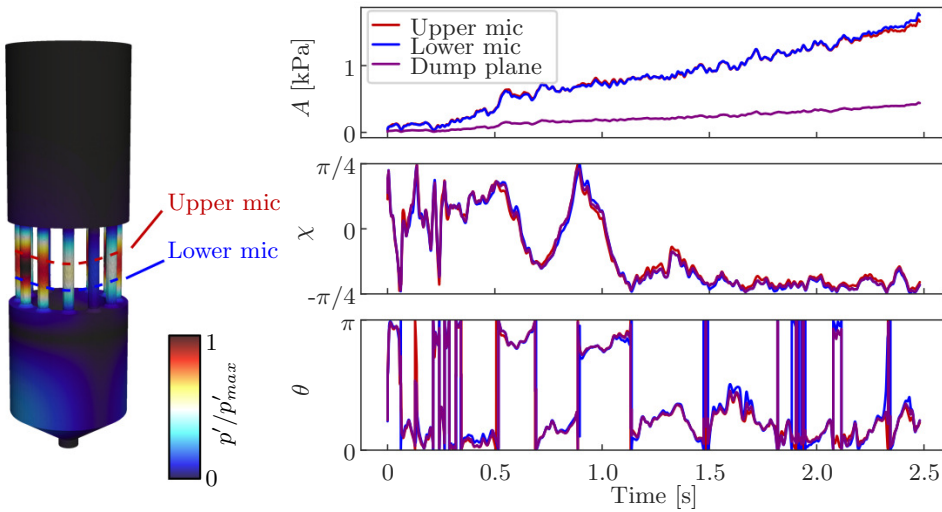
Figure 2.2: Left side: 1A2L mode in the annular atmospheric combustor. Dashed lines indicate the axial positions of the upper and lower microphones. Adapted from [Indlekofer et al. 2021b]. Right side: State of the mode during an equivalence ratio ramp described by the quaternion representation which is introduced in Section 2.2.1: The amplitude (A) of the mode differs depending on the axial position but the nature (χ) and the anti-nodal line position (θ) are the same. Refer to Sect.2.2.1 for a definition of the mode indicator used in this figure.

One will note in the description of the experimental setups (see Chapter 3), that all the pressure measurements are performed in the injector pipes and not in the combustion chamber, to shield the microphones from hot gases. However, the azimuthal mode at the location of the microphones and at

the dump plane are only separated by a complex impedance Z. Therefore, the amplitude and phase of the mode in the combustor might change, but the nature of the mode does not. For most of the investigations in this thesis, it is therefore sufficient to describe the azimuthal mode at the axial location of the microphones as modal dynamics, where mostly the nature and orientation of the mode are of interest, are studied. This is shown on the right side of Fig. 2.2, which compares the nature of the azimuthal mode at different positions. While the amplitude A varies, the nature angle χ (which defines whether the mode is standing or spinning) and the azimuthal position of the anti-nodal line θ are unchanged. The indicators used here are described in detail in 2.2.1.

While the propagation of the pressure to the dump plane is not necessary to study the modal dynamics, it is necessary if the aim is to study the dynamics of the flame. Therefore the next section aims to introduce the calculation of the acoustic field in the injector pipe, before the calculation of the azimuthal mode is introduced in the following section.

2.1   Acoustic mode in the injector

To propagate the pressure, one calculates the acoustic field in the injector where the swirler can be taken into account through a scattering matrix approach as it has a strong effect at high frequencies. Although the approach
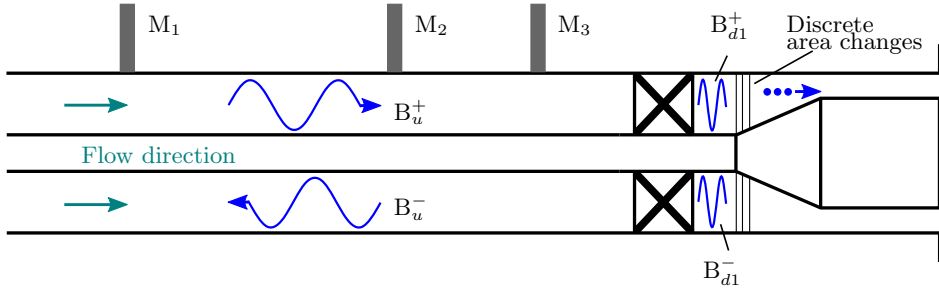
Figure 2.3: Calculation of the acoustic field in the injector pipe. The grey boxes represent the microphones (M_1-M_3) at three axial positions in the IPA injector.

is outlined for an injector with swirlers mounted in the following, it also translates well to the atmospheric annular combustor, which does not feature swirlers in the experiments studied in this thesis (see Chapter 3). The acoustic field in the injector is approximated as a 1D plane wave because it is long compared to its diameter. First, the domain is split up in several

segments. The acoustic field in the first segment, upstream of the swirler, is described by

$$p'(z,t) = \mathbb{R}\{(B_u^+ \exp(-ik^+z) + B_u^- \exp(ik^-z)) \exp(i\omega t)\} \qquad (2.1)$$

$$u'(z,t) = \mathbb{R}\{\frac{1}{\rho c}(B_u^+ \exp(-ik^+z) - B_u^- \exp(ik^-z)) \exp(i\omega t)\}, \qquad (2.2)$$

where B_u^+ and B_u^- describe the complex amplitudes, k^+ and k^- the wave numbers of a downstream and upstream travelling wave respectively, $\omega = 2\pi f$ the angular frequency and ρ the fluid density. The wavenumbers are given by

$$k^\pm = \frac{\omega/c}{1 \pm M} \qquad (2.3)$$

where M is the Mach number. The amplitudes are calculated with the multiple microphone method [Seybert and Ross 1977] through

$$\begin{pmatrix} \hat{p}(z_1) \\ \hat{p}(z_2) \\ \hat{p}(z_3) \end{pmatrix} = \begin{pmatrix} \exp(-ik^+z_1) & \exp(ik^-z_1) \\ \exp(-ik^+z_2) & \exp(ik^-z_2) \\ \exp(-ik^+z_3) & \exp(ik^-z_3) \end{pmatrix} \begin{pmatrix} B^+ \\ B^- \end{pmatrix} \qquad (2.4)$$

with the hatted quantities corresponding to the Fourier transform at the oscillation frequency.

Then, the acoustic effect of the swirler is included through a measured scattering matrix [Åbom 1991] which is defined as

$$\begin{pmatrix} B_u^- \\ B_{d1}^+ \end{pmatrix} = \begin{pmatrix} S_{11} & S_{12} \\ S_{21} & S_{22} \end{pmatrix} \begin{pmatrix} B_u^+ \\ B_{d1}^- \end{pmatrix}, \qquad (2.5)$$

where $(\ldots)_u$ and $(\ldots)_{d1}$ denote the elements upstream and downstream of the swirler respectively. The scattering matrix of the swirler is taken from Indlekofer et al. [2021a]. Finally, the pressure signal is propagated from the trailing edge of the swirler to the dump plane. This distance involves a continuous area decrease through the expansion of the bluff body, which is approximated by a series of discrete area changes through conservation laws.

The method was calibrated with a reference case under cold flow conditions where a microphone was placed at the exit, while a speaker was used for acoustic forcing. Then a frequency sweep was performed and the pressure signal was reconstructed based on the method which was discussed. The reconstruction was compared to the pressure signal measured by the microphone at the dump plane and was found to be reliable up to a frequency of ~ 3.5 kHz.

2.2   Acoustic modes in annular chambers
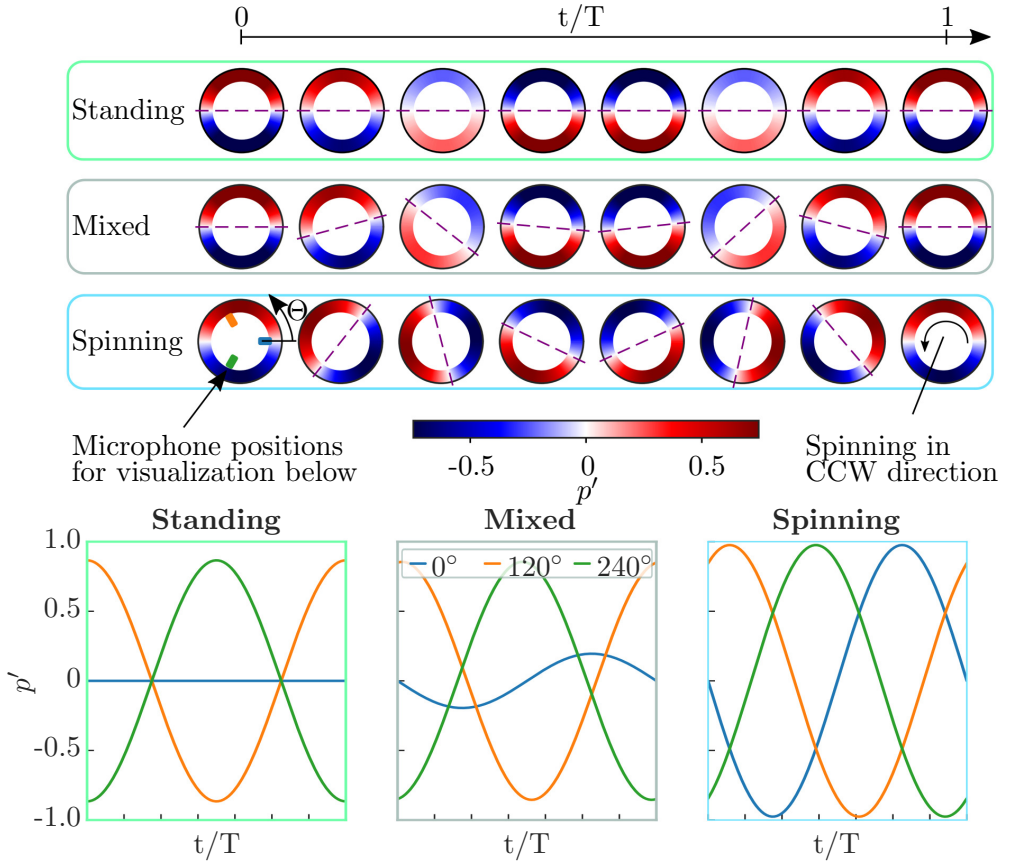
Figure 2.4: Visualization of a standing, mixed and spinning mode exemplified by the pressure field in the annulus viewed from the top of the combustor during one period of the oscillation. Corresponding pressure series for microphones at $\Theta = 0, 120, 240°$. The purple dashed line shows the nodal line.

Focusing on azimuthal modes, depending on the phase and modulus of the pressure waves, these modes can take different forms. In general, one distinguishes between three types (see Fig. 2.4 for a visualization):

- **Standing** modes with fixed locations of the pressure nodes and antinodes. In Fig. 2.4 the nodal line position (purple dashed line) corresponds to a microphone position which results in a zero amplitude response for the microphone at $\Theta = 0$.

- **Spinning** modes with nodal line spinning around the annulus at the speed of sound. One can see that the amplitude response is equal for each microphone, but the signals show a phase delay which corresponds to the azimuthal angle between the measurement locations.

- **Mixed modes**, combining both standing and spinning modes.

2.2.1   Methods used to characterize azimuthal modes

This poses the question on how one can determine the mode nature from experimental measurements, which are shown for example data in Fig. 2.4. Several mode indicators which have been used in the literature will be introduced before a recent approach, which is the main approach used in this work, is exemplified in more detail.

Similar to the expression used to calculate the acoustic field in the injector earlier, the pressure field in an annulus can be described by

$$p'(\Theta, t) = \mathrm{I\!R}\{(A^+ \exp{(-in\Theta)} + A^- \exp{(in\Theta)}) \exp{(i\omega t)}\}, \qquad (2.6)$$

where A^+ and A^- describe the complex amplitudes of two spinning waves in counter clockwise and clockwise direction, respectively, and n is the integer order of the mode. The total pressure amplitude of the mode is given by

$$A_{sp} = \sqrt{|A^+|^2 + |A^-|^2}. \qquad (2.7)$$

Equation 2.6 can describe the different azimuthal modes shown in Fig. 2.4. The relation of the two amplitudes defines whether the mode is standing ($|A^-| = |A^+|$) or spinning in CW ($|A^+| = 0$) or CCW ($|A^-| = 0$) direction.

A convenient indicator for the mode nature, based on the projection on two spinning modes, is the spin ratio [Bourgouin et al. 2013]

$$SR = \frac{|A^+| - |A^-|}{|A^+| + |A^-|}. \qquad (2.8)$$

If $SR = \pm 1$ the mode is rotating counterclockwise or clockwise respectively, while it is standing for $SR = 0$. Wolf et al. [2012] used another mode indicator

$$C(t) = \frac{1}{N} \sum_{k=1}^{N} p_k(\Theta_k, t) e^{i\Theta_k}. \qquad (2.9)$$

Thereby, the phase of $C(t)$ indicates the mode shape, e.g. a standing mode exhibits constant phase, a spinning mode increasing/decreasing phase.

Recently, Ghirardo and Bothien [2018] introduced a new ansatz to describe the nature of azimuthal modes based on quaternion algebra. The main point is that even though the previously introduced indicators are extensively used due to their simplicity, both the C-indicator as well as the the spin ratio SR are derived quantities, e.g. one can not directly relate the pressure field to them. The new ansatz provides a set of four variables which vary slowly with respect to the fast acoustic time scale. In this framework, the acoustic pressure is described by

$$
\begin{aligned}
p'\left(\Theta, t\right) = &\; A\cos\left(n(\Theta - \theta)\right)\cos\left(\chi\right)\cos\left(\omega t + \varphi\right) + \\
&\; A\sin\left(n(\Theta - \theta)\right)\sin\left(\chi\right)\sin\left(\omega t + \varphi\right).
\end{aligned}
\tag{2.10}
$$

where t is the time, Θ is the azimuthal coordinate and A, θ, χ and φ are the new state variables. A is the amplitude and the slowly varying real-valued angle θ describes the direction of the anti-nodal line and is comprised between $-\pi$ and π. It is important to note that at any instant, a state whose orientation angle is θ is the same as the state defined by $\theta + \pi$. Therefore the orientation angle will be bounded to $[0, \pi/n]$ for most of the investigations. The slowly varying real-valued angle χ indicates whether the azimuthal eigenmode is a standing wave ($\chi = 0$), a pure clockwise or counterclockwise spinning wave ($\chi = \mp\pi/4$) or a mix of both for $0 < |\chi| < \pi/4$. The real-valued angle φ stands for a slow temporal phase drift and it is bounded between $-\pi$ and π. These variables describe the pressure field p as a function of the time and azimuthal position Θ.

Ghirardo and Bothien [2018] introduced a useful representation of azimuthal modes in terms of the first three slow-flow variables of the quaternion formalism: A, χ and θ. The representation is shown in Fig. 2.5 and uses the slow-flow variables as spherical coordinates. The mode at a given instant t is described as a point on the Bloch sphere where A corresponds to the sphere radius, 2χ to the latitude and θ to the longitude. Subsequently, thermoacoustic states at the poles correspond to spinning modes, standing modes are located on the equator and mixed modes at intermediate latitudes.

One can relate the slow flow variables of the quaternion formalism to the earlier presented orthogonal description through

$$
\chi = \arctan(SR) \tag{2.11}
$$

and

$$
A/\sqrt{2} = A_{sp}. \tag{2.12}
$$
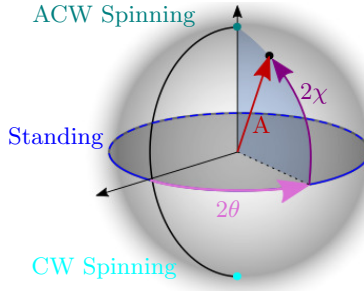
Figure 2.5: Bloch sphere representation of the state of the azimuthal mode in the quaternion representation. The amplitude A describes the radius, 2χ the lattitude and θ the longitude. Thermoacoustic states at the the poles correspond to spinning modes, standing modes are located on the equator and mixed modes at intermediate latitudes.

The exact denomination of mode shapes depends on the characterization method and the thresholds used by the authors. As shown in Fig. 1.8, the nature angle is not constant, it fluctuates and usually does not take the values corresponding to purely spinning/standing modes.

2.2.2 Determination of the azimuthal mode from experimental data

Earlier sections introduced possible descriptions of the acoustic fluctuations in an annulus. This section aims to describe how the slow flow variables of the quaternion framework, which is the main set of indicators used in this work, can be derived from experimental measurements.

As a starting point, one considers the azimuthally distributed pressure signals p_Θ which describe the pressure time series at specific azimuthal locations Θ_k. To determine the dominant mode and its frequency, we perform an FFT. For the atmospheric combustor this is without exception the mode with azimuthal mode order $n = 1$, hereafter referred to as the fundamental mode/component. However, the azimuthal combustion instabilities in the pressurized combustor feature non-negligible harmonic contributions. Therefore, the procedure that is described in the following was separately performed for the fundamental and each harmonic $n = 2 - 5$, hereafter referred to as the first to fourth harmonic. Each pressure time series is bandpass-filtered with a bandpass width of $\Delta f = 100\,\text{Hz}$ around the corresponding peak frequency f to remove noise and harmonic components. The framework takes a starting point in the description of the acoustic field by

two orthogonal eigenmodes

$$p'(\Theta, t) = \xi_1(t)\cos(n\Theta) + \xi_2(t)\sin(n\Theta). \tag{2.13}$$

The projected signals ξ_1 and ξ_2 are obtained from the filtered microphone timetraces by inverting the system

$$\begin{bmatrix} p_0 \\ p_1 \\ \vdots \\ p_k \end{bmatrix} = \begin{bmatrix} \cos(n\Theta_0) & \sin(n\Theta_0) \\ \cos(n\Theta_1) & \sin(n\Theta_1) \\ \vdots & \vdots \\ \cos(n\Theta_k) & \sin(n\Theta_k) \end{bmatrix} \begin{bmatrix} \xi_1 \\ \xi_2 \end{bmatrix}, \tag{2.14}$$

where k describes the number of the pressure signals which are acquired at specific azimuthal positions Θ_k. This system is overdetermined and is solved in a least square sense. The corresponding complex analytic signals of ξ_1 and ξ_2 are

$$\xi_{a,1}(t) = \xi_1(t) + j\mathcal{H}(\xi_1(t)) \ , \ \xi_{a,2}(t) = \xi_2(t) + j\mathcal{H}(\xi_2(t)) \tag{2.15}$$

where $\mathcal{H}$ is the Hilbert transform and j is the second quaternion imaginary unit. The quaternion analytic signal of $\xi(t)$ is defined as

$$\xi_a(t) \ = \ \xi_{a,1} + i\xi_{a,2} \ = \ \xi_1 + i\xi_2 + j\mathcal{H}(\xi_1(t)) + k\mathcal{H}(\xi_2(t)) \tag{2.16}$$

with i, j, k as the quaternion imaginary units. From this point, the slow-flow variables A, χ, θ, φ are extracted from ξ_a with the step by step description presented rigorously in the appendix of [Ghirardo and Bothien 2018].

2.2.3 Theoretical model of azimuthal combustion instabilities

The theoretical model used in this work is a simplified version of the model introduced by Faure-Beaulieu and Noiray [2020]. The main aspects of the derivation will be covered here. For a thorough derivation the interested reader is referred to their work, which features the full set of equations including the effects of swirl, time delay, azimuthal asymmetry and stochastic forcing in the appendix.

It is important to stress that the model is not intended to be used for prediction of thermoacoustic stability in real systems. The stability of a combustor can only be predicted if the whole 3D geometry is considered. This is omitted in this work as only the dynamics of the azimuthal modes

are of interest. The combustor is therefore simplified as a thin annulus (see Fig. 2.6) that is described by the mean radius R, the width $\delta R << R$ and the length H.
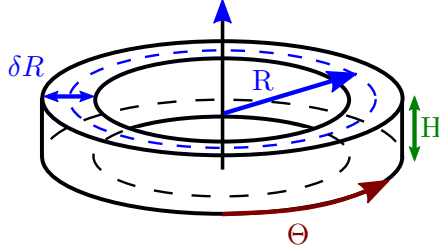
Figure 2.6: Geometry of an annular combustor simplified as a 1D annulus.

The starting point of the model is the 1D wave equation for the acoustic pressure in the chamber in presence of a thermoacoustic source term

$$\frac{\partial^2 p}{\partial t^2} + \alpha \frac{\partial p}{\partial t} - \frac{c^2}{R^2} \frac{\partial^2 p}{\partial \Theta^2} = (\gamma - 1) \frac{\partial \dot{q}}{\partial t} + \Xi(\Theta, t), \qquad (2.17)$$

which involves the following quantities: the acoustic damping at the annulus' boundaries α, the annulus' radius R, the speed of sound in the annulus c, the heat capacities ratio γ, the coherent fluctuations of heat release rate $\dot{q}$ and a spatially distributed white Gaussian noise Ξ, modeling the effect of turbulence as a stochastic forcing.

As introduced in Chapter 1, turbulent flames in gas turbine combustors are significantly affected by axial velocity oscillations. These velocity perturbations are, however, caused by pressure oscillations and can be linked through the acoustic impedance

$$Z(\omega) = \hat{p}(\omega)/\hat{u}(\omega), \qquad (2.18)$$

where $\hat{p}$ and $\hat{u}$ are the acoustic pressure and velocity in the frequency domain. Therefore the heat release response can also be expressed as a function of the acoustic pressure. The coherent heat release rate fluctuations are linked to the acoustic field using the expression

$$(\gamma - 1)\dot{q} = \beta \left[1 + c_2 \cos(2\Theta)\right]p - \kappa p^3. \qquad (2.19)$$

The first term on the right hand side stands for the linear response of the fluctuating heat release rate to acoustic perturbations. The sign of the

linear damping term defines if the flame response makes the system more unstable ($\beta > 0$) or stable ($\beta < 0$). It accounts for spatial non-uniformities along the annulus, through the second component $c_2 \cos(2\Theta)$ of the Fourier expansion of any distribution of heat release rate source, which is the only spatially varying component influencing the first azimuthal eigenmode [Noiray et al. 2011]. The second term, $-\kappa p^3$, defines the saturation of the heat release rate response, which leads to limit cycle oscillations, and is sufficient to adequately capture the thermoacoustic dynamics in the vicinity of supercritical Hopf bifurcations, which will be the region this work considers. Higher order polynomials or sigmoid functions could be applicable [Lee et al. 2021, Noiray 2016] and extend the applicability of the model beyond proximity of the bifurcation but they would complicate the system of equations considerably, and especially trouble the system identification process described in [Indlekofer et al. 2021c].

Further, the quaternion formalism from Eq. 2.10 is introduced into Eq. 2.17. There are several advantages in choosing this formalism over any of the orthogonal projections. Besides the arguments pointed out by [Faure-Beaulieu and Noiray 2020, Ghirardo and Bothien 2018] (well-posed problem, both reflectional and rotational asymmetry can be accounted for), it most importantly simplifies the parameter identification as it only leads to one amplitude equation to identify the growth rate from instead of two for the projection methods.

Performing spatial and temporal averaging [Faure-Beaulieu and Noiray 2020] leads to a nonlinear dynamical system

$$\dot{\mathbf{Y}} = \mathbf{F}(\mathbf{Y}) + \mathbf{B}(\mathbf{Y})\mathbf{N}(t), \qquad (2.20)$$

where $\mathbf{Y} = (A, \chi, \theta, \varphi)$ describes the set of slow flow variables, $\mathbf{F} = (F_A, F_\chi, F_\theta, F_\varphi)$ is the deterministic part and $\mathbf{B}(\mathbf{Y})\mathbf{N}$ is the stochastic part. The deterministic components of this system of Langevin equations are

$$
\begin{aligned}
F_A(\boldsymbol{Y}) &= \left(\nu + \frac{c_2\beta}{4}\cos\left(2\theta\right)\cos\left(2\chi\right)\right)A \\
&\quad - \frac{3\kappa}{64}\left(5 + \cos\left(4\chi\right)\right)A^3 + \frac{3\Gamma}{4\omega^2 A}, \tag{2.21} \\
F_\chi(\boldsymbol{Y}) &= \frac{3\kappa}{64}A^2\sin\left(4\chi\right) \\
&\quad - \frac{c_2\beta}{4}\cos\left(2\theta\right)\sin\left(2\chi\right) - \frac{\Gamma\tan\left(2\chi\right)}{2\omega^2 A^2}, \tag{2.22} \\
F_\theta(\boldsymbol{Y}) &= -\frac{c_2\beta}{4}\frac{\sin\left(2\theta\right)}{\cos\left(2\chi\right)}, \tag{2.23} \\
F_\varphi(\boldsymbol{Y}) &= \frac{c_2\beta}{4}\sin(2\theta)\tan(2\chi), \tag{2.24}
\end{aligned}
$$

and the stochastic components are

$$
\boldsymbol{B}(\boldsymbol{Y})\boldsymbol{N} =
\begin{pmatrix}
1 & 0 & 0 & 0 \\
0 & A^{-1} & 0 & 0 \\
0 & 0 & \frac{1}{A\cos(2\chi)} & -\frac{\tan(2\chi)}{A} \\
0 & 0 & 0 & A^{-1}
\end{pmatrix}
\begin{pmatrix}
\zeta_A \\
\zeta_\chi \\
\zeta_\theta \\
\zeta_\varphi
\end{pmatrix}. \tag{2.25}
$$

Thereby $\nu = (\beta - \alpha)/2$ which corresponds to the linear growth rate of the amplitude A in absence of asymmetries ($c_2 = 0$) and ζ_A, ζ_χ, ζ_θ, ζ_φ, are white noises of intensity $\Gamma/2\omega^2$.

Through calibration with experimental data, the derived model is able to quantitatively and qualitatively reproduce the dynamics of the slow-flow variables A, χ, θ, φ that we introduced in the previous section. After calibration, the parameter space can be investigated further. The model is only applied to the atmospheric combustor as it can not handle the harmonic contributions that are present in the pressurized combustor.

Chapter 3

Experimental setups and diagnostics

Two different experimental setups have been used in the current work. The first setup is the atmospheric annular combustor developed by Worth and Dawson [2013a,b], which was introduced at Cambridge University, Engineering Department, but an identical version with additional features on the ignition system and cooled walls, exists now at NTNU. The second setup is an intermediate pressure annular combustor (IPA) which resembles parts of the geometry of the atmospheric setup and is introduced as part of this thesis. It features a choked outlet condition and can operate up to 4 bar.

3.1 Atmospheric annular combustion chamber

The annular atmospheric combustor was introduced to resemble the main features of modern aero gas turbine combustors and enable the study of azimuthal combustion instabilities in a well-controlled and accessible environment [Worth and Dawson 2013a,b]. A schematic of the combustor is shown in Fig. 3.1.

The fuel and air are mixed in a mixing chamber which is located far upstream. Therefore, the mixture that is fed into the cylindrical plenum by two impinging jets, can be described as perfectly premixed. After an expansion, the flow is conditioned by a perforated grid. The honeycomb flow straightener, which was used in the plenum in earlier publications [Mazur et al. 2019, Nygård et al. 2019, Worth and Dawson 2013a,b], is not used in this work as the flow was found to be equally distributed over the injectors
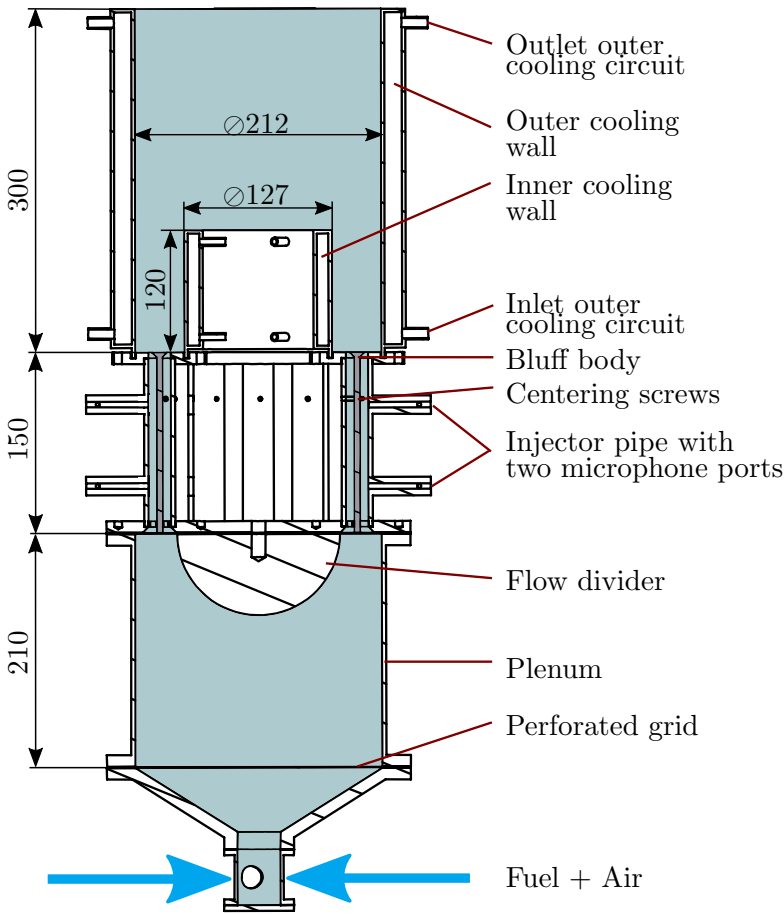
Figure 3.1: The atmospheric annular combustor with dimensions.

without it and as the presence of the honeycomb increases the complexity of acoustic simulations.

A hemispherical flow divider of diameter 140 mm distributes the flow onto 12 identical injectors with machined chamfers at their upstream end to aid smooth flow distribution. The injectors are distributed equidistantly along a circle of diameter 170 mm.

The combustion chamber is made out of cooled walls with diameters of 127 and 212 mm and lengths of 120 and 300 mm respectively. When optical access is needed, a quartz glass segment can be combined with a shortened outer wall segment (without cooling) to achieve the same dimensions (see
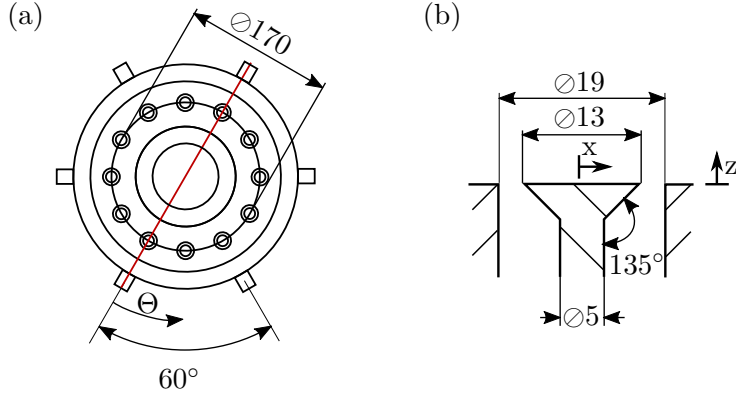
Figure 3.2: a) Top view of the atmospheric annular combustor (In- and outlets of the cooling circuits are excluded in this view) and b) Dimensions of the injector.

Fig. 3.3). The fuel/air mixture is ignited with a retractable glow plug at the exit of the outer enclosure.

Injectors

Each injector is equipped with a concentrically placed conical bluff body of diameter 13 mm which leads to a blocking ratio of 50% (see Fig. 3.2). The bluff bodies are centered by a webbed insert at the upstream side and three M4 grub screws to fine tune the centering at the downstream side. They are positioned flush to the dump plane. Axial swirlers can be mounted upstream of the bluff bodies [Worth and Dawson 2013a] but the works in this thesis constitute investigations without swirlers as for example in Mazur et al. [2019]. Every second injector contains two microphone ports which are separated by 60 mm (see Fig. 3.1).

Cooled walls

In earlier publications, the combustor did not feature cooled walls. This led to two problems: First, the maximum run time of the experiments was limited due to the strong radiation emitted by the glowing walls (see Fig. 3.3), which might damage surrounding equipment. Second, the combustor needed a long time to heat up and running experiments outside of the thermal equilibrium was not found to be satisfactory as initial investigations showed that the modal dynamics in the annular combustor are sensitive to temperature changes. To enable longer run times, shorter warm up times and equilib-
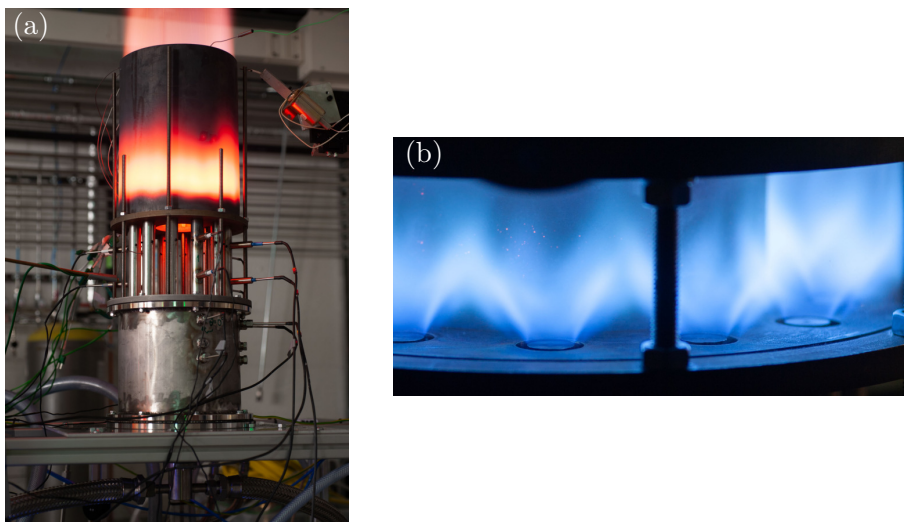
Figure 3.3: a) The atmospheric annular combustor under operation with uncooled walls and b) Annular combustor with a quartz glass segment for optical access of the combustion chamber.

rium wall temperatures, the combustor was equipped with cooled walls. The cooled walls were manufactured in the style of cooling jackets, but still have the same combustion chamber dimensions as the uncooled version. Two separate water circuits provide the water for the inner and outer walls which have three and four inlets and outlets respectively. The cooling water enters at the bottom and leaves the cooling jacket at the top. The flow rates of each cooling circuit are measured by Omega FPB1400 paddle wheel meters and thermocouples measure the temperature of the incoming and outgoing flows.

Gas supply system

Air and fuel flow rates are controlled with Alicat MCR Mass Flow Controllers (MFC). Two MFCs (full scale $80 \, \mathrm{g \, s^{-1}}$ combined) are used for air, and up two four MFCs (full scale $2.5\text{-}20 \, \mathrm{g \, s^{-1}}$ each) are used for fuel. Each MFC is accurate to $\pm 0.8\%$ of the reading plus $\pm 0.2\%$ of the full scale. In general, the combustor can be run with any gaseous fuel available, but in the investigations in this work the fuel is limited to methane/hydrogen mixtures.

3.2 Intermediate pressure annular (IPA) combustion chamber

The intermediate pressure annular (IPA) combustion chamber constitutes a novel lab-scale annular combustor at elevated pressure. There are several motivations behind the development of this setup. Previous experimental studies have been performed at atmospheric pressures with a boundary condition which is often not well defined. In particular the length mismatch of the outer and inner wall, as described in the previous section, complicates efforts to replicate these boundary conditions numerically. Also, industrial and aero-engine gas turbine combustors operate at elevated pressures and feature an outlet boundary condition to the turbine that is choked. Therefore the IPA combustor was developed to operate at pressures up to 3.5 bar. A common way to generate a well defined boundary condition is to choke the flow at the exit by reducing the flow area which leads to the pressurization of the combustor.

Figure 3.4 depicts a cut of the combustor geometry. After being mixed in a mixing chamber upstream, the premixed fuel-air mixture enters the combustor at the bottom and passes the glass bead filled plenum expansion. Optionally, an additional choking plate can be mounted just upstream of the glass bead section.

After the hemispherical flow divider, the flow is further homogenized by a highly acoustically reflective sintered metal plate (mean pore size $183\,\mu m$, porosity 0.12 and $\Delta p \approx 0.15\,bar$) and divided onto 12 injectors.

The diameters of the inner and outer enclosure resemble the atmospheric combustor with diameters of $128\,mm$ and $212\,mm$ respectively. The combustor features a $50\,mm$ long Quartz glass segment for optical access of the flames.

The combustor was designed so that the length of the combustor can be modified through the use of additional wall elements, but the investigations in this thesis are limited to a combustor length of $168\,mm$.

Injectors

Each injector is equipped with a concentrical bluff body and a swirler. The mounting method differs from the atmospheric version. A webbed insert is screwed onto the bluff body holder at the upstream end and compressed into a machined rabbit that fixes the location of the bluff body during assembly. The swirler, which is mounted further downstream, supports the centering.
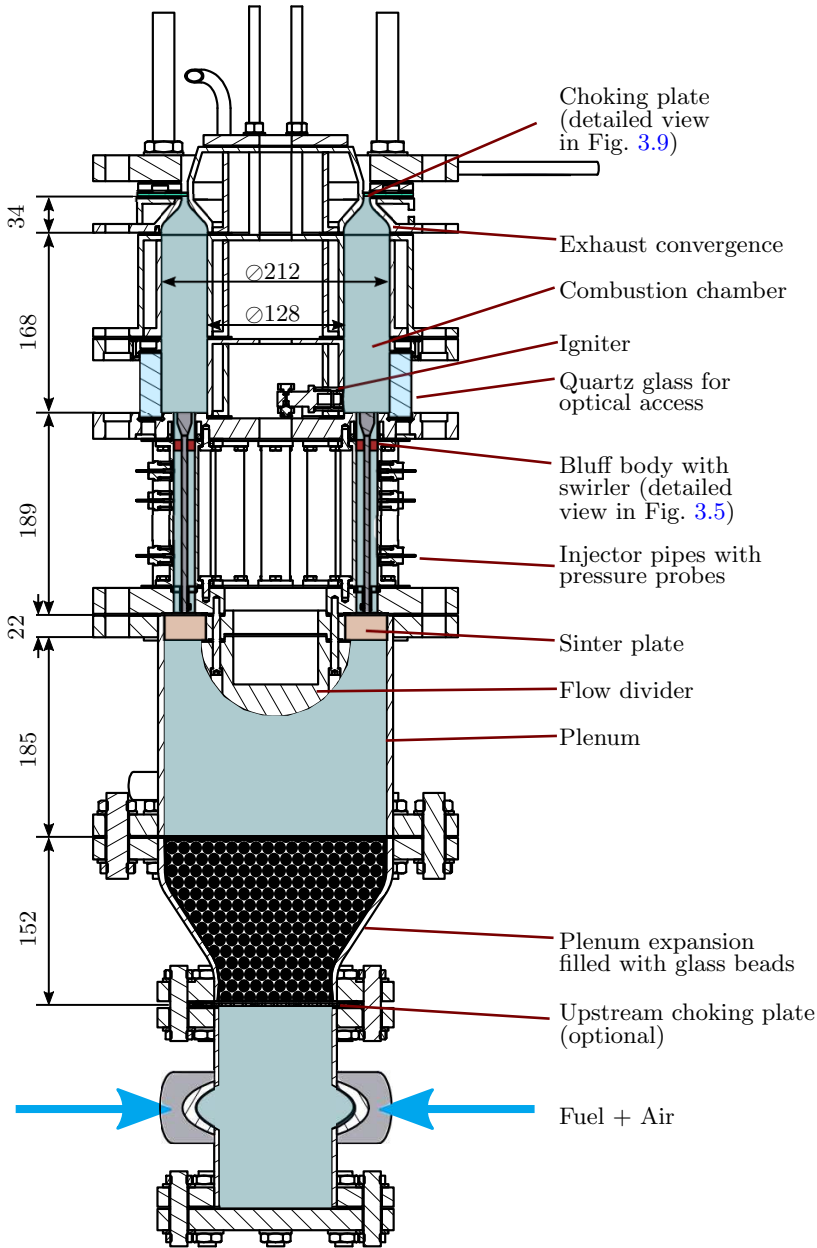
Figure 3.4: Schematic of the intermediate pressure annular (IPA) combustor.
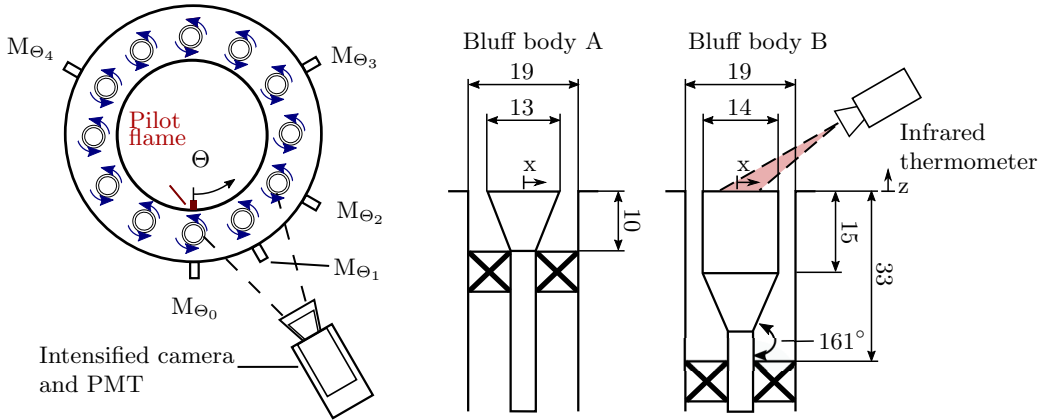
Figure 3.5: Top view and schematic of the injectors of the IPA combustor.

The bluff body design was modified twice during the design of the combustor. Two versions of bluff bodies are used (see Fig. 3.5 and 3.6). Bluff body A resembles the bluff bodies used in the atmospheric setup except for a significantly lower cone half angle of 19°. However, this bluff body assembly was found to cause a large recirculating region behind the swirler that promotes flashback. Bluff body B was introduced to reduce flashback that was observed under unstable operation [Mazur et al. 2020] and features an increased diameter and a 15 mm long cylindrical section in an effort to create a region of high velocity which prevents the flame from anchoring further upstream. Subsequently the swirlers had to be moved further upstream for assembly B.

The swirler is a six vane swirler with a trailing edge angle of 60° and is mounted onto the bluff body rod by an expanding rivet. The swirler results in a counterclockwise swirl motion of the flow when observed from downstream. It has a geometrical swirl number of 1.22 before the contraction of the bluff body. To preserve the rotational geometry of the combustion chamber, each swirler is oriented with two swirler vanes pointing towards the center of the combustion chamber.

Cooling system

The combustor is water cooled through three separate cooling circuits: the back plate, inner walls and outer walls (see Fig. 3.8). The flow rates of the different cooling circuit are measured by Omega FPB1400 paddle wheel meters. For the inner and outer wall circuits, the water enters at the bottom

Figure 3.6: Left side: Injector pipe with microphones mounted. Right side: Evolution of the bluff bodies of the IPA combustor with the bluff bodies A and B which were used in this work.

on one side and exits the corresponding part at the other side towards the top, entering the next component. Water temperatures are measured at the in- and outlet of each circuit for calculation of the cooling rates. A combined cooling rate of up to $150\,\mathrm{kW}$ can be achieved.

Exit contraction

At the exit a symmetrical contraction reduces the area with a contraction ratio $CR = 7$. A second area reduction is achieved by a replaceable choking plate. Two different choking plate designs were utilized. Initially, a hole plate with 164 holes of $2\,\mathrm{mm}$ diameter, distributed around the mean chamber diameter $169.5\,\mathrm{mm}$ was used, leading to a total blockage ratio $CR_{total} = 44$ (Choking plate A). This design suffered from the extreme thermal stress and had to be replaced periodically. The optimized design (Choking plate B) does not feature the holes but a second area contraction that limits the flow to an area between the inner contraction diameter $D_{c,in} = 163.5\,\mathrm{mm}$ and the outer contraction diameter of the choking plate which could be varied between $D_{c,out} = 166.2 - 165.6\,\mathrm{mm}$ depending on the utilized plate.
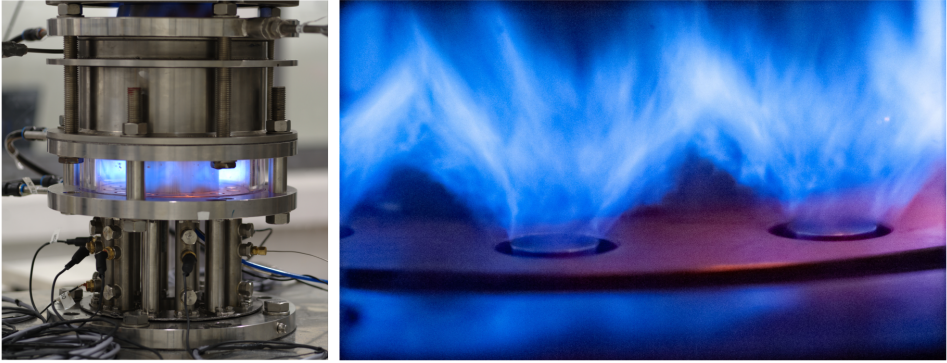
Figure 3.7: Photographs of the IPA combustor.
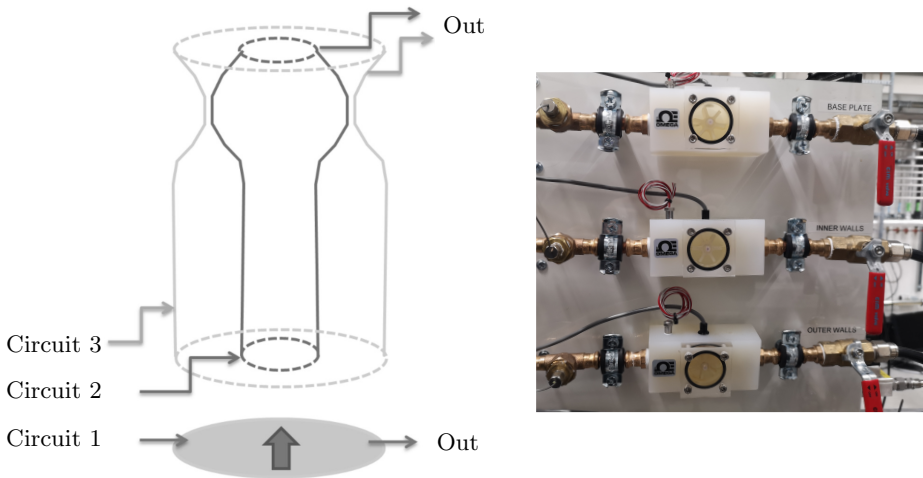
Figure 3.8: Left side: Schematic of the cooling circuits of the IPA combustor. Right side: Paddle wheel meters with temperature measurements for each cooling circuits.

Choking plate B is centered against the inner walls by three small notches with a width of $5\,\mathrm{mm}$. This leads to $CR_{total} = 32.8 - 42.5$ depending on the chosen plate. A schematic of both chocking plates is shown in Fig. 3.9.

Ignition

The ignition of the system is initiated with a premixed ethylene-air pilot flame, shown in Fig. 3.10, which impinges radially into the combustion chamber at $\Theta = 0$. The combustor is ignited close to atmospheric conditions ($\bar{p} = 1 - 1.5\,\mathrm{bar}$, depending on choking plate), usually at $\dot{m}_{air} = 30\,\mathrm{g\,s^{-1}}$.

Choking plate A   Choking plate B

Gasket
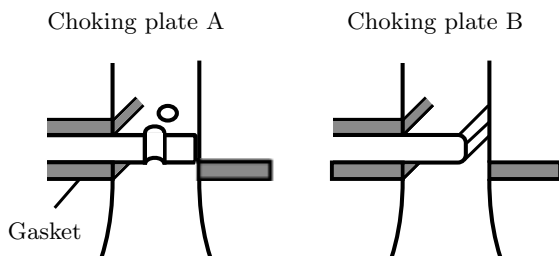
Figure 3.9: Choking plate assemblies of the IPA combustor.

The pilot flame is ignited ($\dot{m}_{air,P} = 0.2\,\text{g}\,\text{s}^{-1}$, $\dot{m}_{C2H4,P} = 0.02\,\text{g}\,\text{s}^{-1}$) before the fuel MFCs are opened. After the light-around is completed, the fuel flow through the ignitor is stopped, while its air flow is maintained for protection of the ignitor system. Then the final operating condition is reached via equivalence ratio and volume flow rate ramps. A spark-ignition unit, enabling more relevant ignition conditions or relight studies, is currently under commissioning.
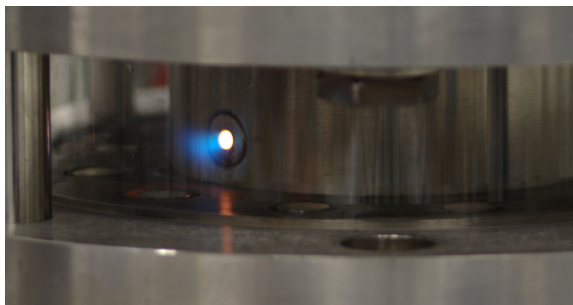
Figure 3.10: Ethylene/air pilot flame of the IPA combustor.

Gas supply system

A schematic of the infrastructure, including gas and air lines, is shown in Fig. 3.11.

Air and fuel flow rates are controlled with Alicat MCR Mass Flow Controllers (MFC) (see Tab. 3.1). For the main air supply, three MFCs (full scale $300\,\text{g}\,\text{s}^{-1}$ combined) are used, and up to three MFCs (full scale $20\,\text{g}\,\text{s}^{-1}$ each) are used for the main fuel supply. Additionally two MFCs (full scale $1\,\text{g}\,\text{s}^{-1}$ each) control the pilot air and fuel flow rates. Each MFC is accurate to $\pm0.8\%$ of the reading plus $\pm0.2\%$ of the full scale.

Table 3.1: Overview of the MFCs for the IPA combustor.

	Number of MFCs	Flow range per MFC $[\mathrm{g\,s^{-1}}]$
Main air	3	100
Main fuel	3	20
Pilot air	1	1
Pilot fuel	1	1

Nitrogen lines provide purging capabilities for the fuel lines and the combustion chamber in case of an emergency. An additional safety feature is implemented through a burst disk which opens for a pressure $> 10\,\mathrm{bar}$ and releases the gases through the exhaust.

Similar to the atmospheric setup, the combustor is usually run with ethylene, methane and/or hydrogen. The combustor can be operated at thermal powers up to $400\,\mathrm{kW}$.
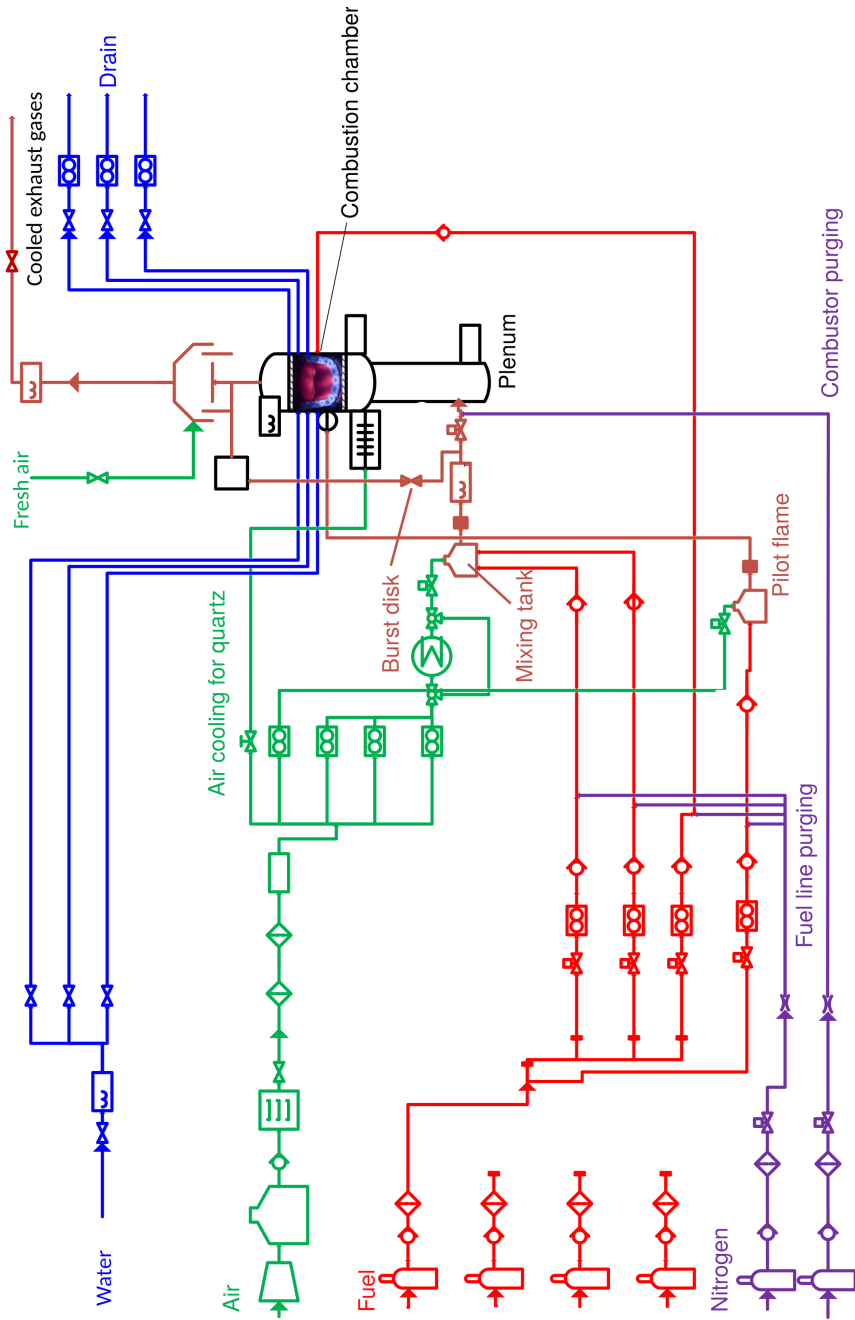
Figure 3.11: Infrastructure of the IPA combustor.

3.3   Impedance measurement setup

For the acoustic characterization of components, an impedance measurement setup was designed to measure the scattering matrices following Åbom [1991]. The measurement setup is shown in Fig. 3.12. Two identical pipes with an inner diameter of 19 mm and four microphone ports on each side are used. In the figure, both horn drivers are mounted, however a total of five independent states is measured for each measured component: left open - speaker right, left closed - speaker right, speaker left - speaker right, speaker left - right closed and speaker left - right open. The measured component (swirler, sintered metal plate, glass bead section) is located in between the two pipes.

Figure 3.12: Schematic of the impedance pipe for acoustic characterization of components.

An Aim-TTi TGA1244 signal generator was used to control the horn drivers. The investigated frequency range was $100 - 3000\,\text{Hz}$. The method was validated by the investigation of an open pipe which resulted in the expected behavior without reflection (see Fig. 3.13). The scattering matrices of different elements are presented in Indlekofer et al. [2021a].
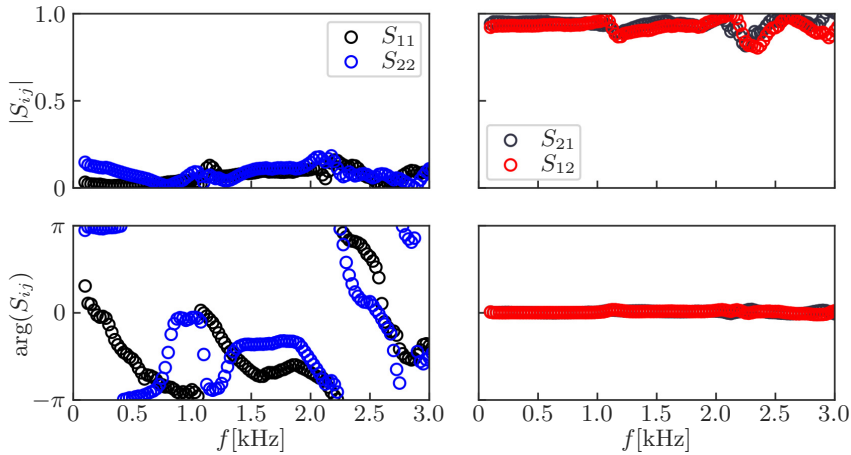
Figure 3.13: Scattering matrix for the open pipe test case.

3.4   Diagnostics

3.4.1   Acoustic pressure measurements

In terms of the acoustic measurements one can differ between the implementation for the atmospheric and the pressurized combustor:

- Atmospheric annular combustor: Kulite XCS-093-05D miniature transducers with a sensitivity of $4.2857 \times 10^{-3}\,\mathrm{mV\,Pa^{-1}}$ were used. The microphones are glued into plastic tubes, oriented flush with the outer wall of the injector and hold in place by O-rings. The signals were amplified by Fylde FE-579-TA bridge amplifiers. The data was acquired with NI-9234 24-bit DAQ cards with a sampling frequency of $f_s = 51.2\,\mathrm{kHz}$. Microphones were mounted flush to the inner wall of the injector pipes for every other injector (at $z = -35$ and $-95\,\mathrm{mm}$, see Fig. 3.1 and 3.2). In the plenum, microphone ports were available at $z = -180$ and $-245\,\mathrm{mm}$ and three azimuthal positions $\Theta = 0, 45, 90°$.

- IPA combustor: Three Danfoss MBS 3000 pressure sensors monitored the mean pressures upstream of the plenum expansion, in the plenum and in one injector pipe. High speed pressure measurements were performed with Kulite XCE-093-7barA sensors with a sensitivity of $1.43 \times 10^{-4}\,\mathrm{mV\,Pa^{-1}}$. The microphones are glued into small metal pipes which are then inserted into microphone ports in the injector pipes and held in place by compression glands. Each microphone as-

sembly was pressure tested up to 5 bar for leakage. The signals were amplified by the same amplifiers as used in the atmospheric setup and then acquired with NI-9215 16-bit/NI-9234 24-bit DAQ cards with a sampling frequency of $f_s = 51.2\,\text{kHz}$. Due to the increased harmonic contributions that were observed in the experiments, five injector pipes contained three longitudinally spaced microphone ports at $z = -44, -81$, and $-133\,\text{mm}$ (see Fig. 3.5 and 3.6). To resolve the higher azimuthal mode orders, the measurements were performed at $\Theta = 0, 30, 60, 120, 240°$. Additional ports for high speed measurements are available in the plenum and upstream of the plenum expansion.

3.4.2   Flame chemiluminescence

The unsteady heat release rate is a key measure in the experimental study of combustion instabilities. Flame chemiluminescence is based on the spontaneous light emission of chemical radicals due to reactions in the flame front, and is used extensively to study properties of reacting flows like the equivalence ratio or the heat release rate [Haber et al. 2000]. Each radical emits light at a specific wavelength. For lean premixed flames, which are the subject of this thesis, the relation between OH* radicals and the heat release rate is well established and was shown to provide a good estimate under both atmospheric and elevated pressures [Docquier et al. 2000, Hurle et al. 1968]. The characteristic wavelength of OH* radicals is $\approx 306\,\text{nm}$.

Photo multiplier

Photo multiplier tubes (PMT) were also used to measure OH* radicals. The signal of the light emission is converted to a voltage which is acquired alongside the pressure signals via the corresponding 16 or 24 bit DAQ card at $f_s = 51.2\,\text{kHz}$. The high temporal resolution (equal to the pressure measurments) is a major advantage of the PMT measurements, and acquiring the signal on the same DAQ ensures a perfect synchronization. In the studies described in this thesis, a Hamamatsu H11902-113 PMT was used in combination with a Hamamatsu C7169 amplifier. To isolate the light emission of the OH* radicals, a LC-HBP310/10-50 bandpass filter with a central wavelength of 310 nm and a band width of 10 nm was used. The photomultiplier integrates the light emission over its full view and is therefore not spatially resolved, but it provides a measure of the global heat release rate. It also has to be limited in terms of its field of view to limit the signal to correspond to the light emission of one specific flame. As the flames interact strongly in the pressurized combustor, this window has to be chosen very accurately. Therefore, two plates blocking neighboring flames were moun-

ted. The position of each plate was evaluated manually with the help of a blow torch and an oscilloscope. The signal of the PMT was compared to the high speed imaging and found to give a satisfactory representation of the heat release rate for one flame.

High-speed imaging

To investigate flame shape and study the flame dynamics in detail through phase-averaged images, high speed imaging is used. High speed imaging is able to measure the heat release rate spatially resolved in two dimension but still constitutes a line of sight measurement in the third dimension (the depth). Phantom V2012 CMOS cameras are used with a sampling frequency of $f_{s,cam} = 10\,\text{kHz}$ for investigation of the atmospheric combustor or $16\,\text{kHz}$ for the pressurized combustor.
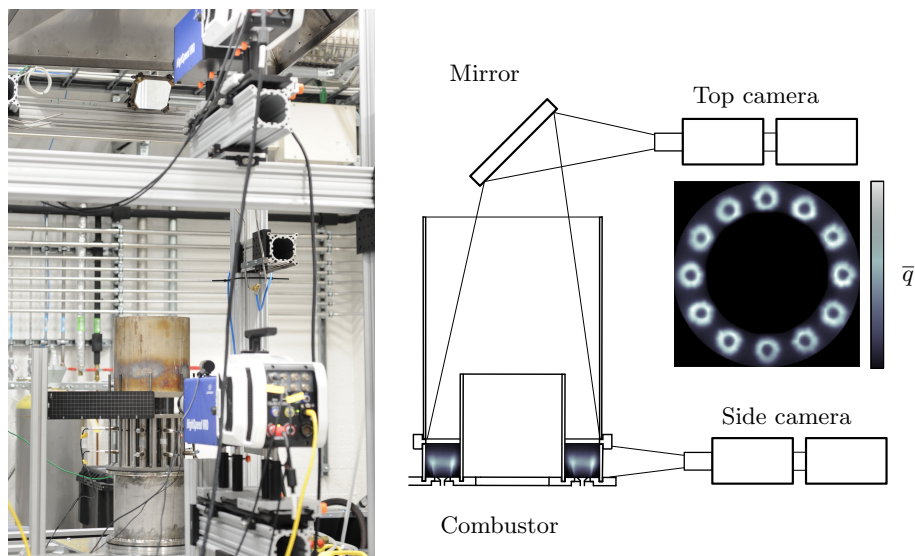
Figure 3.14: Photograph and schematic of the camera arrangement of the atmospheric combustor for simultaneous side and overhead imaging. The dimensions of the schematic are not to scale to keep the figure compact.

The increased $f_{s,cam}$ was required to resolve higher harmonic contributions. The cameras are combined with a LaVision lens-coupled intensifier to amplify the weak light signal and an identical filter to that used for the PMT. The trigger signal of the camera was acquired and widened by an Aim-TTi TGA1244 signal generator before the modified signal was acquired with the

Figure 3.15: Camera arrangement of the IPA combustor.

DAQ system and post-processed to retrieve the exact image timing. For the atmospheric combustor, high speed imaging was performed from both the side and the top via an air-cooled mirror as shown in Fig. 3.14. For the IPA combustor, high speed imaging was performed from the side only (see Fig. 3.15).

3.4.3   Wall temperature and heat transfer measurements

Heat transfer to the walls and flame holders is known to play a significant role in the study of combustion instabilities [Hong et al. 2013, Mejia et al. 2018, Miguel-Brebion et al. 2016], especially when operating close to the stability border. The thermal state of the combustor plays an important role and can have a large impact on the flame [Bonciolini et al. 2019a]. Therefore it must be ensured that the combustor is close to its thermal equilibrium before data is acquired to preclude temperature effects on the modal dynamics. Additionally, to adequately model the combustor, simulations are dependent on accurate temperature measurements.

Three types of measurements were performed to gain information on the heat transfer and wall temperatures in this work. In the atmospheric combustor, arrays of thermocouples (RS PRO Type K 1.5 mm) were used to measure the mean axial and circumferential temperature profiles to ensure that the introduction of the cooled walls does not break the symmetry. Measurements for two runs are shown in Fig. 3.16 and correspond to data
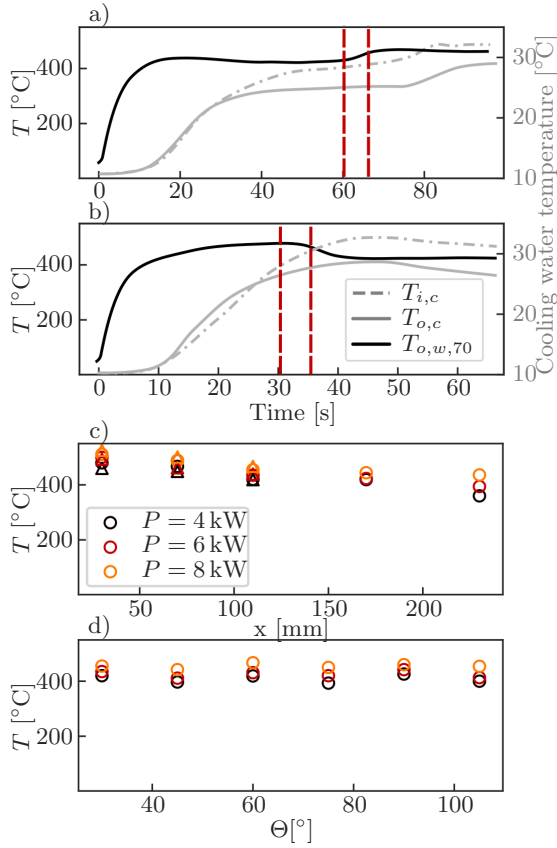
Figure 3.16: Temperature measurements of the outer and inner walls and water cooling temperatures during equivalence ratio ramps in the atmospheric annular burner [Indlekofer et al. 2021b]. The red dashed line shows the start and end of the equivalence ratio ramp respectively. The outer wall temperature $T_{o,w,70}$ was measured at $x_{T3} = 70\,\mathrm{mm}$ and $\Theta = 30°$ and $T_{i,c}$ and $T_{o,c}$ are the cooling water temperature of the inner wall and the outer wall respectively. Subfigure a) corresponds to an increasing and b) to a decreasing equivalence ratio ramp with $P = 8\,\mathrm{kW}$ and $t_{ramp} = 5\,\mathrm{s}$. c) Longitudinal (at $\Theta = 30°$) and d) circumferential (at $x = 70\,\mathrm{mm}$) wall temperature distribution at $t = 60\,\mathrm{s}$. Circular markers describe the outer wall, triangular markers the inner wall.

presented in [Indlekofer et al. 2021b]. Five thermocouples at the outer wall and three thermocouples at the inner wall are distributed in axial direction at $\Theta = 30°$. At $70\,\mathrm{mm}$ above the dump plane, six thermocouples are distributed in azimuthal direction on the outer wall with $\Delta\Theta = 15°$ between each measurement point. Subfigures a) and b) show the heat up process

of the wall temperature and c) and d) show the axial and circumferential distribution. In the axial direction the temperature reduces slightly towards the exit. The mean temperature variation in the circumferential direction is $\approx 10-20\,°\text{C}$ which suggests that the heat transfer does not have a significant impact on symmetry breaking.

The pressurized combustor does not allow the introduction of thermocouples into the combustion chamber. Thermometry provides a contactless alternative which is based on the electromagnetic radiation which a surface emits [Mobley 2001]. Specifically, infrared thermometry can be used to measure the temperature of a surface almost instantaneously.

The key factor for an accurate measure is the emissivity of the surface which has to be adjusted to the application. In our case this adjustment was done by heating up a reference part made out of the same material as the component being investigated. The surface was equipped with a thermocouple and heated with a blow torch up to a temperature of $400\,°\text{C}$. Then the transients of the cooldown measured by the thermocouple and the infrared thermometer were compared and the emissivity was iteratively adjusted until the transients collapsed. For the bluff body an emissivity of $\epsilon_{bluff} \approx 0.7$ was determined and for the dump plane and the combustor walls $\epsilon_{wall} \approx 0.65$.

An Optris CT Laser 3MH infrared thermometer with a spectral range of $2.3\,\mu\text{m}$, a temperature range of $100\text{-}600\,°\text{C}$ and a response time of $2\,\text{ms}$ was used. The chosen optics lead to a measuring spot size of $4.5\text{-}8\,\text{mm}$ depending on the distance and the angle of the sensor with respect to the surface. As the flame also emits radiation in the respective spectral range, this method did not allow for instantaneous measurements over the complete run time of the combustor but provided a temperature at the end of a test run, when the flame was switched off. That means the combustor had to be ignited and switched off several times to measure the transient heating. Subsequently, detailed temperature measurements of the bluff body, the inner wall and the dump plane were only performed for chosen operating conditions. Figure 3.17 shows the transients of the temperature at three locations in the IPA combustor.

In addition to the temperature measurements, the flow rates and the inlet and outlet temperatures of the cooling water were measured for both combustors to provide a measure of the heat transfer through the outer and inner walls.
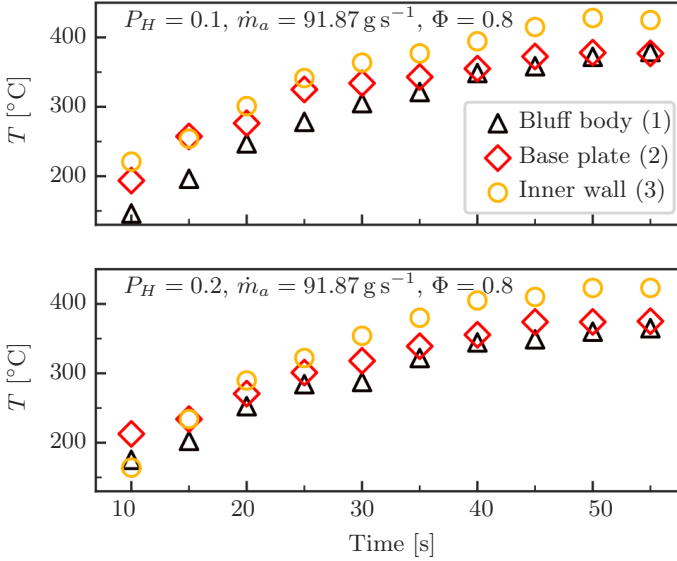
Figure 3.17: Temperature measurements with the infrared thermometer in the pressurized annular combustor [Indlekofer et al. 2021a]. Temperatures T_1-T_3 corresponding to temperatures measured at the bluff body, base plate and inner wall respectively. Top and bottom figure correspond to hydrogen contents $P_H = 0.1$ and 0.2 respectively.

3.4.4 Velocity measurements

Velocity measurements were performed to detect and eventually eliminate flow asymmetries in the combustors, mainly downstream of the injectors to ensure that the flow rates through the injectors were equal. To do this, hot wires were used, specifically constant temperature anemometry, which is based on measuring the heat transfer over a heated wire which is cooled in the measured flow.

Therefore, a tiny tungsten wire mounted on two prongs (Dantec 55P11, miniature wire sensor, 5 nm in diameter, 1.25 mm probe width) is placed into the flow and kept at a constant temperature as it is connected to one arm of a Wheatstone bridge (Dantec StreamLine Pro system). To hold the wire at a constant temperature, a voltage E has to be supplied, which gives a measure of the heat transfer transfer. The convective heat transfer is related to the velocity u and the well known Kings law [King 1914]

$$E^2 = \Delta T A_w h = a + b u^m, \tag{3.1}$$

where ΔT is the difference between the wire and the surrounding air temperature, A_w is the wire's surface and h the heat transfer coefficient, is used. This translates to three constants a, b and m which are determined through calibration. The calibration was performed before and after the measurements on a top hat profile produced by a nozzle.

The main advantages of this technique are the fast response, allowing for a high frequency resolution, a high dynamic range and negligible flow disturbance due to the small size of the probe. The drawbacks are that the flow velocity is averaged over the length of the wire, which means the measurement is not an exact point measurement. Also, single wires measure the velocity magnitude and not the single components and can therefore not distinguish between flow directions or handle flow reversal.

Chapter 4

Conclusions and summaries of the research articles

This thesis describes an experimental study of thermoacoustic instabilities in annular combustion chambers. Chapter 1 motivates the investigation of combustion instabilities, reviews recent studies on the topic and identifies the need for further experimental data in annular combustors, specifically under pressurized conditions. In Chapter 2, common descriptions and indicators of azimuthal modes based on two different frameworks and the identification of those indicators from experimental data are introduced. A theoretical model of azimuthal combustion instabilities is also presented. The experimental setups and measurement devices used in this work are described in detail in Chapter 3. One model annular gas turbine combustor with bluff body stabilized flames is used for investigations at atmospheric conditions. A second experimental setup is designed and commissioned for investigations at pressurized conditions and features a similar geometry as the atmospheric combustor but with a choked nozzle outlet that allows investigations with a well-defined boundary condition.

In the next part of the thesis, the novel contributions of this work are presented in the form of seven scientific articles. Common for the articles is that they all concern experimental studies of thermoacoustic instabilities in annular combustors. While the first two articles utilize the atmospheric combustor and combine experimental investigations with low-order modelling, the next three articles cover the novel pressurized annular combustor. The remaining two articles investigate the effect of dynamic operating conditions in the atmospheric and pressurized annular combustor respectively.

A short summary of each of the articles with their main contributions and how they connect to the objectives of the thesis is given below:

Article I

Spontaneous and explicit symmetry breaking of thermoacoustic eigenmodes in annular geometries

Thomas Indlekofer, Abel Faure-Beaulieu, Nicolas Noiray, James Dawson
Under consideration for publication in Physical Review Letters.

This work addresses the first objective from the introduction and studies modal dynamics in the annular atmospheric combustor. Experiments are conducted at constant operating conditions over a range of equivalence ratios at a power of $6\,\mathrm{kW}$ per burner and a fuel composition of 70% hydrogen and 30% methane by power. A supercritical Hopf-bifurcation is observed around an equivalence ratio of 0.51. Initially the combustor features a standing mode but with increasing equivalence ratio (and amplitude) the phase space becomes bimodal and the mode switches spinning direction intermittently. When the amplitude becomes large compared to the noise (at maximum equivalence ratio), the mode cannot switch direction anymore but keeps spinning in one direction. A system identification approach is used to calibrate a recently developed low-order model [Faure-Beaulieu and Noiray 2020] which is able to capture the effects of spontaneous and explicit symmetry breaking on the thermoacoustic eigenmodes in the combustor. To investigate the complete phase space topology of the system, arbitrary changes in the growth rate and the asymmetries are induced and the stationary solution of the Fokker-Planck equation is calculated. The joint PDFs show transitions between unimodal, bimodal, single torus and double tori states and allow the identification of a magnified lens effect of a minute asymmetry that prohibits the occurrence of single tori phase spaces in real engines.

Article II

Experiments and low-order modelling of intermittent transitions between clockwise and anticlockwise spinning thermoacoustic modes in annular combustors

Abel Faure-Beaulieu, Thomas Indlekofer, James Dawson, Nicolas Noiray

Proceedings of the Combustion Institute, in press.

Article II utilizes the same experimental data set as *Article I*, and specifically investigates the intermittent switching between clockwise and anti-clockwise spinning modes. The same model is simplified and reduces to a potential landscape. At operating conditions featuring standing modes, the landscape consists of a single well corresponding to a standing mode. It describes a symmetric double well potential for the intermittently switching modes, where each well corresponds to either spinning direction. With increasing amplitude of the instability, the potential barrier increases until the mode is not able to switch direction any more (to be pushed from one well to the other by the noise). The calibrated model is able to recreate the mean switching time of the experiments.

Article III

Self-excited longitudinal and azimuthal modes in a pressurized annular combustor
Marek Mazur, Yi Hao Kwah, Thomas Indlekofer, James Dawson, Nicholas A. Worth
Proceedings of the Combustion institute, in press.

Article III introduces the first pressurized lab-scale annular combustor able to self-excite thermoacoustic instabilities, and therefore targets the second objective. Experiments are performed between 2 and 3 bar chamber pressure for ethylene-air mixtures and the combustor is equipped with 12 swirled bluff body stabilized injectors (Bluff body A). The pressurization of the chamber is achieved by reducing the exit flow area through a choked nozzle (Choking plate A). Initially the combustor features longitudinal instabilities but at high equivalence ratios the flame stabilization position moves upstream into the injectors, promoting a transition to azimuthal modes. The pressure spectra features strong harmonical components besides the fundamental frequency, demonstrating the response of high amplitude self-excited azimuthal instabilities under pressurized conditions may contain additional complexity in comparison with modes generated at atmospheric conditions. A wide range of modal dynamics is observed. Interestingly, the fundamental and harmonic components do not necessarily feature the same mode nature, i.e. the harmonic component can spin in the opposite direction of the fundamental mode.

Article IV

The effect of hydrogen addition on the amplitude and harmonic response of azimuthal instabilities in a pressurized annular combustor
Thomas Indlekofer, Byeonguk Ahn, Samuel Wiseman, Yi Hao Kwah, Marek Mazur, James Dawson, Nicholas A. Worth
Combustion and Flame, Volume 228, June 2021, Pages 385-387.

A modified version of the pressurized combustor is introduced in *Article IV*. The combustor features a modified bluff body geometry with a larger diameter and the addition of a cylindrical section circumventing the flashback issue (Bluff body B) and a modified choking plate (Choking plate B). Experiments were performed for methane hydrogen mixtures at pressures from 1.5 to 3.3 bar. The combustor is stable for low hydrogen contents ($P_H = 0 - 0.05$) but becomes unstable when the hydrogen content is increased. The strongest oscillations are observed for $P_H = 0.1$ while the amplitudes decrease if P_H is increased further and the combustor becomes stable again for $P_H = 0.25$. Strong harmonic components are observed for high amplitude instabilities and their relation is investigated infering a *cut-on* amplitude of the fundamental component at which the harmonic components become significant. A quadratic relationship between the different harmonic components of the mode is shown. All high amplitude instabilities feature CW spinning waves, while instabilities close to the stability border, at very low amplitudes, feature CCW spinning modes. In agreement with recent theoretical investigations, larger amplitudes lead to purer spinning modes. Similar to the work before, the nature of the harmonics can deviate from the harmonics but they always have the same spinning directions with smaller differences than observed before. High and a low amplitude cases are investigated in terms of their flame dynamics, and while the high amplitude instabilities feature an extreme distortion of the flame shape, the low amplitude case shows similar flame dynamics to results in atmospheric combustors. Emphasis in this work is also put on a thorough characterization of the boundary conditions to position this work as a reference case for numerical and theoretical investigations.

Article V

The role of fundamental and harmonic heat release rate components in self-excited azimuthal instabilities in a pressurized annular combustor with methane/hydrogen flames
Byeonguk Ahn, Thomas Indlekofer, James Dawson, Nicholas A. Worth
To be submitted to Combustion and Flame.

Article V is based on a subset of the data from *Article IV* and focuses on the flame dynamics of azimuthal combustion instabilities at pressurized conditions. Thereby, this work focuses on quantifying the importance of the harmonics on the heat release rate oscillations of the flames. Compared to the heavily distorted phase space of the pressure time series, the heat release rate time series is well described by the fundamental component. The reason for this is found in the spatial distribution of the heat release oscillations which shows that for high frequency oscillations multiple structures exist on a flame, eventually canceling out in the integrated heat release rate. The Rayleigh index is only very weakly affected by the inclusion of harmonics, thereby emphasizing the dominance of the fundamental component. Flame dynamics are investigated for four selected cases. The high amplitude cases are driven by the oscillation of the heat release rate at the top of the flame. The low amplitude cases show more damping at the flame brush, where heat release and pressure occur out of phase, resulting in a lower amplitude response.

Article VI

The effect of dynamic operating conditions on the thermoacoustic response of hydrogen rich flames in an annular combustor
Thomas Indlekofer, Abel Faure-Beaulieu, Nicolas Noiray, James Dawson
Combustion and Flame, Volume 223, January 2021, Pages 284-294.

Article VI connects to the third objective from the indroduction. In this article the effect of dynamic operating conditions on the response of hydrogen rich flames is investigated for the nominally symmetric annular combustor under atmospheric conditions. The combustor is equipped with twelve conical bluff bodies without swirl. To mimic the flexible load of real gas turbines, the model combustor is subjected to linear ramps of the equivalence ratio at a fuel composition of 70% hydrogen and 30% methane per power. The combustor is operated at powers of 4-8 kW per burner and the ramping

time is 5, 20 or 60 s. The operating conditions range from near blow-off to near flashback. During operation the combustor features a wide range of instabilities and exhibits repeatable modal dynamics along the equivalence ratio ramps. Two types of hysteresis were observed: 1) positive hysteresis, similar to hysteresis phenomena observed in single sector combustors and leading to a decrease of the stability range and 2) negative hysteresis which has not been observed in the field before and leads to an increase of the stability range of the combustor. The occurrence of either hysteresis phenomenon was found to be strongly dependent on the operating and ramping conditions. Additionally, a mode hopping phenomenon describing the transition from a 1A2L to a 1A3L mode is presented.

Article VII

Transient thermoacoustic responses of methane/hydrogen flames in a pressurized annular combustor
Byeonguk Ahn, Thomas Indlekofer, James Dawson, Nicholas A. Worth
Accepted for publication at ASME 2021

Article VII targets both the second and the third objective of the introduction as it investigates dynamic operation in the pressurized annular combustor. Similar to *Article VI*, the equivalence ratio is ramped linearly both upward and downward. Hysteresis phenomena are observed in both the amplitude and the nature angle. Emphasis is put on the reaction of the harmonics on transient operating conditions. While the transients are shown to largely follow the fundamental component through the quadratic relationship described in *Article IV* a non-linear response of the amplitude of the first harmonic component was observed which does not follow that relationship as the amplitude of the first harmonic drops while the amplitude of the fundamental mode reaches its maximum.

4.1   Future outlook

The conducted work in thesis could be extended in several directions in the future.

The combined experimental/theoretical approach of Articles I and II makes use of a simplified model to recreate the dynamics observed in the experiments. This approach could be extended in several ways:

- In practice, coherent heat release rate oscillations, resulting from acoustic perturbations, occur after a convective time delay. A model including this time delay was already derived in [Faure-Beaulieu and Noiray 2020]. The inclusion of it would however necessitate the characterization of an extra parameter which is not possible in a robust manner by using the acoustic pressure signals only. A good way to identify this parameter could be to acquire a synchronized measure of the heat release rate of each flame via high speed imaging from the top. Nonetheless, as the time delay is expected to be short compared to the inverse of the thermoacoustic growth rate, only small changes in the phase space topology are expected.

- The simple flame model used in the present work is only valid close to the bifurcation. More elaborate flame models, for example higher order polynomials or sigmoid-type functions, have already been used for investigations of single sector flames [Bonciolini et al. 2021, Lee et al. 2021] and could be applied for studies of azimuthal combustion instabilities. Depending on the model, the complexity of the slow-flow equations will increase and the parameter identification could be complicated. Another way would be to measure the flame response in terms of a FTF/FDF on a single-flame experiment and include this into the low-order model. Preliminary tests on this task were performed, but unsuccessful as the flame was self-excited at the corresponding operating conditions, thereby hindering a measurement of the flame response to a controlled excitation.

- Also, in the current approach, the flame model does not depend on the azimuthal acoustic velocity in the annular chamber. Such a flame model has for example been proposed by [Ghirardo and Juniper 2013]. This led to a number of experimental investigations focusing on the effect of transverse forcing on the flame response. Subsequently, an improved flame model could consider the interaction between disturb-

ances initiated by the axial and transverse components of the acoustic velocity.

- In its current form the low-order model is not able to explain the phenomenon of periodic switching of the spinning direction which was observed in Article VI. The regularity of this phenomenon suggests that it is not purely driven by the turbulent noise, but governed by a deterministic effect. This differentiates this switching mode significantly from the switching modes that are observed and explained in Articles I and II. Work on introducing a reactive asymmetry, which can emerge from small geometrical or thermal asymmetries, and can lead to this type of beating phenomenon is currently ongoing and shows great promise in reproducing the dynamics.

The development of the pressurized annular combustor is still in a very early stage. A lot of time was spent fixing mechanical and operational issues of the initial design, now allowing for extensive investigations in a very modular experimental facility. The only mechanical problem that still needs some attention, is the leaking issue of the water cooling circuit due to extremely sensitive graphite gaskets.

The investigations, which are presented in this thesis, target a very broad view on azimuthal combustion instabilities to get an overview of the new combustor. Future work will concentrate on more specific phenomena:

- Several extensions for the presented works are currently ongoing. The observed high-amplitude instabilities with significant harmonic components led to a strong distortion of the flame, which made it strongly asymmetric and the line-of-sight integrated measurement of the heat release rate via high speed imaging less meaningful. To resolve the 3D flame structure, more complex diagnostics like OH* PLIF (planar laser-induced fluorescence) or even scanning OH* PLIF will be performed to investigate the response of the flame in more detail.

- In the scope of the effect of transverse forcing onto the flame, future works will also aim to differentiate between transverse and longitudinal oscillations perturbing the flames and relating these perturbations to the flame response. This will provide valuable results that could be compared to forced single sector experiments which are currently used to investigate these effects.

- In real gas turbine engines, the fresh air entering the combustor is heated due to the compressor stage. To achieve more realistic boundary conditions, a preheater was recently installed that allows to preheat the air to around 300 °C before it enters the combustor. However, the preheater has yet to be tested in reactive conditions and its effect on the combustion instabilities is so far unknown and remains future work.

- Under atmospheric conditions, the modal dynamics of the azimuthal combustion instabilities differed significantly for swirled and unswirled injectors, due to the effect of an azimuthal bulk flow. For both the atmospheric experiments and also the initial tests in the pressurized combustor, clearly predominant spinning mode directions were observed with few switches to the opposite spinning direction. A logical next step is to investigate the pressurized combustor with injectors without swirl, thereby removing the effect of the induced bulk swirl. If similar states as in the atmospheric combustor can be observed, with stochastic switches between spinning directions, the relation of the harmonic components will be of interest, e.g. does the state of the harmonic components follow the dynamics of the state of the fundamental mode or is it independent?

- Until now, the pressurized combustor is ignited with a pilot flame, which allows a relatively safe and controlled light-around of the system. In industrial engines, the light around is initiated with one or several spark ignitor units. Ignition studies on annular laboratory-combustors have been done at atmospheric conditions but not at pressurized conditions yet. This might extend our knowledge of phenomena controlling the light-around at more realistic boundary conditions. The spark ignition unit was recently designed an manufactured. It's commissioning and the investigations remain future work.

- The complexity of this system, with high pressure, a preheater unit and a reflecting outlet condition mimicking the turbine stage allows investigations under more realistic conditions with well-defined boundary conditions. These efforts have been undertaken to place this setup as a base-line case for numerical and theoretical investigations targeting both method validation and the investigation of phenomena that are not yet understood. Therefore several collaborations with international research facilities and companies are currently initiated.

The third objective of this work focuses on the effect of transient operating

conditions on azimuthal combustion instabilities. This objective is motivated by increasing demands of gas turbine engines towards flexible loads. In this work, the flexible load is mimicked through equivalence ratio ramps. However, in real gas turbine engines, the power of the engine is ramped, which is expected to have a significantly different effect than the equivalence ratio ramps. Future work could therefore concentrate on performing transient investigations where the power in the combustor is varied instead of the equivalence ratio.

The current investigation revealed different hysteresis phenomena affecting the stability of the combustor. Nonetheless, without modelling of these phenomena, as done for the stationary operating conditions in Articles I and II, the cause of them remains hidden, troubling a possible exploitation of positive effects (as the stabilizing hysteresis effect in Article VI) in real configurations.

Bibliography

Power-to-x: Decarbonizing energy with green hydrogen: Technology available and proven in production today. Technical report, Siemens, 2019.

M. Åbom. Measurement of the scattering-matrix of acoustical two-ports. *Mech. Syst. Signal Pr.*, 5:89–104, mar 1991.

V. Acharya and T. Lieuwen. Response of non-axisymmetric premixed, swirl flames to helical disturbances. In *Volume 4B: Combustion, Fuels and Emissions*. American Society of Mechanical Engineers, jun 2014.

V. Acharya, Shreekrishna, D.-H. Shin, and T. Lieuwen. Swirl effects on harmonically excited, premixed flame kinematics. *Combustion and Flame*, 159(3):1139–1150, mar 2012.

E. Æsøy, J. G. Aguilar, S. Wiseman, M. R. Bothien, N. A. Worth, and J. R. Dawson. Scaling and prediction of transfer functions in lean premixed h2/CH4-flames. *Combustion and Flame*, 215:269–282, may 2020.

E. Æsøy, J. G. Aguilar, N. A. Worth, and J. R. Dawson. The response of an axisymmetric jet placed at various positions in a standing wave. *Journal of Fluid Mechanics*, 917, apr 2021.

M. Bauerheim, P. Salas, F. Nicoud, and T. Poinsot. Symmetry breaking of azimuthal thermo-acoustic modes in annular cavities: a theoretical study. *Journal of Fluid Mechanics*, 760:431–465, nov 2014.

M. Bauerheim, M. Cazalens, and T. Poinsot. A theoretical study of mean azimuthal flow and asymmetry effects on thermo-acoustic modes in annular combustors. *Proceedings of the Combustion Institute*, 35(3):3219–3227, 2015.

M. Bauerheim, F. Nicoud, and T. Poinsot. Progress in analytical methods to predict and control azimuthal combustion instability modes in annular chambers. *Physics of Fluids*, 28(2):021303, feb 2016.

B. D. Bellows, M. K. Bobba, A. Forte, J. M. Seitzman, and T. Lieuwen. Flame transfer function saturation mechanisms in a swirl-stabilized combustor. *Proceedings of the Combustion Institute*, 31(2):3181–3188, jan 2007.

V. Bellucci, P. Flohr, C. O. Paschereit, and F. Magni. On the use of Helmholtz resonators for damping acoustic pulsations in industrial gas turbines. *Journal of Engineering for Gas Turbines and Power*, 126(2):271–275, apr 2004.

P. Berenbrink and S. Hoffmann. Suppression of dynamic combustion instabilities by passive and active means. *ASME TURBO EXPO 2000-GT-0079*, 2000.

G. Bonciolini, D. Ebi, U. Doll, M. Weilenmann, and N. Noiray. Effect of wall thermal inertia upon transient thermoacoustic dynamics of a swirl-stabilized flame. *Proceedings of the Combustion Institute*, 37(4):5351–5358, 2019a.

G. Bonciolini, D. Ebi, U. Doll, M. Weilenmann, and N. Noiray. Effect of wall thermal inertia upon transient thermoacoustic dynamics of a swirl-stabilized flame. *Proc. Combust. Inst.*, 37:5351–5358, 2019b.

G. Bonciolini, A. Faure-Beaulieu, C. Bourquard, and N. Noiray. Low order modelling of thermoacoustic instabilities and intermittency: Flame response delay and nonlinearity. *Combustion and Flame*, 226:396–411, apr 2021.

M. R. Bothien, N. Noiray, and B. Schuermans. Analysis of azimuthal thermo-acoustic modes in annular gas turbine combustion chambers. *Journal of Engineering for Gas Turbines and Power*, 137(6), jun 2015.

M. R. Bothien, A. Ciani, J. P. Wood, and G. Fruechtel. Toward decarbonized power generation with gas turbines by using sequential combustion for burning hydrogen. *J. Eng. Gas Turbines Power*, 141:121013, nov 2019.

J. Bourgouin, D. Durox, J. Moeck, T. Schuller, and S. Candel. A new pattern of instability observed in an annular combustor: The slanted mode. *Proceedings of the Combustion Institute*, 35(3):3237–3244, 2015.

J.-F. Bourgouin, D. Durox, J. P. Moeck, T. Schuller, and S. Candel. Self-sustained instabilities in an annular combustor coupled by azimuthal and longitudinal acoustic modes. In *Volume 1B: Combustion, Fuels and Emissions*. American Society of Mechanical Engineers, jun 2013.

J.-F. Bourgouin, D. Durox, J. P. Moeck, T. Schuller, and S. Candel. Characterization and modeling of a spinning thermoacoustic instability in an annular combustor equipped with multiple matrix injectors. *Journal of Engineering for Gas Turbines and Power*, 137(2), sep 2014.

P. Breeze. *Power generation technologies*. Elsevier, 2019.

S. Candel. Combustion dynamics and control: Progress and challenges. *Proceedings of the Combustion Institute*, 29(1):1–28, jan 2002.

B.-T. Chu. On the energy transfer to small disturbances in fluid flow (part i). *Acta Mechanica*, 1(3):215–234, sep 1965.

J. D. Crawford and E. Knobloch. Symmetry and symmetry-breaking bifurcations in fluid dynamics. *Annual Review of Fluid Mechanics*, 23(1): 341–387, jan 1991.

L. Crocco. Aspects of combustion stability in liquid propellant rocket motors part i: Fundamentals. low frequency instability with monopropellants. *Journal of the American Rocket Society*, 21(6):163–178, nov 1951.

L. Crocco and S. Cheng. Theory of combustion instabilitiy in liquid propellant rocket motors. *Agardograph No. 8*, 1956.

L. Crocco, J. Grey, and D. Harrje. Theory of liquid Propellant rocket combustion instability and its experimental verification. *ARS Journal*, 30 (2):159–168, feb 1960.

J. R. Dawson and N. A. Worth. The effect of baffles on self-excited azimuthal modes in an annular combustor. *Proceedings of the Combustion Institute*, 35(3):3283–3290, 2015.

N. Dickson. Local air quality and icao engine emissions standards. *Presented at ICAO Environmental Workshop*, 2014.

N. Docquier, S. Belhalfaoui, F. Lacas, N. Darabiha, and C. Rolon. Experimental and numerical study of chemiluminescence in methane/air high-pressure flames for active control applications. *Proceedings of the Combustion Institute*, 28(2):1765–1774, jan 2000.

A. P. Dowling. A kinematic model of a ducted flame. *Journal of Fluid Mechanics*, 394:51–72, sep 1999.

S. Ducruix, D. Durox, and S. Candel. Theoretical and experimental determinations of the transfer function of a laminar premixed flame. *Proceedings of the Combustion Institute*, 28(1):765–773, jan 2000.

I. D. J. Dupere and A. P. Dowling. The use of Helmholtz resonators in a practical combustor. *Journal of Engineering for Gas Turbines and Power*, 127(2):268–275, apr 2005.

D. Eckhardt. *Gas Turbine Powerhouse: The Development of the Power Generation Gas Turbine at BBC - ABB - Alstom.* De Gruyter Oldenbourg, 2014.

EPA. U.S. environmental protection agency. integrated science assessment for oxides of nitrogen – health critera. *EPA/600/R-15/068*, 2016.

A. Faure-Beaulieu and N. Noiray. Symmetry breaking of azimuthal waves: Slow-flow dynamics on the Bloch sphere. *Phys. Rev. Fluids*, 5:023201, feb 2020.

L. Garrow and V. Lurkin. How COVID-19 is impacting and reshaping the airline industry. *Journal of Revenue and Pricing Management*, 20(1):3–9, jan 2021.

G. Ghirardo and M. R. Bothien. Quaternion structure of azimuthal instabilities. *Physical Review Fluids*, 3(11), nov 2018.

G. Ghirardo and F. Gant. Background noise pushes azimuthal instabilities away from spinning states. 2019.

G. Ghirardo and M. P. Juniper. Azimuthal instabilities in annular combustors: standing and spinning modes. *Proceedings of the Royal Society A: Mathematical, Physical and Engineering Sciences*, 469(2157):20130232, sep 2013.

G. Ghirardo, M. P. Juniper, and J. P. Moeck. Weakly nonlinear analysis of thermoacoustic instabilities in annular combustors. *Journal of Fluid Mechanics*, 805:52–87, sep 2016.

G. Ghirardo, H. T. Nygård, A. Cuquel, and N. A. Worth. Symmetry breaking modelling for azimuthal combustion dynamics. *Proceedings of the Combustion Institute*, jul 2020.

L. C. Haber, U. Vandsburger, W. R. Saunders, and V. K. Khanna. An examination of the relationship between chemiluminescent light emissions and heat release rate under non-adiabatic conditions. In *Volume 2: Coal, Biomass and Alternative Fuels; Combustion and Fuels; Oil and Gas Applications; Cycle Innovations*. American Society of Mechanical Engineers, may 2000.

X. Han, J. Li, and A. S. Morgans. Prediction of combustion instability limit cycle oscillations by combining flame describing function simulations with a thermoacoustic network model. *Combustion and Flame*, 162(10):3632–3647, oct 2015.

M. Hauser, M. Lorenz, and T. Sattelmayer. Influence of transversal acoustic excitation of the burner approach flow on the flame structure. *Journal of Engineering for Gas Turbines and Power*, 133(4), nov 2010.

C. Hirsch, D. Fanaca, P. Reddy, W. Polifke, and T. Sattelmayer. Influence of the swirler design on the flame transfer function of premixed flames. In *Volume 2: Turbo Expo 2005*. , jan 2005.

S. Hong, S. J. Shanbhogue, K. S. Kedia, and A. F. Ghoniem. Impact of the flame-holder heat-transfer characteristics on the onset of combustion instability. *Combustion Science and Technology*, 185(10):1541–1567, oct 2013.

G. Hsiao, R. Pandalai, H. Hura, and H. Mongia. Combustion dynamic modeling for gas turbine engines. In *34th AIAA/ASME/SAE/ASEE Joint Propulsion Conference and Exhibit*. American Institute of Aeronautics and Astronautics, jul 1998.

I. J. Hughes and A. P. Dowling. The absorption of sound by perforated linings. *Journal of Fluid Mechanics*, 218(-1):299, sep 1990.

S. C. Humbert, J. Moeck, A. Orchini, and C. O. Paschereit. Effect of an azimuthal mean flow on the structure and stability of thermoacoustic modes in an annular combustor model with electroacoustic feedback. *Journal of Engineering for Gas Turbines and Power*, oct 2020.

T. Hummel, F. Berger, N. Stadlmair, B. Schuermans, and T. Sattelmayer. Extraction of linear growth and damping rates of high-frequency thermoacoustic oscillations from time domain data. In *Volume 4A: Combustion, Fuels and Emissions*. American Society of Mechanical Engineers, jun 2017a.

T. Hummel, K. Hammer, P. Romero, B. Schuermans, and T. Sattelmayer. Low-order modeling of nonlinear high-frequency transversal thermoacoustic oscillations in gas turbine combustors. *Journal of Engineering for Gas Turbines and Power*, 139(7), feb 2017b.

I. R. Hurle, R. B. Price, T. M. Sugden, and A. Thomas. Sound emission from open turbulent premixed flames. *Proceedings of the Royal Society of London. Series A. Mathematical and Physical Sciences*, 303(1475):409–427, mar 1968.

IATA. The international air transport associations, 20-year air passenger forcast. 2016. URL https://www.iata.org/en/publications/store/20-year-passenger-forecast/.

T. Indlekofer, B. Ahn, Y. H. Kwah, S. Wiseman, M. Mazur, J. R. Dawson, and N. A. Worth. The effect of hydrogen addition on the amplitude and harmonic response of azimuthal instabilities in a pressurized annular combustor. *Combustion and Flame*, 228:375–387, jun 2021a.

T. Indlekofer, A. Faure-Beaulieu, N. Noiray, and J. Dawson. The effect of dynamic operating conditions on the thermoacoustic response of hydrogen rich flames in an annular combustor. *Combustion and Flame*, 223:284–294, jan 2021b.

T. Indlekofer, A. Faure-Beaulieu, N. Noiray, and J. Dawson. Spontaneous and explicit symmetry breaking of thermoacoustic eigenmodes in annular geometries. *Physical Review Letters (under review)*, 2021c.

IPCC. Summary for policymakers. In I. P. on Climate Change, editor, *Climate Change 2013 - The Physical Science Basis*, pages 1–30. Cambridge University Press, 2013a.

IPCC. Technical summary. In I. P. on Climate Change, editor, *Climate Change 2013 - The Physical Science Basis*, pages 31–116. Cambridge University Press, 2013b.

S. Jaensch, M. Merk, T. Emmert, and W. Polifke. Identification of flame transfer functions in the presence of intrinsic thermoacoustic feedback and noise. *Combustion Theory and Modelling*, 22(3):613–634, mar 2018.

P. Jansohn. *Modern gas turbine systems: high efficiency, low emission, fuel flexible power generation*. Woodhead Publishing, Oxford, 2016. ISBN 0081013841.

JulHoltz, G. Mensah, and A. Orchini. Julia package for handling various wave equations and (non-linear) eigenvalue problems: https://github.com/JulHoltzDevelopers/WavesAndEigenvalues.jl.

K. Kim, J. Lee, B. Quay, and D. Santavicca. Spatially distributed flame transfer functions for predicting combustion dynamics in lean premixed gas turbine combustors. *Combustion and Flame*, 157(9):1718–1730, sep 2010.

L. V. King. XII. on the convection of heat from small cylinders in a stream of fluid: Determination of the convection constants of small platinum wires with applications to hot-wire anemometry. *Philosophical Transactions of the Royal Society of London. Series A, Containing Papers of a Mathematical or Physical Character*, 214(509-522):373–432, jan 1914.

P. Knoop, F. Culick, and E. Zukoski. Extension of the stability of motions in a combustion chamber by nonlinear active control based on hysteresis. *Combust. Sci. Tech.*, 123:363–376, jan 1997.

J. C. Koj, C. Wulf, and P. Zapp. Environmental impacts of power-to-x systems - a review of technological and methodological choices in life cycle assessments. *Renewable and Sustainable Energy Reviews*, 112:865–879, sep 2019.

W. Krebs, G. Walz, and S. Hoffmann. Thermoacoustic analysis of annular combustors. *AIAA A99-27906*, 1999.

W. Krebs, P. Flohr, B. Prade, and S. Hoffmann. Thermoacoustic stability chart for high intensity gas turbine combustion systems. *Combust. Sci. andTech., 174(7): 99-128*, 2002.

D. Laera, T. Schuller, K. Prieur, D. Durox, S. M. Camporeale, and S. Candel. Flame describing function analysis of spinning and standing modes in an annular combustor and comparison with experiments. *Combustion and Flame*, 184:136–152, oct 2017.

M. Lee, K. T. Kim, V. Gupta, and L. K. Li. System identification and early warning detection of thermoacoustic oscillations in a turbulent combustor using its noise-induced dynamics. *Proceedings of the Combustion Institute*, 38(4):6025–6033, 2021.

A. Lefebvre and D. Ballal. *Gas turbine combustion: Alternative fuels and emissions.* CRC PressTaylor & Francis Group, 2010.

T. Lieuwen. Modeling premixed combustion-acoustic wave interactions: A review. *Journal of Propulsion and Power*, 19(5):765–781, sep 2003.

T. Lieuwen and V. Yang. *Combustion Instabilities In Gas Turbine Engines: Operational Experience, Fundamental Mechanisms, and Modeling*. American Institute of Aeronautics and Astronautics, Inc., 2005.

Lord Rayleigh. The explanaition of certain acoustic phenomena. *Nature*, 18:319–321, 1878.

L. Magri, M. P. Juniper, and J. P. Moeck. Sensitivity of the rayleigh criterion in thermoacoustics. *Journal of Fluid Mechanics*, 882, nov 2019.

S. Manikandan and R. Sujith. Rate dependent transition to thermoacoustic instability via intermittency in a turbulent afterburner. *Exp. Therm. Fluid Sci.*, 114:110046, 2020.

M. Mazur, H. T. Nygård, J. R. Dawson, and N. A. Worth. Characteristics of self-excited spinning azimuthal modes in an annular combustor with turbulent premixed bluff-body flames. *Proc. Combust. Inst.*, 37:5129–5136, 2019.

M. Mazur, Y.-H. Kwah., T. Indlekofer, J. R. Dawson, and N. A. Worth. Self-excited longitudinal and azimuthal modes in a pressurized annular combustor. *Proc. Combust. Inst. (in press)*, 2020.

K. McManus, T. Poinsot, and S. Candel. A review of active control of combustion instabilities. *Progress in Energy and Combustion Science*, 19 (1):1–29, jan 1993.

D. Mejia, M. Miguel-Brebion, A. Ghani, T. Kaiser, F. Duchaine, L. Selle, and T. Poinsot. Influence of flame-holder temperature on the acoustic flame transfer functions of a laminar flame. *Combustion and Flame*, 188: 5–12, feb 2018.

M. Miguel-Brebion, D. Mejia, P. Xavier, F. Duchaine, B. Bedat, L. Selle, and T. Poinsot. Joint experimental and numerical study of the influence of flame holder temperature on the stabilization of a laminar methane flame on a cylinder. *Combustion and Flame*, 172:153–161, oct 2016.

R. K. Mobley. Predictive maintenance. In *Plant Engineer's Handbook*, pages 867–888. Elsevier, 2001.

A. Morgans and S. Stow. Model-based control of combustion instabilities in annular combustors. *Combustion and Flame*, 150(4):380–399, sep 2007.

M. A. Nemitallah, S. S. Rashwan, I. B. Mansir, A. A. Abdelhafez, and M. A. Habib. Review of novel combustion techniques for clean power production in gas turbines. *Energy & Fuels*, 32(2):979–1004, jan 2018.

F. Nicoud and T. Poinsot. Thermoacoustic instabilities: Should the rayleigh criterion be extended to include entropy changes? *Comb. Flame 142 (1-2), pp. 153-159*, 2005.

N. Noiray. Linear growth rate estimation from dynamics and statistics of acoustic signal envelope in turbulent combustors. *Journal of Engineering for Gas Turbines and Power*, 139(4), oct 2016.

N. Noiray and B. Schuermans. On the dynamic nature of azimuthal thermoacoustic modes in annular gas turbine combustion chambers. *Proceedings of the Royal Society A: Mathematical, Physical and Engineering Sciences*, 469(2151):20120535, mar 2013.

N. Noiray, D. Durox, T. Schuller, and S. Candel. A unified framework for nonlinear combustion instability analysis based on the flame describing function. *Journal of Fluid Mechanics*, 615:139–167, nov 2008.

N. Noiray, M. Bothien, and B. Schuermans. Investigation of azimuthal staging concepts in annular gas turbines. *Combustion Theory and Modelling*, 15(5):585–606, oct 2011.

H. T. Nygård, M. Mazur, J. R. Dawson, and N. A. Worth. Flame dynamics of azimuthal forced spinning and standing modes in an annular combustor. *Proceedings of the Combustion Institute*, 37(4):5113–5120, 2019.

H. T. Nygård, G. Ghirardo, and N. A. Worth. Azimuthal flame describing functions and symmetry breaking in an azimuthally forced annular combustor. *Combustion and Flame (under review)*, 2021.

J. O'Connor and T. Lieuwen. Disturbance field characteristics of a transversely excited burner. *Combustion Science and Technology*, 183(5):427–443, feb 2011.

J. O'Connor and T. Lieuwen. Recirculation zone dynamics of a transversely excited swirl flow and flame. *Physics of Fluids*, 24(7):075107, jul 2012.

J. O'Connor, V. Acharyab, and T. Lieuwen. Transverse combustion instabilities: Acoustic, fluid mechanic, and flame processes. *Prog. Energy Combust. Science*, 49:1–39, 2015.

J. C. Oefelein and V. Yang. Comprehensive review of liquid-propellant combustion instabilities in f-1 engines. *J. Prop. Power*, 9(5), 1993.

J.-F. Parmentier, P. Salas, P. Wolf, G. Staffelbach, F. Nicoud, and T. Poinsot. A simple analytical model to study and control azimuthal instabilities in annular combustion chambers. *Combustion and Flame*, 159(7):2374–2387, jul 2012.

C. Paschereit, B. Schuermans, and P. Monkewitz. Non-linear combustion instabilities in annular gas-turbine combustors. In *44th AIAA Aerospace Sciences Meeting and Exhibit*. American Institute of Aeronautics and Astronautics, jan 2006.

T. Poinsot. Prediction and control of combustion instabilities in real engines. *Proceedings of the Combustion Institute*, 36(1):1–28, 2017.

W. Polifke and C. Lawn. On the low-frequency limit of flame transfer functions. *Combustion and Flame*, 151(3):437–451, nov 2007.

K. Prieur, D. Durox, T. Schuller, and S. Candel. A hysteresis phenomenon leading to spinning or standing azimuthal instabilities in an annular combustor. *Combustion and Flame*, 175:283–291, jan 2017.

A. Roy, S. Singh, A. Nair, S. Chaudhuri, and R. Sujith. Flame dynamics during intermittency and secondary bifurcation to longitudinal thermoacoustic instability in a swirl-stabilized annular combustor. *Proceedings of the Combustion Institute*, oct 2020.

A. Saurabh and C. O. Paschereit. Combustion instability in a swirl flow combustor with transverse extensions. In *Volume 1B: Combustion, Fuels and Emissions*. American Society of Mechanical Engineers, jun 2013.

A. Saurabh and C. O. Paschereit. Dynamics of premixed swirl flames under the influence of transverse acoustic fluctuations. *Combustion and Flame*, 182:298–312, aug 2017.

A. Saurabh and C. O. Paschereit. Premixed flame dynamics in response to two-dimensional acoustic forcing. *Combustion Science and Technology*, 191(7):1184–1200, sep 2018.

A. Saurabh, R. Steinert, J. P. Moeck, and C. O. Paschereit. Swirl flame response to traveling acoustic waves. In *Volume 4B: Combustion, Fuels and Emissions*. American Society of Mechanical Engineers, jun 2014.

B. Schuermans, V. Bellucci, and C. O. Paschereit. Thermoacoustic modeling and control of multi burner combustion systems. In *Volume 2: Turbo Expo 2003*. , jan 2003.

T. Schuller, D. Durox, and S. Candel. A unified model for the prediction of laminar flame transfer functions. *Combustion and Flame*, 134(1-2):21–34, jul 2003.

T. Schuller, T. Poinsot, and S. Candel. Dynamics and control of premixed combustion systems based on flame transfer and describing functions. *Journal of Fluid Mechanics*, 894, may 2020.

J. R. Seume, N. Vortmeyer, W. Krause, J. Hermann, C.-C. Hantschk, P. Zangl, S. Gleis, D. Vortmeyer, and A. Orthmann. Application of active combustion instability control to a heavy duty gas turbine. *Journal of Engineering for Gas Turbines and Power*, 120(4):721–726, oct 1998.

A. F. Seybert and D. F. Ross. Experimental determination of acoustic properties using a two-microphone random-excitation technique. *The Journal of the Acoustical Society of America*, 61(5):1362–1370, may 1977.

S. Singh, A. Roy, R. K. V., A. Nair, S. Chaudhuri, and R. I. Sujith. Intermittency, secondary bifurcation and mixed-mode oscillations in a swirl-stabilized annular combustor: Experiments and modeling. *Journal of Engineering for Gas Turbines and Power*, dec 2020.

N. Syred and J. Beér. Combustion in swirling flows: A review. *Combustion and Flame*, 23(2):143–201, oct 1974.

G. Vignat, D. Durox, A. Renaud, and S. Candel. High amplitude combustion instabilities in an annular combustor inducing pressure field deformation and flame blow-off. In *Volume 4A: Combustion, Fuels, and Emissions*. American Society of Mechanical Engineers, jun 2019.

G. Vignat, D. Durox, T. Schuller, and S. Candel. Combustion dynamics of annular systems. *Combustion Science and Technology*, 192(7):1358–1388, mar 2020.

P. Wolf, G. Staffelbach, L. Y. Gicquel, J.-D. MÃijller, and T. Poinsot. Acoustic and large eddy simulation studies of azimuthal modes in annular combustion chambers. *Combustion and Flame*, 159(11):3398–3413, 2012. ISSN 0010-2180.

N. A. Worth and J. R. Dawson. Modal dynamics of self-excited azimuthal instabilities in an annular combustion chamber. *Combust. Flame*, 160: 2476–2489, nov 2013a.

N. A. Worth and J. R. Dawson. Self-excited circumferential instabilities in a model annular gas turbine combustor: Global flame dynamics. *Proc. Combust. Inst.*, 34:3127–3134, jan 2013b.

B. T. Zinn and T. C. Lieuwen. *Combustion Instabilities In Gas Turbine Engines: Operational Experience, Fundamental Mechanisms, and Modeling*, chapter 1: Combustion Instabilities: Basic Concepts, pages 1–26. 2005.

Article I

Spontaneous and explicit symmetry breaking of thermoacoustic eigenmodes in annular geometries

Thomas Indlekofer, Abel Faure-Beaulieu, Nicolas Noiray
and James R. Dawson

Experiments and low-order modelling of intermittent transitions between clockwise and anticlockwise spinning thermoacoustic modes in annular combustors

Abel Faure-Beaulieu, Thomas Indlekofer, James R. Dawson and Nicolas Noiray

Experiments and low-order modelling of intermittent transitions between clockwise and anticlockwise spinning thermoacoustic modes in annular combustors

Abel Faure-Beaulieu [a,*], Thomas Indlekofer [b], James R. Dawson [b], Nicolas Noiray [a,*]

[a] *CAPS Laboratory, Department of Mechanical and Process Engineering, ETH Zürich, Switzerland*
[b] *Department of Energy and Process Engineering, Norwegian University of Science and Technology, Norway*

Abstract

Annular combustion chambers of gas turbines and aircraft engines are subject to unstable azimuthal thermoacoustic modes leading to high amplitude acoustic waves propagating in the azimuthal direction. For certain operating conditions, the propagating direction of the wave switches randomly. The strong turbulent noise prevailing in gas turbine combustors is a source of random excitation for the thermoacoustic modes and can be the cause of these switching events. A low-order model is proposed to describe qualitatively this property of the dynamics of thermoacoustic azimuthal modes. This model is based on the acoustic wave equation with a destabilizing thermoacoustic source term to account for the flame's response and a stochastic term to account for the turbulent combustion noise. Slow-flow averaging is applied to describe the modal dynamics on times scales that are slower than the acoustic pulsation. Under certain conditions, the model reduces formally to a Fokker-Planck equation describing a stochastic diffusion process in a potential landscape with two symmetric wells: One well corresponds to a mode propagating in the clockwise direction, the other well corresponds to a mode propagating in the anticlockwise direction. When the level of turbulent noise is sufficient, the stochastic force makes the mode jump from one well to the other at random times, reproducing the phenomenon of direction switching. Experiments were conducted on a laboratory scale annular combustor featuring 12 hydrogen-methan flames. System identification techniques were used to fit the model on the experimental data, allowing to extract the potential shape and the intensity of the stochastic excitation. The

* Corresponding authors.
  E-mail addresses: abelf@ethz.ch (A. Faure-Beaulieu), noirayn@ethz.ch (N. Noiray).

statistical predictions obtained from the Fokker–Planck equation on the mode's behaviour and the direction switching time are in good agreement with the experiments.

1. Introduction

Thermoacoustic instabilities are a major issue in the development of new aeroengines combustion chambers aligned with the current ecological challenges because they induce vibrations that can severely damage the combustor and the turbine. The seriousness of this problem lies in the fact that despite decades of intense research, these instabilities are still very difficult to predict, which calls for further advances in their modelling and understanding [1]. The present study falls within this context and deals with the modelling of an intriguing phenomenon occuring in annular aeroengine combustors: the intermittent transitions between clockwise and counterclockwise spinning thermoacoustic modes. Indeed, in modern aeroengines, the combustor is annular, which has advantages in terms of weight, maintenance and manufacturing, and the instabilities frequently involve the first azimuthal eigenmodes of the annulus. Based on acoustic measurements in the combustors of practical gas turbines [2,3], in academic annular chambers [4–6] and on high fidelity numerical simulations [7], these self-sustained azimuthal thermoacoustic modes have been classified as *spinning modes* that propagate at the speed of sound in the clockwise or the anticlockwise direction, *standing modes* whose nodal line stays at a constant azimuthal position or drifts slowly compared to the speed of sound, or *mixed modes* that result from the sum of a standing mode and a spinning mode. Many studies dealing with the dynamics of these modes have been published over the last ten years, covering several aspects of the underlying physics such as the effects of spatial asymmetries, turbulent combustion noise, mean azimuthal flow or specific types of nonlinearities in the flame response, e.g. [8–13]. However, no detailed studies have been published on the intermittent transition events between mixed and standing modes and between clockwise-spinning and anticlockwise-spinning mixed modes. This paper aims at filling this gap with new experimental data and a low-order model, which is derived from first principles and describes the stochastic dynamics of these transitions in the same way as thermally activated barrier crossing in reaction rate theory [14].

The experimental setup and data are presented in Section 2. Section 3 presents the low-order model. In Section 4, the validity of this model is assessed using the experimental data, and its parameters are identified. Section 5 introduces the potential representation. The calibrated model is then used in Section 6 to shed light on the mechanisms associated with the intermittent transitions of the spinning direction.

2. Experiments

Fig. 1a shows the experimental setup used in this study. It consists in an annular combustion chamber at atmospheric pressure, with 12 regularly spaced flames anchored on axisymmetric bluff bodies. The fuel is a gaseous mixture of CH_4 (contributing to 30% of the thermal power) and H_2 (70% of the thermal power) that are premixed in a plenum. The inner and outer walls of the chamber are cooled with water. The setup is described more in detail in [15]. Acoustic measurements are performed with 6 pressure transducers Kulite XCS-093-05D flush mounted in the burner's pipes at equidistant azimuthal positions. All the experiments are run with the same thermal power of $12 \times 6 = 72$ kW and equivalence ratios Φ comprised between 0.4 and 0.62. This is achieved by keeping the fuel mass flow constant at 320 sl/min and by varying the air mass flow between 2600 sl/min and 1670 sl/min. The mass flows are controlled with several Alicat mass flow controllers. Fig. 1b shows the evolution of the acoustic amplitude for different equivalence ratios: The signature of a supercritical Hopf bifurcation is detected from the acoustic time traces when Φ is increased: below 0.4, the system is stable. The Hopf point is located at $\Phi = 0.51$: above this value, a thermoacoustic instability is detected. To ensure stationarity of the thermoacoustic dynamics, acoustic records are performed at least 60 s after ignition at each operating points so that thermal transient behavior of the combustor has ended. At this time, the measured inner wall temperature and acoustic root-mean-square amplitudes are stabilized. In this paper, we focus on three specific operating points to illustrate our conclusions: $\Phi = 0.525$, $\Phi = 0.55$ and $\Phi = 0.60$. The equivalence ratios at these conditions are beyond the Hopf point and the associated acoustic spectra are dominated by one single peak close to 1.1 kHz, which corresponds to an acoustic eigenmode with one wavelength spanning the circumference of the annular chamber. Fig. 2
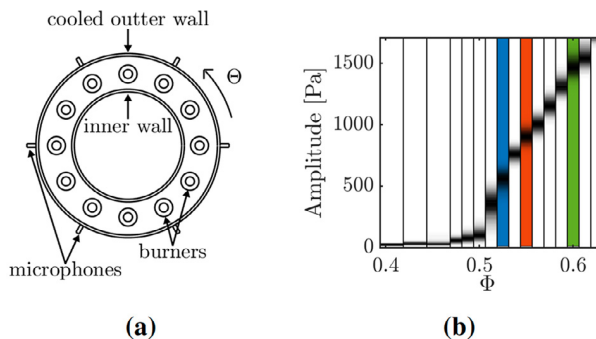
(a)   **(b)**

Fig. 1. **(a)**: Sketch view from the top of the chamber with the 12 burners and the location of the 6 microphones. **(b)**: measured PDF of the acoustic amplitude A for different equivalence ratios. The colors correspond to the 3 cases studied in the paper: $\Phi = 0.525$, $\Phi = 0.55$, $\Phi = 0.60$.
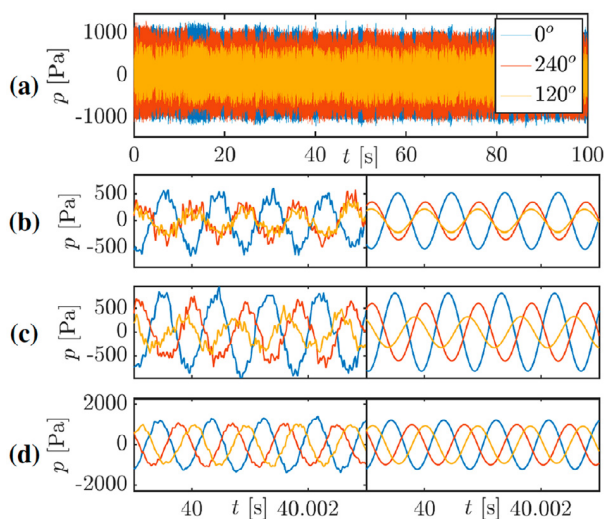

Fig. 2. **(a)**: Complete microphones time traces at 3 azimuthal locations for $\Phi = 0.55$. **(b,c,d)**: Detail of the microphones timetraces for $\Phi = 0.525$, $\Phi = 0.55$, $\Phi = 0.6$ (from the top to the bottom). Left panel: raw timetrace. Right panel: timetrace filtered with a rectangular filter of bandwidth 100 [Hz] centered around the main frequency in the spectrum.

shows portions of the corresponding acoustic pressure time series. One can see in Fig. 2b–d that the acoustic oscillations are almost sinusoidal even before applying any spectral filtering. Fig. 2b corresponds to $\Phi=0.525$, and one can conclude from the time traces that around $t = 40$ s, the acoustic oscillation corresponds to a standing mode. This is because all the microphone signals are in phase or exactly in phase opposition and exhibit different amplitudes. In Fig. 2c, the signals are not in phase and the amplitude depends on the angular position, which corresponds, at that instant, to a mixed mode. In Fig. 2d, the signals exhibit phase differences of about 120° with similar amplitudes which also corresponds to a mixed mode, but with a stronger spinning component.

At a given axial position, the pressure field associated to the first azimuthal mode is represented with the quaternion ansatz introduced in [16]:

$$\tilde{p}(\Theta, t) = A(t)e^{i(\theta(t)-\Theta)}e^{-k\chi(t)}e^{j(\omega t+\varphi(t))}. \tag{1}$$

where i, j and k are the quaternion imaginary units. The real-valued azimuthal mode state variables φ, θ, A, and χ are slowly varying in time with respect to the acoustic period $2\pi/\omega$. They describe the slow dynamics of the mode [16,17]: φ is a slow temporal phase drift, θ is the direction of the antinodal line of the pressure oscillations and A is the oscillation amplitude. The nature angle χ characterizes the mode type: $\chi = 0$ for a pure standing mode, $\chi = \pi/4$ for a pure anticlockwise spinning mode, $\chi = -\pi/4$ for a pure clockwise
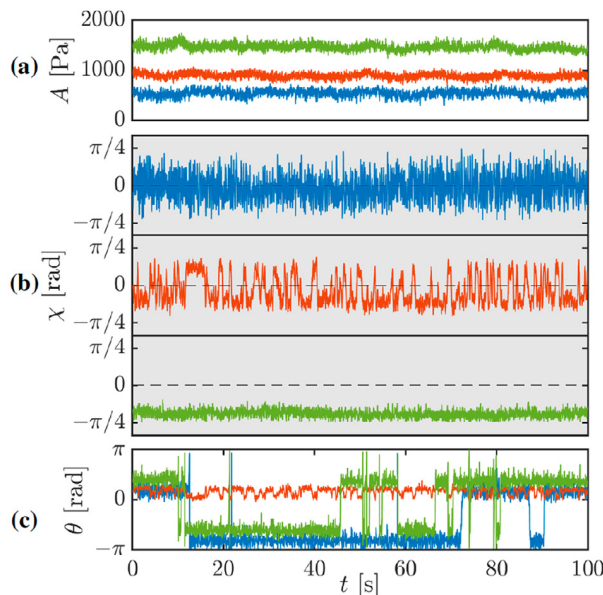
Fig. 3. Time traces of the slow-flow variables: **(a)**: A, **(b)**: χ, **(c)**: θ for 3 different equivalence ratios: $\Phi = 0.525$ (blue), dynamics centered around a standing mode. $\Phi = 0.55$ (red), dynamics switching between anticlockwise and clockwise mixed modes. $\Phi = 0.6$ (green), the mode is mixed and spins in the clockwise direction during the whole experiment.

spinning mode, $-\pi/4 > \chi > 0$ and $0 > \chi > -\pi/4$ for a anticlockwise and for a clockwise mixed mode respectively. The real pressure $p(\Theta, t)$ is obtained by taking the real part of the quaternion ansatz $\tilde{p}$. This quaternion representation describes the modal dynamics in a non-ambiguous way [16]. To obtain the time traces of the slow variables A, χ, θ and φ, we first write the pressure field associated to the first azimuthal mode with the ansatz $p(\Theta, t) = \eta_1(t)\cos(\Theta) + \eta_2(t)\sin(\Theta)$. Since the number of microphones is greater than 2, the signals η_1 and η_2 are obtained from the filtered microphones time traces by inverting an overdetermined system with a least-square method, with an error smaller than 5% for the present experiments. Then, the procedure to obtain the slow variables from the bivariate signal (η_1, η_2) is described in [16].

Fig. 3 shows the time traces of A, χ and θ for the three considered operating points ($\Phi = 0.525$, $\Phi = 0.55$ and $\Phi = 0.60$). The amplitude increases with the equivalence ratio, and the fluctuations of the amplitude A are relatively low during the 100 s of recording. For $\Phi = 0.55$, the antinodal line θ remains locked all the time in the same direction. For $\Phi = 0.525$ and $\Phi = 0.60$, θ shows some jumps between two values distant of π, which are in fact describing the same antinodal line [16]. In Fig. 4a, one can see that φ does not show a preferential value, its PDF is flat. The time derivative of φ gives information on the frequency drift. The PDF of $\dot{\varphi}$ shown in Fig. 4b suggests that this drift remains close to 0 and is small compared to the instability frequency.

The nature angle χ behaves completely differently between the three cases: for $\Phi = 0.525$, it fluctuates randomly around 0, which corresponds to a predominant standing mode state. For $\Phi = 0.55$, χ switches randomly between a positive value and its negative, which indicates a statistically dominant mixed mode whose propagating direction changes randomly. For $\Phi = 0.60$, χ is locked on a negative value close to $-\pi/4$, corresponding to an almost pure spinning mode propagating in the clockwise direction.

3. Theoretical model

We introduce now a low-order model that describes the dynamics of azimuthal thermoacoustic eigenmodes in an idealized one dimensional annular combustor. The four parameters of this model will be afterward identified from the experimental data presented in the previous section. It will be shown that the calibrated model quantitatively reproduce the dynamics of the slow-flow variables, which shows that it can used as a minimal model for describing the state of eigenmodes exhibiting an azimuthal component in real 3 dimensional combustors. It is important to stress that this model is not intended to be used for prediction of thermoacoustic stability in real systems. The chamber is modelled as a 1D annular waveguide of radius $\mathcal{R}$. The azimuthal angular coordinate is referred to as Θ. The wave equation for the acoustic pressure in the
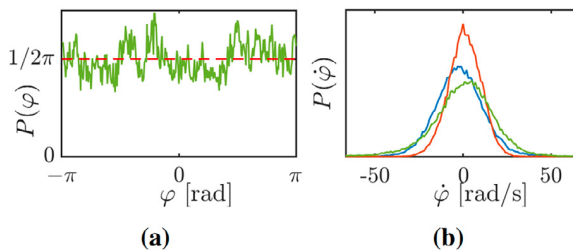
Fig. 4. **(a)**: experimental PDF of φ for $\Phi = 0.60$. **(b)**: experimental PDF of $\dot{\varphi}$ for $\Phi = 0.525$ (blue), $\Phi = 0.55$ (red), $\Phi = 0.60$ (green).

chamber in presence of a thermoacoustic source term is

$$\frac{\partial^2 p}{\partial t^2} + \alpha \frac{\partial p}{\partial t} - \frac{c^2}{\mathcal{R}^2} \frac{\partial^2 p}{\partial \Theta^2} = (\gamma - 1) \frac{\dot{Q}}{\partial t} + \Xi(\Theta, t), \tag{2}$$

where c is the speed of sound, α is the acoustic damping, γ is the heat capacity ratio, Ξ is a random forcing representing the turbulent heat release rate fluctuations, and $\dot{Q}$ is the coherent component of the heat release rate of the flames. The latter is responsible of the thermoacoustic instability phenomenon, and it is modelled with a 3rd order nonlinearity: $(\gamma - 1)\dot{Q} = \beta[1 + c_2 \cos(2\Theta)]p - \kappa p^3$, where $\beta[1 + c_2 \cos(2\Theta)]p$ influences the linear stability of the thermoacoustic modes and κp^3 governs the saturation to limit cycles [3,8,18,19]. To account for spatial asymmetries in the *coherent* heat release rate fluctuations, only the second term c_2 of the spatial Fourier expansion of the source term distribution was kept. Indeed, it was shown in previous works that it is the only term having an effect on the dynamics of the first azimuthal mode [8]. In [19], the quaternion formalism of Eq. (1) is introduced in the wave Eq. (2), and methods of spatial and slow time averaging are applied to obtain a first order system of coupled Langevin equations for A, χ, θ and φ. Based on the experimental data presented in Fig. 3, we consider that the fluctuations of the antinodal line direction are weak enough to set θ as a constant in the equations. Under these assumptions, the equations for A and χ are:

$$\begin{cases} \dot{A} = \left(\nu + \frac{c_2\beta}{4}\cos(2\chi)\right)A \\ \quad - \frac{3\kappa}{64}(5 + \cos(4\chi))A^3 + \frac{3\Gamma}{4\omega^2 A} + \zeta_A \\ \dot{\chi} = \frac{3\kappa}{64}A^2 \sin(4\chi) - \frac{c_2\beta}{4}\sin(2\chi) \\ \quad - \frac{\Gamma}{2\omega^2}\frac{\tan(2\chi)}{A^2} + \frac{1}{A}\zeta_\chi \end{cases} \tag{3}$$

where $\nu = (\beta - \alpha)/2$. The constant Γ is the intensity of the noise coming from the projection of the random fluctuation Ξ on the first azimuthal mode shape [19]. ζ_A and ζ_χ are uncorrelated gaussian noises of intensities $\Gamma/2\omega^2$. In the considered experimental time traces, A is almost constant and

will be replaced by its mean value A_0 in the equation for χ. In the equation for A, χ appears in the terms $\cos(2\chi)$ and $\cos(4\chi)$. However, for the considered experimental conditions, the standard deviation of $\cos(2\chi)$ never exceeds 0.15. Under the assumption that $c_2\beta/4$ is of the same order as ν or smaller, the fluctuations of $\cos(2\chi)$ are neglected and χ is replaced by the average value of its absolute value $\chi_0 = \langle|\chi|\rangle$. The standard deviation of $\cos(4\chi)$ in the experiments is always under 0.5, which has small effect in the sum $(5 + \cos(4\chi))$. Therefore, χ is also replaced by χ_0 in this term. The two equations are in this way decoupled:

$$\dot{A} = \left(\nu + \frac{c_2\beta}{4}\cos(2\chi_0)\right)A$$
$$\quad - \frac{3\kappa}{64}(5 + \cos(4\chi_0))A^3 + \frac{3\Gamma}{4\omega^2 A} + \zeta_A, \tag{4}$$

$$\dot{\chi} = \frac{3\kappa}{64}A_0^2 \sin(4\chi) - \frac{c_2\beta}{4}\sin(2\chi)$$
$$\quad - \frac{\Gamma}{2\omega^2}\frac{\tan(2\chi)}{A_0^2} + \frac{1}{A_0}\zeta_\chi. \tag{5}$$

In a more compact form $\dot{A} = F_A(A) + \zeta_A$ and $\dot{\chi} = F_\chi(\chi) + \zeta_\chi/A_0$, where all the deterministic terms are grouped in the functions F_A and F_χ, which are the *drift coefficients* of the Fokker–Planck (FP) equations governing the evolution of the probability density $P(A)$ and $P(\chi)$. The FP equations have also a *diffusion coefficient*. The latter is equal to $\Gamma/2\omega^2$ in the FP equation for $P(A)$.

4. Model parameters calibration

It is now interesting to make use of the experimental data to identify the model parameters, and therefore calibrate it for each of the stationary operating conditions investigated in this work. This can be achieved by following the framework proposed in [20,21], which has been already applied in a thermoacoustic context, e.g. [22]. It is based on the fact that one can compute from time series the

drift and diffusion coefficients of a FP equation by using their statistical definition [20,21,23]:

$$F_A(A) \equiv \lim_{\tau \to 0} \frac{1}{\tau} \int (a - A)P(a, t + \tau | A, t)\, da \qquad (6)$$

$$F_\chi(\chi) \equiv \lim_{\tau \to 0} \frac{1}{\tau} \int (x - \chi)P(x, t + \tau | \chi, t)\, dx \qquad (7)$$

The noise intensity Γ is obtained with the second order moment for the time traces of A

$$\frac{\Gamma}{2\omega^2} \equiv \lim_{\tau \to 0} \frac{1}{\tau} \int (a - A)^2 P(a, t + \tau | A, t)\, da. \qquad (8)$$

In Eq. (6), the transition probability $P(a, t + \tau | A, t)$ is the probability of the amplitude a at a time $t + \tau$ knowing that the amplitude at the time t was A. These probabilities are extracted for $\tau \gtrsim 1/\Delta f$ with Δf the bandwidth of the filter applied on the microphones timetraces [24]. The limits for $\tau \to 0$ are obtained by extrapolation, as explained in [24]. The next step is to fit the theoretical model on the extracted drift and diffusion coefficients to identify the parameters Γ/ω^2, κ and $c_2\beta$. Although the noise intensity does not depend on the amplitude in the model, Fig. 5a shows that the extracted diffusion coefficient presents a parabolic shape. This is due to limitations in the extrapolation method for the extreme values of A. However, a validation on numerically generated data has shown that a reliable estimation of the noise intensity $\Gamma/2\omega^2$ can be obtained by weighting these extrapolated points with the experimental probability density function of A for the fit of $\Gamma/2\omega^2$. Once $\Gamma/2\omega^2$ is known, ν and κ are identified using the extracted drift function F_A (Fig 5b). With the knowledge of $\Gamma/2\omega^2$ and κ, $c_2\beta$ is identified using F_χ (Fig. 5c). As a final remark, it is important to note that modeling the nonlinear saturation with a cubic term only is too simplistic for the considered operating conditions, which are far away from the bifurcation point [25]. Consequently, although the identified values for ν, c_2 and κ allows to capture the topology of the phase space, they shall only be considered as indicative values.

5. Potential description

The equation for χ is now written in a potential form:

$$\dot{\chi} = -\frac{dU}{d\chi} + \frac{1}{A_0}\zeta_\chi, \qquad (9)$$

where the potential U is defined as:

$$U(\chi) = \frac{3\kappa}{256}A_0^2 \cos(4\chi) - \frac{c_2\beta}{8}\cos(2\chi)$$
$$- \frac{\Gamma \log(\cos(2\chi))}{4\omega^2 A_0^2}. \qquad (10)$$

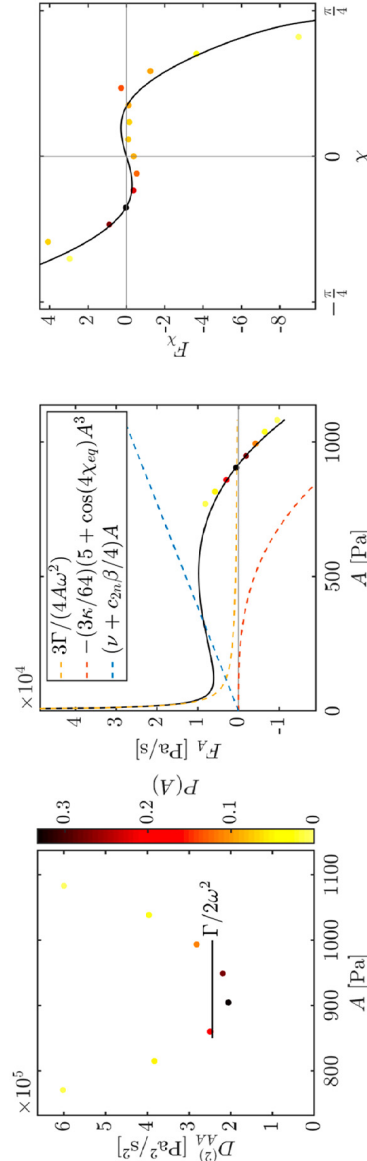Eq. (9) is formally similar to the equation of a particle of negligible mass evolving in a potential

Fig. 5. Fitting of $\Gamma/2\omega^2$, F_A and F_χ on the experimental data for the case $\Phi = 0.55$. The obtained values are: $A_0 = 904$ [Pa], $\nu = 19.5$ [s^{-1}], $\kappa = 1.27.10^{-4}$ [Pa^{-2}.s^{-1}], $\Gamma/\omega^2 = 4.89.10^5$ [Pa^{2}s^{-1}], $c_2\beta = 31.9$ [s^{-1}].
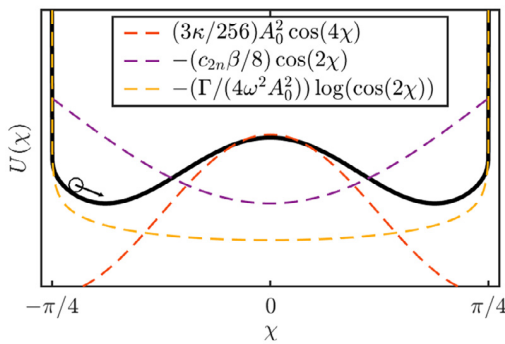
Fig. 6. Contributions to the potential.

landscape and undergoing a stochastic force ζ_χ/A_0 and a strong fluid friction [14]. It has to be noted that in Eq. (9), the noise intensity Γ affects not only the amplitude of the stochastic noise ζ_χ, but also the shape of the potential landscape U. The expression (10) of the potential has three terms: the first term, proportional to $A_0^2\cos(4\chi)$, grows with the limit cycle amplitude A_0 and promotes spinning modes. The second term, proportional to $c_2\beta\cos(2\chi)$, grows with the asymmetry coefficient c_2 and promotes standing modes. The third term increases with the ratio Γ/A_0^2, which depends on the relative importance of the noise compared to the limit cycle amplitude, it also promotes standing modes and creates potential barriers in $\pm\pi/4$, preventing the occurence of pure spinning modes. These terms and their contribution to the potential shape are represented on Fig. 6. Depending on the relative importance of these three terms, two situations can be encountered: the one-well potential leading to a dynamic centered around standing modes, and the two-well potential leading to a dynamic centered around two mixed modes spinning in opposite directions. The first situation occurs when $(3\kappa/16)A_0^2 \le c_2\beta/2 + \Gamma^2/(\omega^2 A_0^2)$. Then, the contribution of the asymmetry and the deterministic contribution of the turbulent noise in U predominate over the term coming from the nonlinear saturation, and F_χ has only one stable equilibrium point in $\chi = 0$, corresponding to a one-well potential around the standing mode, corresponding to the blue line in Fig. 7b. The noise excitation will make χ wander randomly around its equilibrium point, but the dynamics will be centered around a standing mode. The second situation occurs when $(3\kappa/16)A_0^2 > c_2\beta/2 + \Gamma^2/(\omega^2 A_0^2)$. Then, the term coming from the nonlinear saturation in $F_\chi(\chi)$ predominates over the terms coming from the asymmetry and the deterministic contribution of the turbulent noise, and F_χ has two symmetric stable equilibrium point $\pm\chi_{eq}$ corresponding to symmetric mixed modes propagating in opposite directions, and one unstable equilibrium point in $\chi = 0$. This corresponds to a potential landscape featuring two wells in $\pm\chi_{eq}$ separated by a poten-
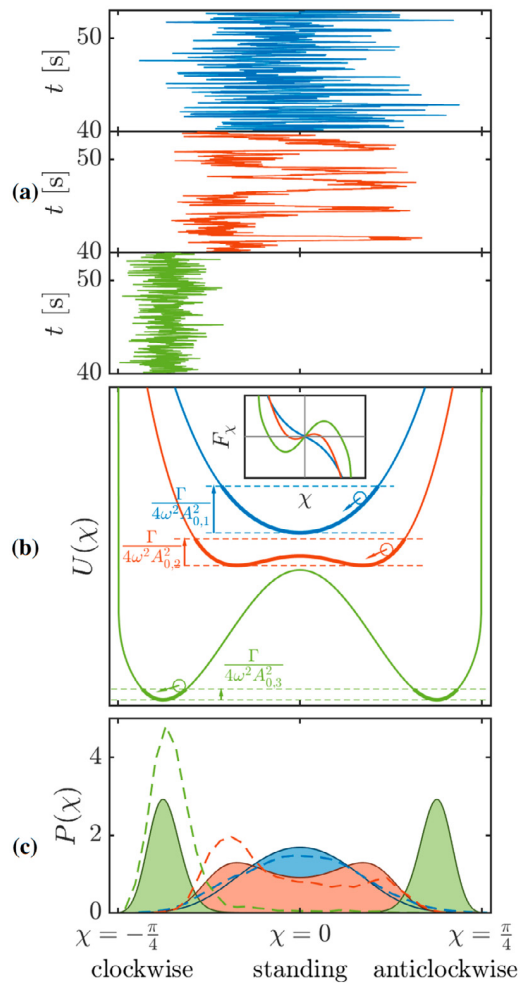

Fig. 7. Comparison of the potentials and PDFs of the 3 cases. Φ=0.525 (blue), standing mode. Φ=0.55 (red), switching mixed mode. Φ=0.60 (green), clockwise spinning mixed mode. **(a)**: Experimental timetraces of χ. **(b)**: potential $U(\chi)$ whose parameters are calibrated from the experimental data. The dashed lines show the typical range of χ which is explored by the system under a stochastic excitation of intensity $\Gamma/(4\omega^2 A_0)$. Inset: Drift coefficient for each case. **(c)**: Solid lines: PDF computed from the stationary Fokker-Planck equation. Dashed lines: PDF of the experimental timetraces.

tial barrier in $\chi = 0$. Fig. 7b shows examples of potentials presenting this two-well shape (red and green lines). The noise excitation will make χ wander randomly around one of the mixed modes and eventually trigger random jumps from one well to the other, making the propagating direction of the wave switch randomly.

For the cases showing two potential wells, the rate of jumps from one well to the other depends on the noise intensity. When χ is in one of the wells, Kramers theory will allow us to compute the prob-
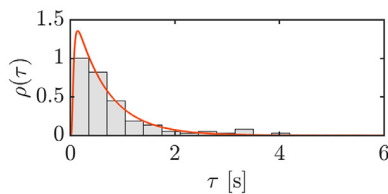
Fig. 8. PDF of escape time for $\Phi = 0.55$. Bars: experimental statistics. Red line: PDF obtained from the numerical resolution of the Fokker-Planck equation.

ability that χ crosses the barrier after a certain time [14]. The probability density function of χ is governed by the Fokker-Planck equation

$$\frac{\partial P(\chi, t)}{\partial t} = -\frac{\partial F_\chi P}{\partial \chi} + \frac{\Gamma}{4A_0^2 \omega^2} \frac{\partial^2 P}{\partial \chi^2} \qquad (11)$$

which is equivalent to the Langevin Eq. (9). We assume that χ is initially in one of the wells, e.g the positive one, $\chi = \chi_{eq}$. This is modelled with an initial condition $P(\chi, 0) = \delta(\chi - \chi_{eq})$ for the probability density. An absorbing boundary condition is placed in $\chi = 0$. We then consider $\mathcal{P}_c(t) = 1 - \mathcal{P}(\chi > 0, t)$, which is the probability that χ crossed the barrier in 0 at a time $\tau \leq t$. $\mathcal{P}_c$ is initially 0 and increases with t because of the absorbing condition. $\mathcal{P}_c(t) = \int_0^t \rho(\tau) d\tau$ with ρ the probability density function of the first passage time though the barrier. When the potential and the noise intensity are known, the Fokker-Planck equation can be solved numerically, giving access to ρ by differentiation of the cumulative distribution function $\mathcal{P}_c$.

6. Discussion

Fig. 7 summarizes how the shape of the potential landscape explains the differences in the dynamics of the nature angle between the three considered cases. Fig. 7b shows the potential landscapes associated with the calibrated model, whose parameters where identified from experimental data for each of the three cases, as explained in the previous section. The $\Phi = 0.525$ case (blue line) shows a single potential well in $\chi = 0$, so that the stochastic forcing leads to a predominantly standing mode. The $\Phi = 0.55$ (red line) and $\Phi = 0.60$ cases (green line) both present two symmetric potential wells separated by a potential barrier in $\chi = 0$. For the $\Phi = 0.55$ case (red), the noise intensity and the height of the potential barrier are of the same order of magnitude. The turbulent noise is therefore strong enough to drive χ from one well to the other, causing the observed phenomenon of intermittent transitions between clockwise and counterclockwise mixed modes. Conversely, the $\Phi = 0.60$ case (green) presents a slightly smaller level of noise, due to the stronger amplitude, and a higher

potential barrier. The noise level is small compared to the height of the potential barrier, making any switching event very unlikely: χ will remain confined in one well, corresponding to a constant spinning direction. The choice of the well depends only on the initial conditions. Fig. 7c compares the theoretical stationary PDFs against the experimental ones. It has to be noted that for the $\Phi = 0.60$ case (green), the solution of the stationary Fokker-Planck equation gives a bimodal distribution while the experiments show a single peak. This is because the solution of the stationary Fokker-Planck equation gives the repartition obtained for an infinite time. The duration of the experiment is too short to observe any switching event. For $\Phi = 0.55$, the probability density function of switching time ρ has been obtained numerically and compared to experimental statistics, showing good agreement (Fig. 8).

7. Conclusion

A low order model was used to describe the dynamics of the first azimuthal mode in an idealized annular combustion chamber subject to turbulent combustion noise. Considering a wave equation with coherent and stochastic source terms, we obtain an equation describing the modal dynamics as a stochastic diffusion process in a potential landscape. This equation gives a model for the spontaneous symmetry breaking that is observed on a real combustor, and which leads to either a clockwise spinning or a counter-clockwise spinning mode for sufficiently large values of the bifurcation parameter. The decomposition of the model's potential landscape allows us 1) to attribute the predominance of a spinning to the nonlinear saturation of the flame, while turbulent forcing and spatial asymmetries favor predominance of standing modes, and 2) to explain the intermittent transitions induced by the turbulent forcing when the potential barrier separating the two counter-spinning attractors has a height that is similar to the normalized stochastic forcing intensity. The model was able to reproduce quantitatively the statistics of these intermittent transitions, showing that it is a suited minimal model for describing the complex topology of the phase space.

Declaration of Competing Interest

None.

References

[1] T. Poinsot, *Proc. Combus. Inst.* 36 (1) (2017) 1–28.

[2] W. Krebs, P. Flohr, B. Prade, S. Hoffmann, *Combust. Sci. Technol.* 174 (7) (2002) 99–128.

[3] N. Noiray, B. Schuermans, *Proc. R. Soc. A* 469 (2151) (2013) 20120535.

[4] N.A. Worth, J.R. Dawson, *Proc. Combust. Inst.* 34 (2) (2013) 3127–3134.

[5] J.-F. Bourgouin, D. Durox, J.P. Moeck, T. Schuller, S. Candel, *Proc. Combust. Inst.* 35 (3) (2015) 3237–3244.

[6] N.A. Worth, J.R. Dawson, *Proc. Combust. Inst.* 36 (3) (2017) 3743–3751.

[7] P. Wolf, G. Staffelbach, L.Y.M. Gicquel, J.D. Müller, T. Poinsot, *Combust. Flame* 159 (11) (2012) 3398–3413.

[8] N. Noiray, M.R. Bothien, B. Schuermans, *Combust. Theory Model.* 15 (5) (2011) 585–606.

[9] G. Ghirardo, M.P. Juniper, *Proc. R. Soc. A* 469 (2157) (2013) 20130232.

[10] J.R. Dawson, N.A. Worth, *Proc. Combust. Inst.* 35 (3) (2015) 3283–3290.

[11] M. Bauerheim, M. Cazalens, T. Poinsot, *Proc. Combust. Inst.* 35 (3) (2015) 3219–3227.

[12] K. Prieur, D. Durox, T. Schuller, S. Candel, *Combust. Flame* 175 (2017) 283–291.

[13] T. Hummel, K. Hammer, P. Romero, B. Schuermans, T. Sattelmayer, *J. Eng. Gas Turbines Power* 139 (7) (2017) 071503.

[14] P. Hänggi, P. Talkner, M. Borkovec, *Rev. Mod. Phys.* 62 (2) (1990) 251–341.

[15] M. Mazur, H.T. Nygård, J.R. Dawson, N.A. Worth, *Proc. Combust. Inst.* 37 (4) (2019) 5129–5136.

[16] G. Ghirardo, M.R. Bothien, *Phys. Rev. Fluids* 3 (11) (2018) 113202.

[17] J. Flamant, N. Le Bihan, P. Chainais, *Appl. Comput. Harmon. Anal.* 46 (2) (2017) 351–383.

[18] N. Noiray, A. Denisov, *Proc. Combust. Inst.* 36 (3) (2017) 3843–3850.

[19] A. Faure-Beaulieu, N. Noiray, *Phys. Rev. Fluids* 5 (2) (2020) 023201.

[20] S. Siegert, R. Friedrich, J. Peinke, *Phys. Lett. A* 243 (5–6) (1998) 275–280.

[21] R. Friedrich, J. Peinke, M. Sahimi, M.R.R. Tabar, *Phys. Rep.* 506 (5) (2011) 87–162.

[22] N. Noiray, B. Schuermans, *Int. J. Non-linear Mech.* 50 (2013) 152–163.

[23] A.N. Kolmogorov, *Math. Ann.* 104 (1931) 415–458.

[24] E. Boujo, N. Noiray, *Proc. R. Soc. A* 473 (2200) (2017) 20160894.

[25] N. Noiray, *J. Eng. Gas Turbines Power* 139 (4) (2017) 041503.

Article III

Self-excited longitudinal and azimuthal modes in a pressurized annular combustor

Marek Mazur, Yi Hao Kwah, Thomas Indlekofer, James R. Dawson and
Nicholas A. Worth

Self-excited longitudinal and azimuthal modes in a pressurised annular combustor

Marek Mazur [a],[*], Yi Hao Kwah [b], Thomas Indlekofer [b],
James R. Dawson [b], Nicholas A. Worth [b]

[a] *CORIA-UMR 6614 Normandie Université, CNRS-Université et INSA de Rouen, Campus Universitaire du Madrillet, Saint Etienne du Rouvray, France*
[b] *Department of Energy and Process Engineering, Norwegian University of Science and Technology, Kolbjørn Hejes v 1B, 7491 Trondheim, Norway*

Abstract

A new laboratory scale pressurised annular combustion experiment is introduced and used to generate self-excited longitudinal and azimuthal instabilities. The experiments are operated at mean pressures ranging from approximately 2 to 3 atmospheres in order to maintain a well defined acoustic boundary at exit. A range of operating conditions is studied parametrically, and it is observed that at high equivalence ratios, the flame stabilisation location propagates upstream, significantly altering the flame structure. The change in flame stabilisation location promotes a transition from a dominant longitudinal to a dominant azimuthal instability. Investigation of the azimuthal instabilities highlights a rich array of frequency content, with significant amplitude pressure and heat release responses observed for not only the fundamental ($n = 1$), but also higher harmonics ($n = 2, 3$). These higher harmonics are also shown to exhibit distinct characteristic modal dynamics, shown through probability density functions of the spin ratio. The flame dynamics for three distinct operating states, corresponding to longitudinal modes at two different stabilisation locations, and one corresponding to strong azimuthal modes are studied. These highlight the difference between longitudinal and azimuthal modes, and demonstrate the presence of significant higher harmonic content. The characterisation of both longitudinal and azimuthal modes in a pressurised laboratory scale annular combustor for the first time provides a unique opportunity for understanding the nature of such instabilities in practically relevant configurations.
© 2020 The Author(s). Published by Elsevier Inc. on behalf of The Combustion Institute.
This is an open access article under the CC BY license. (http://creativecommons.org/licenses/by/4.0/)

Keywords: Pressurised combustor; Combustion instability; Annular combustor; Azimuthal modes; Flame dynamics

1. Introduction

Thermoacoustic instabilities remain an important issue for the design and operation of aero

* Corresponding author.
  E-mail address: marek.mazur@coria.fr (M. Mazur).

engines and stationary gas turbines. Many engines utilise annular combustion chambers, which may experience self-excited azimuthal modes [1]. The ability to replicate azimuthal instabilities in both lab and industrial scale annular combustors has given way to a range of recent experimental [2–7], numerical [8,9], and theoretical studies [10–14], which have provided insight into their nature. These have shown that the dominant mode shapes and modal dynamics (referring to the time-varying spin ratio, orientation, and strength of a mode) are associated with parameters such as burner geometry, equivalence ratio, bulk velocity, the presence or absence of a mean azimuthal flow, as well as whether the fuel is gaseous or liquid.

In previous experimental studies, however, the boundary conditions were not always well defined. In particular the acoustic impedance at the exit of the annular combustion chamber, which is commonly open to atmosphere [3,4]. As described in [3], depending on the length ratio between the inner and outer chamber walls, the combustor exhibits longitudinal and/or azimuthal modes, highlighting the importance of the downstream acoustic boundary. A similar combustor height mismatch was also employed by Bourgouin et al. [4] to generate azimuthal modes, with strong acoustic activity in the plenum showing the importance of the upstream boundary conditions. These boundary conditions are not trivial to replicate numerically, so simpler, more practically relevant conditions are necessary.

One way to generate a well-defined downstream boundary condition is to choke the flow; a condition which implies the pressurisation of the combustor ($\gtrsim$200 kPa). Due to the additional complexity and cost of such configurations, most studies have been conducted on pressurised single flames. Such studies have shown that an increase in combustor pressure leads to more compact flames [15], the modified acoustic boundary conditions can exert a strong influence on the mode structure [16,17], and can generate extremely large pressure oscillations, resulting in phenomena such as acoustically induced flashback [18]. While studies have featured annular combustion chamber geometry under pressurised conditions [19], many of these are in practical devices with highly complex geometry and limited optical access. While pressurised measurements in a lab scale annular combustor have been reported previously [20], only forced rather than self-excited oscillations have been observed.

The aim of the current investigation is to investigate self-excited azimuthal modes which occur in a pressurised lab scale annular combustor, during flame flashback. Choking the flow replicates the important acoustic boundary conditions of practical devices, allowing the effect of the boundary condition on the instabilities to be better understood. Furthermore, well-defined acoustic boundaries will help future simulations to replicate such experimental results, significantly enhancing our understanding. The remainder of the paper introduces a new experimental setup which allows both self-excited longitudinal and azimuthal modes to be studied for the first time at elevated pressure in a laboratory scale burner. In the current setup, azimuthal modes are only excited after flame flashback, which in itself is a phenomenon of significant interest. Therefore, the occurrence and transitional behaviour of these modes is discussed and the overall system stability and flame dynamics are described. Finally some conclusions are drawn.

2. Experimental methods

2.1. Intermediate Pressure Annular (IPA) combustor

Experiments were carried out in a novel Intermediate Pressure Annular (IPA) model combustor, shown schematically in Fig. 1. The flow geometry largely replicates that of previously reported atmospheric annular setups [2,3], with the addition of a convergent nozzle to choke the flow at the exit.

A premixed ethylene-air mixture is passed through a cylindrical plenum containing steel wool and glass beads to improve flow uniformity. The flow divides around a hemispherical bluff body, and is passed through a 22 mm thick sintered metal plate (mean pore size 183 μm, porosity 0.12, and $\Delta p = 15$ kPa). The acoustic boundary between the sintered metal plate and injection tubes was determined experimentally, and is characterised in the supplementary material.

The flow is divided between 12 injector tubes of $D_{inj} = 19$ mm, resulting in a non-dimensional flame separation distance of $S/D_{inj} = 2.3$. Each injector tube contains a central rod ($d_r = 5$ mm), which expands linearly at an angle of 38° over a stream-wise distance of 10 mm, resulting in a final bluff body of diameter $D_{bb} = 13$ mm. A six vane axial swirler, with the same geometry as reported previously [3], was positioned 10 mm upstream of the dump plane.

At the combustor exit, a first area reduction takes place through a symmetric matched 5th order contraction of length $L_{CR,1} = 34$ mm, and contraction ratio $CR = 7$, followed by a second area reduction via a replaceable blockage plate, with a thickness of 3 mm, featuring 164 holes of 2 mm diameter, distributed equally around a circle matching the mean chamber diameter $D_n = 169.5$ mm. This configuration mimics the approximately annular contraction in practical devices, resulting in a total area contraction ratio of $CR_{total} = 44$.

Main air and fuel flow rates were controlled using Mass Flow Controller (MFC) devices. Two MFCs (0 - 106.3 g/s) were used for air, and one MFC (0 - 20.7 g/s) was used for fuel. Each MFC was accurate to 0.8% of the reading plus $\pm 0.2\%$ of the full scale. The mean reactant supply tem-
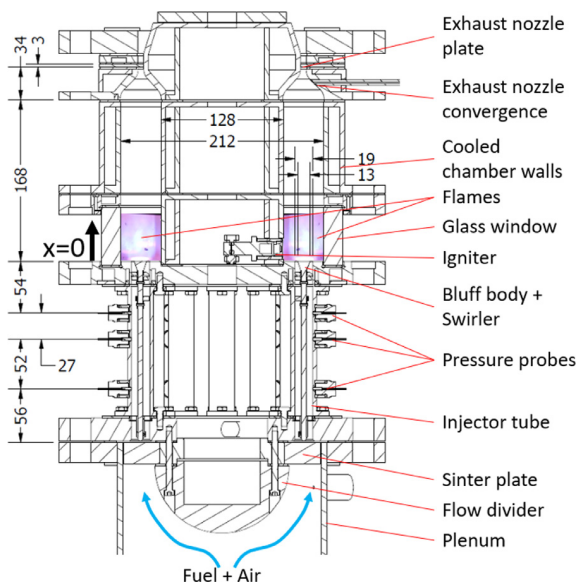
Fig. 1. Intermediate Pressurised Annular (IPA) combustor schematic with labels describing the main geometry and dimensions.

perature was around 293 K. A small independently operated pilot flame mounted on the inner annular wall was used to ignite the experiment. A range of equivalence ratios, $\phi = 0.65 - 0.95$, and air mass flow rates, $\dot{m}_a = 95.7 - 116.9$ g/s, was investigated.

Optical access was obtained through the outer annular wall as shown in Fig. 1. Three separate water paths were used to cool all other combustor surfaces, with isolated circuits for: 1. the dump plane; 2. the inner annular walls and inner nozzle walls; and 3. the outer annular walls and outer nozzle walls. A constant wall cooling flow rate was maintained in the three paths, which led to a combined cooling rate up to 80 kW.

2.2. Experimental measurements

Pressure fluctuations were measured in the injector tubes at three locations $x = -54, -81, -133$ mm upstream of the dump plane, at three angular locations around the annulus, $\theta_{k=\{1,2,3\}} = \{0°, 120°, 240°\}$. Pressure signals (from Kulite XCE-093 sensors, 1.4286×10^{-4} mV/Pa) were amplified (Fylde FE-579-TA) and sampled at $f_s = 51.2$ kHz during ~ 60 s for each experiment. The data presented in §3 corresponds to ~ 10 s for each run. Signals were digitised using a 24-bit DAQ system (NI model 9174). Each operating condition was tested 5 times, resulting in 175 experiments. Further to this, the transient case studied in Section 3.2 was tested 15 times to assess repeatability.

During experiments both longitudinal and azimuthal modes were observed, with the latter found to contain significant harmonics. To separate har-

monic components, frequency-domain filtering is performed selectively using an Infinite Impulse Response (IIR) filter, with width $\Delta f_{filt} = 0.2$ kHz and $\Delta f_{filt} = 1$ kHz for longitudinal and azimuthal modes respectively.

Longitudinal pressure oscillation amplitudes are evaluated at the fundamental frequency, f_L, averaged over the three angular locations, and described through the term $P'_L = |p(f_L)'|$. Components of the azimuthal mode of order $n = 1 - 3$ are evaluated at frequencies $f_{A,n=\{1,2,3\}}$, with these herein referred to as the fundamental, and first and second harmonic components. The modal dynamics of the filtered azimuthal components are evaluated using the approach described previously [5,8], applied now to components of order n. Estimates are made for $A_+(n)$ and $A_-(n)$, which are the amplitudes of azimuthal waves travelling in the anti-clockwise (ACW) and clockwise (CW) directions respectively, and the spin ratio $SR(n)$ [4]. The pressure response of azimuthal mode components of order n is thus evaluated as $P'_A(n) = |A_+^2(n) + A_-^2(n)|^{1/2}$. All pressure fluctuation amplitudes are described at a reference location $x = -54$ mm. Moreover, the multi-microphone method was used to locally characterise the magnitude of acoustic velocity oscillations ($|u(t)'|$) at the dump plane ($x = 0$ mm).

The dynamics of a single flame were analysed by synchronised high speed OH* chemiluminescence imaging. A high-speed camera (Phantom V2012) with intensifier (LaVision IRO) and UV filter (centre wavelength of 310 nm and a full width at half maximum of 10 nm) was used to capture the dy-
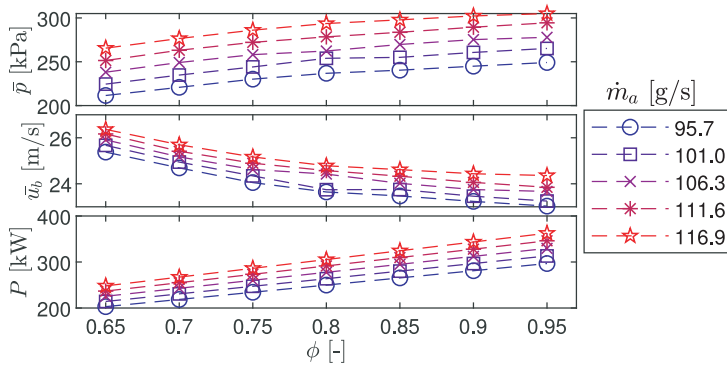
Fig. 2. Mean pressure, bulk velocity, and thermal power as functions of $\dot{m}_a$, and ϕ.

namics at angular location, $\theta = 30°$. 110,000 images were acquired at 10 kHz at an image resolution of 640×528 pixels, and spatial resolution of 0.11 mm/pixel. Imaging results are presented as phase averaged intensity distributions.

3. Results and discussion

3.1. Variation of mean operating conditions

Varying $\dot{m}_a$ and ϕ for a fixed exit area results in variations of the mean pressure $\bar{p}$, defined in the injection tubes, the bulk flow velocity u_b, defined at the dump plane ($x = 0$mm), and the thermal power. As shown in Fig. 2, the pressure varies from 210 to 305 kPa, increasing with both $\dot{m}_a$ and ϕ, due to the stagnation temperature rise and choked exit boundary conditions at all operating points. While bulk inlet velocity u_b increases with $\dot{m}_a$, it slightly decreases with ϕ due to the associated pressure increase. However, the variation in bulk flow velocity is relatively narrow ($\sim 10\%$), ranging from $u_b = 23.5 - 26.2$m/s. Power increases with $\dot{m}_a$ and ϕ, and ranges from $\sim 200 - 360$ kW.

3.2. Longitudinal to azimuthal instability transition

During the experiments a variety of self-excited instabilities were observed including both longitudinal and azimuthal modes, strongly depending on operating condition. At low equivalence ratios only longitudinal modes were observed. However, at high equivalence ratios a more complicated transitional behaviour occurred, during which mode switching between longitudinal and azimuthal states was observed, accompanied by a dramatic change in flame shape due to flashback.

Fig. 3 shows mode transition for the $\phi = 0.95$, $\dot{m}_a = 116.9$g/s case through a number of metrics. The pressure time series from a single sensor at location $\theta_{k=1}$ was used to calculate the spectrogram (Hamming windows of length 98 ms, and overlap 60 %). The acoustic velocity oscillation magnitude is presented with the pressure time series, which shows the envelope of the pressure response. A time series of spin ratio is also plotted for azimuthal mode components of order $n = 1, 2$, and the flame structure is described through photographs taken with an SLR camera at selected times.

From the spectrogram, a strong longitudinal mode can be initially observed to dominate at a frequency of ~ 410 Hz. The image at time t_1 corresponds to this excitation, and a swirling bluff-body stabilised flame structure can be observed at each injector location. The flame structure is noticeably diffuse, which is due to the strong oscillations (described further in Section 3.4).

The flames are observed to flashback between time t_1 and t_2, stabilising upstream of the bluff body. Later inspection identified that the flames flash back a distance of 10mm, before anchoring on the downstream edge of the swirl vanes in each injector tube. The image at time t_2 shows the flame structure initially after flashback occurred, with a more compact structure and narrower distribution in the transverse direction. The image shown in Fig. 3 was chosen to illustrate that on occasion, not all flames flashback, which is likely due to slight imperfections in the flow uniformity from flame to flame.

Flashback occurred in response to an increase in equivalence ratio. However, over multiple repeat measurements, the time until flashback varied by up to 10 seconds, after the new operating condition had been reached. It is our conjecture that this relatively long and variable delay may be associated with thermal inertia. After ϕ is increased, the dump plane and bluff body temperatures will also increase over several seconds due to the higher thermal power, permitting flashback through the low velocity flow in the boundary layer. As shown in Fig. 2, increasing ϕ reduces the bulk flow velocity, while increasing flame speed, and although flame speed has a weak inverse scaling with pressure [21], the higher ratio of flame speed to bulk flow veloc-
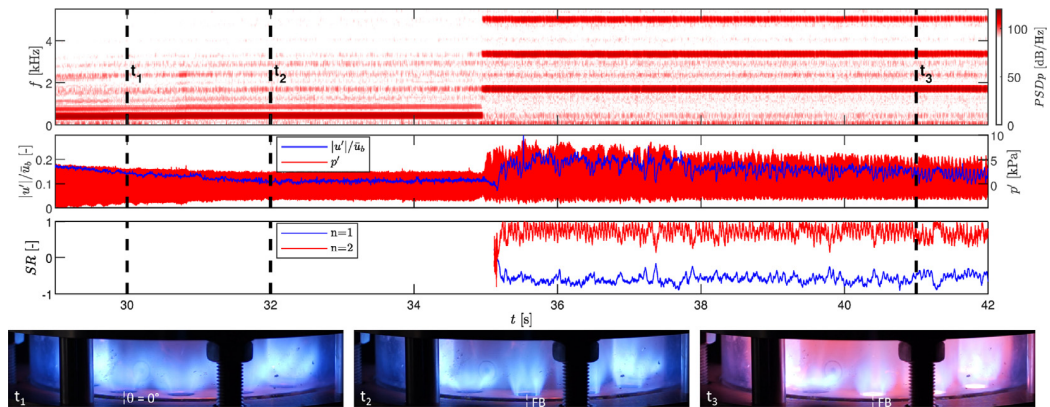
Fig. 3. Transitional behaviour of instability, switching from longitudinal to azimuthal modes for the $\phi = 0.95$, $\dot{m}_a = 116.9$ g/s case. Spectrogram (*top row*), and pressure and normalised bulk velocity oscillations (*second row*) both from $\theta_{k=1}$ location. Spin ratio time series for azimuthal modes (*second row*). Images (*bottom row*) show mean flame structure at: t_1, during longitudinal mode; t_2, flashback induced change to flame structure during longitudinal mode; t_3, after transition to azimuthal mode. FB: Flashbacked flame

ity at higher equivalence ratios ($\phi \geq 0.85$) enables flashback.

The frequency remains relatively constant prior to flashback, while the pressure oscillation amplitude decreases only slightly, but is still significant. The pressure oscillations result in significant ($|u'|/\bar{u}_b \approx 0.15$ for the $n = 1$ component) longitudinal velocity oscillations, as shown in Fig. 3. Thus, given the significant periodic oscillations in the bulk flow velocity, the flashback observed is also likely to depend on the presence of combustion instabilities in the system.

After flashback, modal transition from longitudinal to azimuthal takes place as shown in the spectrogram in Fig. 3, with the fundamental azimuthal mode component at a frequency of $f_{A,n=1} \approx 1.65$ kHz accompanied by significant amplitude higher harmonics. Following flashback, the bluff bodies undergo significant heating, as shown in the image at t_3. The notable delay of up to 5 seconds between the sudden change in flame structure following flashback, and the mode transition from longitudinal to azimuthal, we again conjecture is a result of thermal inertia.

In the example presented in Fig. 3 not all flames exhibit flashback, creating an asymmetric distribution. However, this transitional case was tested 15 times, and on a number of occasions all flames flashback. It was observed that this does not change the transition behaviour, with qualitatively similar flashback and then mode switching from longitudinal to azimuthal being observed during each repeat test. Furthermore, the nature of the azimuthal modes after switching is also qualitatively similar. Therefore, the transient phenomena described herein can be regarded as highly repeatable.

To confirm the nature of the modes observed in Fig. 3, the power spectral density was calculated separately for regions in the time series corresponding purely to longitudinal and azimuthal modes, as shown in Fig. 4, which includes local representative pressure time series to show the time dependent behaviour.

During longitudinal oscillations, time varying pressure oscillations at locations around the annulus are of similar amplitude and approximately in-phase. The pressure oscillations deviate slightly from sinusoidal behaviour due to the presence of higher harmonics, which can be clearly observed in the PSD and in the filtered time series. It is also interesting to note the presence of frequency content corresponding to the first azimuthal mode component and corresponding higher harmonics even when the longitudinal mode dominates.

In contrast, following modal transition the PSD shows only significant peaks for azimuthal mode components. The pressure time series during azimuthal instability now shows large departures from sinusoidal behaviour due to significant amplitude harmonics, which are clearly observed in the filtered time series. The filtered time series for the fundamental $n = 1$ component exhibits pressure oscillations of similar magnitude, with a phase lag corresponding to the angular separation of the sensors, indicative here of a strong CW spinning mode. Given the dominant amplitude of this fundamental component, similar features can be identified in the unfiltered pressure times series. However, the behaviour of the $n = 2$ component is distinctly different, exhibiting spinning behaviour in the ACW direction, at this instant in time. The modal dynamics are also presented later in Fig. 6, which shows that for this case, the fundamental and first harmonic spin in opposing directions. Given the current arrangement of sensors it is not pos-
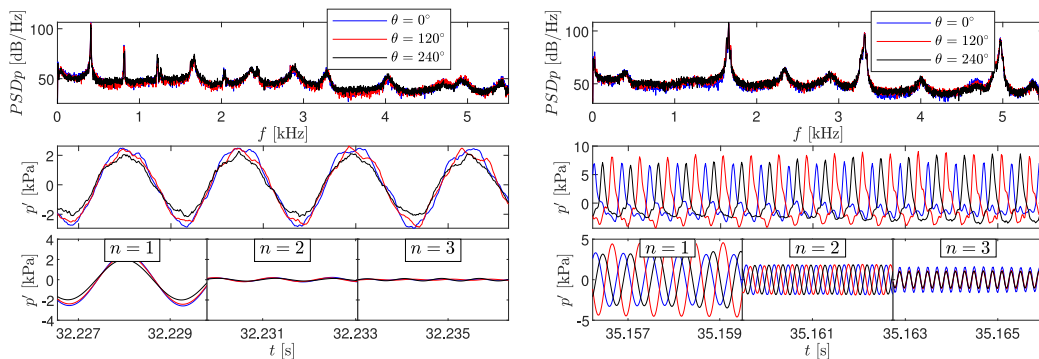
Fig. 4. Pressure PSD (*top row*) and local pressure time series during predominantly longitudinal (*LHS*) and azimuthal (*RHS*) modes for the $\phi = 0.95$, $\dot{m}_a = 116.9$g/s case, at a location $x = -54$ mm. Both unfiltered (*middle row*) and filtered (*bottom row*) pressure time series are shown.
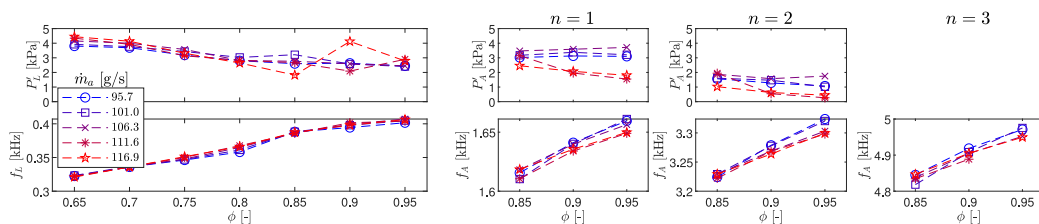

Fig. 5. Amplitude (*top row*) and frequency (*bottom row*) response of longitudinal (*LHS*) and azimuthal (*3 RHS columns*) mode components as a function of ϕ and $\dot{m}_a$, evaluated at $x = -54$ mm.
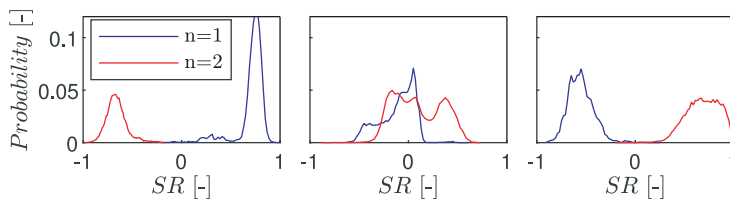
Fig. 6. *SR* probabilities for $n=1,2$. Left: $\phi = 0.85$, $\dot{m}_a = 111.6$ g/s. Middle: $\phi = 0.95$, $\dot{m}_a = 95.7$ g/s. Right: $\phi = 0.95$, $\dot{m}_a = 116.9$ g/s.

sible to determine the modal dynamics of the 2nd harmonic ($n = 3$).

3.3. Stability analysis and modal dynamics

Following the analysis of transition between longitudinal and azimuthal modes, the stability over the range of operating conditions is now described. Fig. 5 shows the frequency and amplitude response for both longitudinal and azimuthal instabilities as a function of ϕ and $\dot{m}_a$. The transitional flashback phenomena was only observed when $\phi \geq 0.85$, and azimuthal modes are thus plotted for a restricted range. The self-excitation frequency for all mode components is shown to increase with ϕ as expected, due to the increase in gas temperature and speed of sound within the combustion chamber. The lack of dependence on $\dot{m}_a$,

and therefore thermal power also suggest that minor differences in wall cooling rates do not significantly affect the chamber temperature.

While the pressure response shows a weak inverse scaling with ϕ, longitudinal modes show little dependence on $\dot{m}_a$. Therefore, given the strong dependence of pressure and power on $\dot{m}_a$ shown previously in Fig. 2, the absolute magnitude of longitudinal instability does not appear to scale with these. Azimuthal mode components in contrast show some dependence on $\dot{m}_a$, with lower amplitudes observed for the two highest $\dot{m}_a$ cases. The amplitudes are of a similar order of magnitude for both longitudinal and azimuthal modes and an order of magnitude larger in absolute terms (and several times larger when normalised by the mean pressure) in comparison with similar measurements made at atmospheric conditions [3].
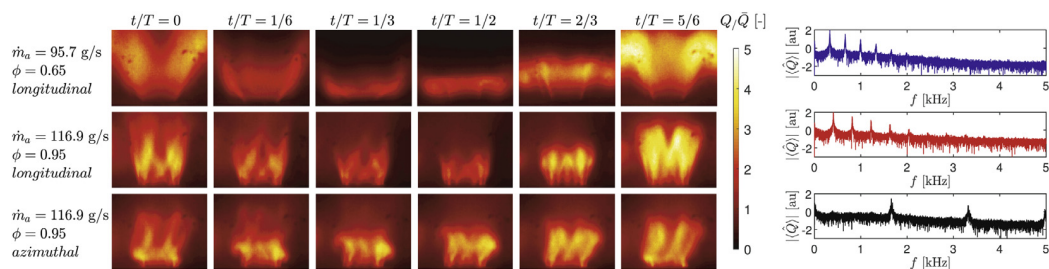
Fig. 7. Phase averaged OH* chemiluminescence imaging of a single flame at $\theta = 30°$ (*LHS*), and frequency spectra of the globally integrated fluctuating heat release rate (*RHS*), conditioned for 3 states: $\phi = 0.65$, $\dot{m}_a = 95.7$ g/s (*Top*); $\phi = 0.95$, $\dot{m}_a = 116.9$ g/s (*midlle*) longitudinal; $\phi = 0.95$, $\dot{m}_a = 116.9$ g/s azimuthal (*bottom*).

The azimuthal modal dynamics can be assessed through the distribution of spin ratios, as shown through PDF distributions for selected cases in Fig. 6. While significant variations were observed in SR as ϕ and $\dot{m}_a$ were varied, no clear trends could be identified. However, it is interesting to note that the modal dynamics of azimuthal mode components of order, $n = 1, 2$ both demonstrate distinct modal preferences. This can result in the preferential selection of separate states. For example, the modal distribution for the $\phi = 0.85$ $\dot{m}_a = 111.6$ g/s case shows the first two azimuthal mode components select distinct spinning modes. In contrast, the components in the $\phi = 0.95$ $\dot{m}_a = 95.7$ g/s case show a preference for predominantly standing behaviour. Corresponding peak locations in this case raise the possibility of coupling between the dynamics of these components (also suggested by the time varying spin ratios shown previously in Fig. 3), and a more detailed investigation of the modal dynamics between harmonic components is warranted in future work.

3.4. Flame dynamics

Fig. 7 shows the phase averaged flame dynamics (LHS), and integrated PSD (RHS) for the three flow states described in Section 3.2. The upper row of images illustrates the $\phi = 0.65$, $\dot{m}_a = 95.7$ g/s case. Flashback was not observed and the magnitude of the longitudinal instability is associated with extreme oscillations in flame length and heat release rate through the cycle. From the point of minimum heat release rate, where the flame is flattened against the dump plane, the flame brush rolls up in response to the longitudinal velocity fluctuation, resulting in maximum heat release rate at $t/T = 5/6$.

The lower two rows correspond to the $\phi = 0.95$, $\dot{m}_a = 116.9$ g/s case after flame flashback. During longitudinal instability (middle row), oscillations in both flame length and heat release rate stay similar. However, as noted in Fig. 3, flashback results in a dramatic modification of the flame structure, reducing the spreading angle, and altering the distribution of heat release. Angled streaks of high intensity heat release rate are likely to correspond to increasing patternation from the six vane swirler, resulting in a loss of symmetry.

In the bottom row, the reduced flame brush angle and increased patternation are still present, but the azimuthal self-excitation leads to different dynamics. The flame length oscillations are now accompanied by a strong asymmetric transverse flapping motion. The strong CW spinning mode ($\overline{SR} = -0.58$) results in pressure oscillations travelling from right to left, leading to stronger vortex roll up on the left hand side, and an inclined propagation downstream of the flame brush. Due to the higher frequency of oscillation, the variation in heat release rate magnitude is less pronounced through the cycle in comparison with the longitudinal modes.

Finally, given the strong presence of higher harmonic content shown previously in Section 3.2, the magnitude of the globally integrated fluctuating heat release rate $|\langle \widehat{Q} \rangle|$ is analysed in frequency spectra, where $\langle \ldots \rangle$ and $\widehat{\ldots}$ denote the ensemble average and frequency space fluctuations respectively. The amplitude of the spectra is represented on a logarithmic scale. As shown on the RHS of Fig. 7, significant peaks can be seen for both longitudinal and azimuthal mode components of order $n = 1 - 3$. While the relative magnitudes of the $n = 1$ and $n = 2$ azimuthal components modes is less pronounced in comparison with the pressure response presented in Section 3.2, the magnitude of the harmonic modes is still significant, confirming the importance of these in a description of the overall response.

4. Conclusions

A new pressurised laboratory scale annular combustor was introduced and used to characterise the occurrence and dynamics of self-excited instabilities. High equivalence ratios modified the flame stabilisation location and flame structure, pro-

moting transition from longitudinal to azimuthal modes.

The frequency and amplitude of both longitudinal and azimuthal modes were characterised across a range of mass flow rates and equivalence ratios, resulting in a variation of pressure, power and flow rate. A weak inverse scaling of amplitude with equivalence ratio was observed for the majority of modes. Additionally, significant amplitude higher order harmonics were observed for the azimuthal modes, and these were observed to contain distinct time varying modal dynamics.

Simultaneous high speed OH* chemiluminescence measurements were also used to characterise a range of flow states, demonstrating distinct dynamics corresponding to both longitudinal and azimuthal modes. Significant higher harmonic oscillations were also observed in the heat release rate oscillations, demonstrating the response of high amplitude self-excited azimuthal instabilities under pressurised conditions may contain additional complexity in comparison with modes generated at atmospheric conditions.

Declaration of Competing Interest

None.

Acknowledgements

Supplementary material

Supplementary material associated with this article can be found, in the online version, at doi:10.1016/j.proci.2020.05.033.

References

[1] W. Krebs, P. Flohr, B. Prade, S. Hoffmann, *Combust. Sc. Tech.* 174 (2002) 99–128.
[2] N.A. Worth, J.R. Dawson, *Proc. Combus. Inst.* 34 (2013) 3127–3134.
[3] N.A. Worth, J.R. Dawson, *Combustion and Flame* 160 (2012) 2476–2489.
[4] J.-F. Bourgouin, D. Durox, J.P. Moeck, T. Schuller, S. Candel, ASME Turbo Expo 2013V01BT04A007.
[5] N.A. Worth, J.R. Dawson, *Proc. Combus. Inst.* 36 (2017) 3743–3751.
[6] K. Prieur, D. Durox, T. Schuller, .S. Candel, *J. Eng. Gas Turbines Power* 140 (2017) 031503.
[7] M. Mazur, H.T. Nygård, J.R. Dawson, N.A. Worth, *Proc. Combus. Inst.* 37 (2019) 5129–5136.
[8] P. Wolf, G. Staffelbach, L.Y.M. Gicquel, J.-D. Müller, T. Poinsot, *Combustion and Flame* 159 (2012) 3398–3413.
[9] N. Zettervall, M. Mazur, J.R. Dawson, N.A. Worth, C. Fureby, *Proc. Combus. Inst.* 37 (4) (2019) 5223–5231.
[10] N. Noiray, B. Schuermans, *Proc. R. Soc. A Math. Phys. Eng. Sci.* 469 (2012).
[11] G. Ghirardo, M.P. Juniper, *Proc. R. Soc. A Math. Phys. Eng. Sci.* 469 (2013).
[12] B. Schuermans, V. Bellucci, C.O. Paschereit, *ASME Turbo Expo* (2003) 509–519.
[13] M.R. Bothien, N. Noiray, B. Schuermans, *J. Eng. Gas Turbines Power* 137 (2015) 061505.
[14] J.P. Moeck, D. Durox, T. Schuller, S. Candel, *Proc. Combus. Inst.* 37 (2019) 5343–5350.
[15] Z. Xi, Z. Fu, X. Hu, S.W. Sabir, Y. Jiang, *Energies* 11 (2018) 930–949.
[16] M. Cazalens, S. Roux, C. Sensiau, T. Poinsot, *J. Prop. Power* 24 (2008) 770–778.
[17] M. Mazur, W. Tao, P. Scouflaire, F. Richecoeur, S. Ducruix, *ASME Turbo Expo* (2015). V04BT04A001
[18] C. Lapeyre, M. Mazur, P. Scouflaire, F. Richecoeur, S. Ducruix, T. Poinsot, *Flow Turb. Combust.* 98 (2017) 265–282.
[19] M. Mastrovito, S.M. Camporeale, A. Forte, B. Fortunato, ASME Turbo Expo 2005749–756.
[20] D. Fanaca, P.R. Alamela, C. Hirsch, T. Sattelmayer, *J. Eng. Gas Turbines Power* 132 (2010) 071502.
[21] A.A. Konnov, *J. Proc. Europ. Combust. Meeting* (2015) 071502.

Article IV

The effect of hydrogen addition on the amplitude and harmonic response of azimuthal instabilities in a pressurized annular combustor

Thomas Indlekofer, Byeonguk Ahn, Yi Hao Kwah, Samuel Wiseman,
Marek Mazur, James R. Dawson and Nicholas A. Worth

The effect of hydrogen addition on the amplitude and harmonic response of azimuthal instabilities in a pressurized annular combustor

Thomas Indlekofer [a,*], Byeonguk Ahn [a], Yi Hao Kwah [a], Samuel Wiseman [a], Marek Mazur [b], James R. Dawson [a], Nicholas A. Worth [a]

[a] Department of Energy and Process Engineering, Norwegian University of Science and Technology, Trondheim N-7491, Norway
[b] CORIA-UMR 6641 Normandie Universit, CNRS-Universit et INSA de Rouen, Campus Universitaire du Madrillet, Saint Etienne du Rouvray, France

ARTICLE INFO

ABSTRACT

The present work introduces an annular combustion chamber operated at intermediate pressures. The combustor is operated with CH_4-H_2 blends leading to a variety of azimuthal combustion instabilities. The influence of the hydrogen content, the air mass flow rate and the equivalence ratio on the instabilities is investigated over a wide range of operating conditions with mean chamber pressures from 1.5 to 3.3 bar. This leads to a range of exit boundary conditions, from partially to fully reflecting. It is found that pure methane and methane-hydrogen mixtures with low hydrogen contents result in stable combustion. However, when the hydrogen content reaches 25% by volume high-amplitude instabilities are excited, which exhibit higher order harmonics with significant pressure amplitude contributions. Such harmonic response was not previously observed in atmospheric annular combustors. The amplitudes decrease slightly when the H_2 content is increased further. The harmonic response is found to be amplitude dependent with fewer significant harmonic contributions occurring at low-amplitudes and a cut-on amplitude of the fundamental mode at which higher harmonics become significant. The interaction between the harmonic components of the pressure amplitudes is shown to follow a quadratic relationship. The modal response was analyzed and it was found that all high-amplitude instabilities feature clockwise spinning modes whereas lower-amplitude instabilities feature counter clockwise spinning modes. Finally, a low- and high-amplitude case were investigated in detail and phase-averaged images are discussed. The low-amplitude instabilities result in flame dynamics similar to those observed in atmospheric combustors previously whereas the high-amplitude instabilities exhibit large oscillations in the flame height and intensity. A characterization of the boundary conditions is also provided for numerical simulations which includes temperature measurements, acoustic characterization and cold flow velocity profiles.

1. Introduction

The shift towards renewable energy sources, such as wind and solar power, is leading to an increasing share of intermittent energy sources in the future energy mix. Gas turbines are seen as a vital enabling technology for renewable energy sources as they are highly dispatchable, meaning they can be rapidly deployed to stabilize the grid [1].

A promising way to reduce carbon emissions is to increase the use of hydrogen as a fuel. While the introduction of hydrogen into the fuel (usually CH_4) can increase the flammability limit and power density, the high reactivity of hydrogen can also promote

flashback [2]. Even a modest addition of hydrogen leads to an increase in the laminar flame speed and a reduction of the flame height which can have a major impact on the thermoacoustic stability of a combustor [3,4].

Thermoacoustic instabilities result from a constructive coupling between the acoustic field and fluctuations in the heat release rate that lead to large pressure oscillations [5], thereby limiting the operational envelope and reducing the life time of the combustor. Despite decades of investigation, self-excited thermoacoustic instabilities still remain a serious problem and further understanding of the phenomenon in practically relevant configurations is needed [6,7].

Modern gas turbines and aeroengines often have annular combustion chambers. Azimuthal modes propagating in either direction around the annulus have been observed in industrial combustors [8–10], and have been reproduced in atmospheric

* Corresponding author.
E-mail address: thomas.indlekofer@ntnu.no (T. Indlekofer).

pressure laboratory combustors [11–13], as well as high-fidelity numerical simulations [14,15]. Azimuthal modes can take the form of standing modes, with a fixed nodal line position, spinning modes with the nodal line spinning around the annulus at the speed of sound, or a combination of both leading to mixed modes. These modes can undergo continuous transitions between either mode nature [11,12,14,16], a phenomenon commonly referred to as *modal dynamics* [9]. Over the last decade, the dynamic nature of these modes has received significant attention from the scientific community. Modal dynamics were shown to be dominated by the effects of symmetry breaking [11,17–20] and turbulent noise [9,21,22].

Even though several laboratory annular combustion chambers now exist [11,13,23], they usually feature an exit boundary condition open to atmosphere. This complicates the transferability to industrial engines (gas turbines for power generation operate at around 20 bar [24]) and the ability to conduct high fidelity numerical simulations due to complex boundary conditions [6,25]. Subsequently, there is a need for choked experimental rigs, enabling the study of combustion instabilities with more realistic acoustic boundary conditions at higher pressures, turbulence levels and power densities.

There has been a number of studies investigating the dynamics of swirl or bluff body stabilized flames at elevated pressure in single isolated flames. Freitag et al. [26] measured flame transfer functions (FTFs) from $1.1 − 5 \, bar$ to investigate the effect of pressure on the FTF. They found that pressure can introduce a phase shift, which has an influence on the stability of a combustor. In terms of the gain, the effect of pressure led to a higher response at higher frequencies and the opposite at low frequencies. This finding was supported by Cheung et al. [27]. Sabatino et al. [28] found that elevated pressure modifies the flame-vortex interactions causing an increase in the gain. It was also found that the effect of pressure on flame interaction was fuel-dependent. While the local maxima of the FTF increased monotonically for methane, for propane it increased until 3 bar and then dropped.

Under well controlled laboratory conditions there are only a few pressurized experiments in annular combustion chambers. Fanaca et al. [29,30] introduced a down-scaled model of an Alstom gas turbine, which was operated at elevated pressure but did not feature self-excited azimuthal instabilities under fully choked exit conditions. Under forced operation, they observed a difference between FTFs of the single sector and annular combustor which was attributed to differences in the resulting aerodynamics. Mazur et al. [31] reported self-excited longitudinal and azimuthal modes in a pressurized annular combustor. However, the occurrence of azimuthal modes was linked to a flashback phenomenon precluding long run times but strong harmonic contributions appeared which were not observed in previous atmospheric studies.

In addition to the effect of pressure on self-excited azimuthal modes, information on the thermal state and acoustic boundary conditions of the combustor is also needed for high-fidelity simulations. Progress depends on both simulations and experiments, and therefore, part of the aim of this research is to provide a test case that can replicate as many of the important boundary conditions found on a real engine as possible, whilst maintaining the well-controlled conditions of an optically accessible lab setup.

This work constitutes the first detailed study of azimuthal combustion instabilities at elevated pressures across a wide range of operating conditions in order to study the modal dynamics, the role of pressure scaling on the response, and to examine in more detail the behaviour of the harmonic contributions. In addition, a thorough characterization of the boundary conditions was performed.

The paper is organized as follows. First, the setup and the operating conditions are introduced. Then the general system response

in terms of the amplitudes and nature of the modes is investigated and analyzed for different hydrogen contents, air flow rate and equivalence ratio. We then focus our investigation on two particular cases, a high- and low-pressure amplitude case, by analyzing their pressure time-series and flame dynamics.

2. Experimental methods

2.1. Intermediate pressure annular (IPA) combustor

A schematic of the combustor is presented in Fig. 1. Premixed fuel-air mixtures are fed into a cylindrical plenum that conditions the flow (through a bed of glass beads in the expansion) before it passes through a 22 mm thick sintered metal plate and is divided between twelve burners. The twelve burners are comprised of tubes that hold the bluff bodies and counter clockwise swirlers (as viewed from above) which are equally spaced around the circumference of the annular combustor. The lower section of the outer wall consists of a quartz glass window enabling optical access for high-speed imaging. The combustion chamber has a length of 168 mm and an inner/outer diameter of $d_i = 128 \, mm$ and $d_o = 212 \, mm$ respectively. The outer and inner walls, as well as the dump plane are cooled by separate water circuits. The chamber ends with a symmetric contraction (contraction ratio $CR_c = 7$) before the flow is passed through a choking plate ($CR_p = 5$), which further reduces the outer diameter, leading to $CR_{total} = 35$. A second choking plate can be mounted upstream of the plenum expansion.

Further details and a limited set of data with the upper choking plate are presented in A.1 for comparison, an acoustic characterization of the glass bead section, the sintered metal plate and the swirler is found in A.2 and the supplemental material. Details about the pressure drop across the sintered metal plate are presented in A.3 and information about the cooling heat transfer in Appendix D. The complete 3D CAD model is available in the supplemental material.

2.2. Experimental measurements

Dynamic pressure measurements (Kulite XCE-093 sensors, $1.43 \times 10^{-4} \, mVPa^{-1}$) were recorded at five azimuthal positions ($\Theta_{0-4} = 0, 30, 60, 120$ and $240°$) and two longitudinal positions in the injector tube at $z_1 = −81 \, mm$ (upper microphone) and $z_2 = −133 \, mm$. The signals were acquired at a sampling frequency $f_s = 51.2 \, kHz$ and digitized using a 24-bit DAQ system (NI model 9174). Additionally two Danfoss MBS 3000 pressure sensors monitor the mean pressure in the combustion chamber and the plenum.

A high-speed camera (Phantom V2012) with intensifier and UV filter ($\lambda = 310 \, nm$, FWHM 10 nm) and a photo multiplier tube (PMT) with the same UV filter are used to capture OH*-chemiluminescence at $\Theta = 30°$.

To determine the temperature of the bluff body, dump plane and inner wall at certain locations, a pyrometer (Optris CT Laser 3MH) was used. An explanation of the procedure and temperatures for two operating conditions are provided in Appendix C.

2.3. Operating conditions and experimental procedure

The operating conditions are described in Table 1. Air mass flow rates ranged from 61.25 to 122.5 gs^{-1} and the fuel was composed of methane (CH_4) with varying quantities of hydrogen (H_2). Air and fuel are combined in a mixing chamber upstream of the plenum. A range of volume fractions $P_V = \dot{V}_{H2}/(\dot{V}_{CH4} + \dot{V}_{H2})$ of $0 − 0.5$, where 0 is no hydrogen and 1 is pure hydrogen, were investigated. This ratio can be translated to the power fraction P_H, resulting in a
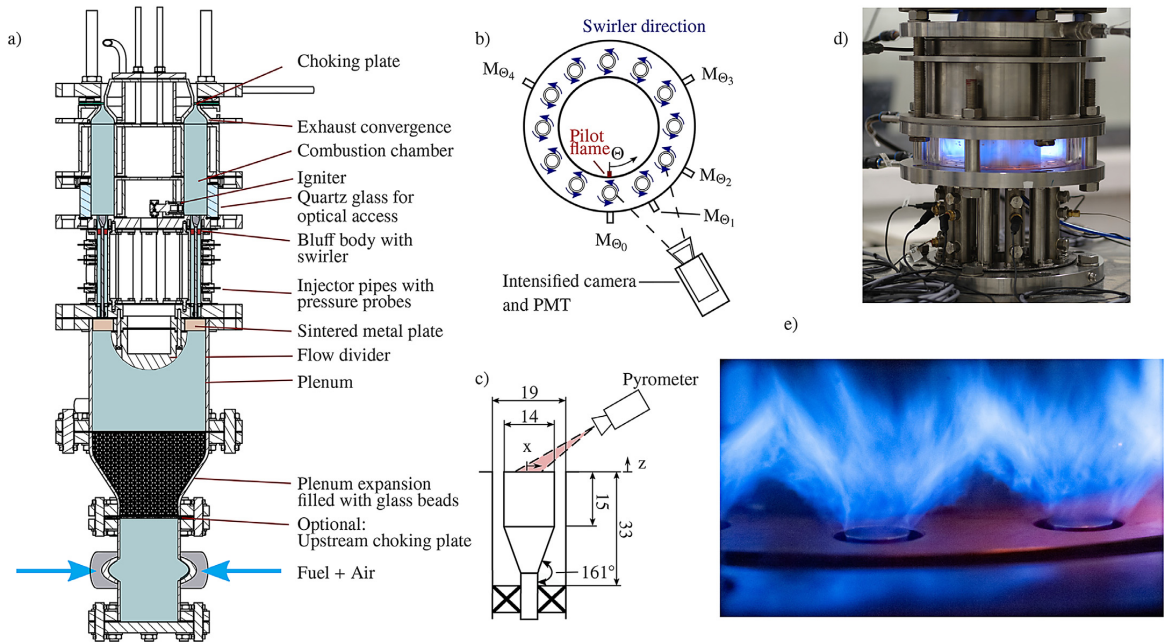
Fig. 1. (a) Schematic of the Intermediate Pressure Annular (IPA) combustor with (b) top view showing the azimuthal position of microphones and the high-speed camera to acquire OH*-chemiluminescence, (c) detailed view of the modified bluff body/swirler assembly (d) Photograph of the IPA combustor during operation and e) quasi-instantaneous image of the flame dynamics.

Table 1
Operating conditions in terms of the air mass flow rate $\dot{m}_a$, the hydrogen power fraction P_H, the hydrogen volume fraction P_V, the equivalence ratio Φ, the laminar flame speed at $p = 2\ bar$ and the resulting thermal power P and exit bulk velocities u_b.

	Stable		Presented data set		Flashback
$\dot{m}_a$ [g/s^{-1}]			61.25–122.5		
P_H	0-0.05	0.1	0.15	0.2	0.25
P_V	0-0.14	0.25	0.35	0.43	0.5
Φ			0.65-1.0		
s_L [m/s^{-1}]		0.17-0.35	0.19-0.39	0.2-0.43	
P [kW]			170-350		
u_b [m/s^{-1}]			28-22		

range of $0 - 0.25$, which was investigated in steps of 0.05. Although stability maps were performed for P_H=0 and 0.05, none of the investigated cases featured self-excited instabilities. For $P_H = 0.25$ it was found that the combustor was prone to flashback. Subsequently, this work will focus on $P_H = 0.1 - 0.2$ with an equivalence ratio (Φ) range of $0.65 - 1$ with steps of 0.05.

Ignition and light-around was performed at $\dot{m}_a = 40.83\ gs^{-1}$, $\Phi = 0.7$ and initiated by a rich ethylene pilot flame at $\Theta = 0°$. This differs from the usual method of ignition in laboratory annular combustion chambers, which typically use one or multiple spark ignitors [32,33]. In the present procedure a combustible mixture is introduced into the combustion chamber only after the pilot flame has been successfully ignited. As soon as a combustible fuel-air mixture reaches the chamber, the pilot ignites a flame kernel which is advected downstream towards the choking plate where it ignites a larger portion of fuel-air mixture and initiates the full light-around which eventually leads to a stabilization of the single flames on the bluff bodies. After successful ignition, the pilot flame is switched off and the flow rates of air and fuel are linearly (constant Φ) increased over 10 s before Φ is increased over 5 s to reach the target operating condition.

2.4. Mode determination

The investigated operating conditions feature self-excited azimuthal modes, which occasionally show significant harmonic components. To separate the different components and harmonic contributions of the azimuthal modes (of order n), the pressure time series are bandpass-filtered with a bandpass width of $\Delta f = 100\ Hz$ centered on the peak frequency f_n.

To determine the nature of the azimuthal modes, the Quaternion formalism, introduced by Ghirardo and Bothien [34] is used. The acoustic pressure in an annulus can be represented as

$$p(\Theta, t) = A\cos{(n(\Theta - \theta))}\cos{(\chi)}\cos{(\omega t + \varphi)}$$
$$+ A\sin{(n(\Theta - \theta))}\sin{(\chi)}\sin{(\omega t + \varphi)}, \tag{1}$$

with Θ as the azimuthal coordinate and n describing the order of the mode. The orders $n = 1 - 5$ are herein referred to as the fundamental and the first to fourth harmonic frequencies. A describes the amplitude of the mode. The slowly varying real-valued angle $\theta(t)$ describes the angular location of the anti-nodal line and it is bounded between $-\pi$ and π. However, it is important to note that for an increasing order of the azimuthal modes, the number of anti-nodal lines increases. For example for $n = 1$, one anti-nodal line exists, whose position is described by θ or $\theta + \pi$, while a mode of $n = 2$ features two anti-nodal lines whose positions are described by θ or $\theta + \pi/2$. Subsequently, for an unambiguous description, each anti-nodal line position will be described in a range of $[0, \pi/n]$.

The nature angle is described by the slowly varying real-valued angle $\chi(t)$ and indicates whether the azimuthal eigenmode is a standing wave ($\chi = 0$), a pure clockwise (CW) or counterclockwise (CCW) spinning wave ($\chi = \mp\pi/4$) or a mix of both for $0 < |\chi| < \pi/4$. We adopt the reference frame where a CW spinning mode will rotate against Θ and a CCW spinning mode with Θ (see
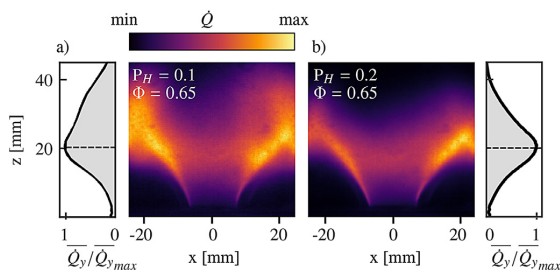
Fig. 2. Mean flame shape and corresponding streamwise distribution of the integrated heat release rate for stable operating conditions: $\dot{m}_a = 91.87 gs^{-1}$, a) P_H=0.1, $\Phi = 0.65$ and b) P_H=0.2, $\Phi = 0.65$.

Fig. 1). The fourth variable φ describes the temporal phase which is related to slow and small changes of the frequency.

3. Experimental results

3.1. General system response and stability maps

Mean flame shapes for two stable operating conditions are shown in Fig. 2 with the streamwise distribution of the integrated heat release rate depicted by grey plots on adjacent sides. Increasing hydrogen enrichment increases the flame temperature, laminar and turbulent flame speeds (see Table 1) and changes the Lewis number (as the diffusivity of hydrogen is high) which generally leads to shorter, more compact flames for the same power [35,36]. In comparison to the previous configuration [31] the flames are more compact and the modified bluff body leads to a wider flame angle with stronger flame-flame interactions at the end of the flame brushes which corresponds to the location of maximum heat release rate.

Although the flame is slightly more compact when $P_H = 0.2$, the location of maximum heat release rate remains at the end of the flame brush. It also reduces interactions with neighbouring flames. This is shown by the much larger interacting region for $P_H = 0.1$ in comparison to $P_H = 0.2$. For the $P_H = 0.1$ case, the flame brushes from adjacent flames can be seen to merge near the side edges of the image. This creates a large vertically oriented region of high heat release rate between the flames found along the sides of the image which extends downstream. This is not observed for the $P_H = 0.2$ flame although there is some evidence of interactions at the flame tips.

Fig. 3 shows the mean chamber pressure $\bar{p}$, bulk velocity u_b, fundamental azimuthal frequency f and the thermal power over a range of Φ for different $\dot{m}_a$ for $P_H = 0.1$. For clarity, data points for all mass flows are only displayed for $P_H = 0.1$, while $P_H = 0.15$ and 0.2 are plotted for $\dot{m}_a = 91.87 gs^{-1}$ only.

With increasing $\dot{m}_a$ and Φ the chamber pressure $\bar{p}$ increases from 1.5 to 3.3 bar. When $\bar{p} > 1.89\ bar$ the choked condition is reached resulting in a fully reflected condition. Therefore cases with $\dot{m}_a > 102.08\ gs^{-1}$ always result in a choked exit condition, while it depends on Φ for lower $\dot{m}_a$. In contrast to $\bar{p}$, u_b decreases with increasing Φ due to the increasing gas temperature and pressure. Nonetheless, increasing $\dot{m}_a$ leads to a slight increase in u_b. The increased flame temperature with hydrogen addition also affects the mean gas temperature in the chamber and thereby the oscillation frequency. The fundamental frequency f lies between $1450-1650\ Hz$ and increases with Φ as expected and is relatively insensitive to changes in $\dot{m}_a$ except at the lowest flow rate. At a fixed operating point an increase in P_H results in an increase of P and f whereas $\bar{p}$ and u_b remain almost unaffected noting that only small hydrogen mass fractions were investigated.

During the experiments the combustor exhibited both stable and unstable conditions, including a wide range of instabilities. Figs. 4 and E.6 display the amplitudes normalized by the chamber pressure and the nature angle of the azimuthal modes. Each sub-plot corresponds to a specific $\dot{m}_a$ and P_H. The color denotes the frequency of the azimuthal mode, e.g. light yellow denotes the fundamental frequency, while purple denotes the fourth harmonic. The normalized amplitude was calculated using the mean value of the Quaternion amplitude at the upper microphone normalized by the chamber pressure. The bar markers show the standard deviation of the time-series for three separate runs (separate test days) illustrating the repeatability of the experiments. A major difference to previous experiments at atmospheric pressures [11,13] is the occurrence of significant higher harmonics for high-amplitude instabilities which will be discussed later in the paper.

Focusing on the general system response first, Fig. 4 shows that the combustor is unstable over large parts of the stability map and stable at lean values of Φ as well as the lowest values of $\dot{m}_a$ for $P_H = 0.1$. With small amounts of hydrogen addition the normalized amplitudes of the fundamental eigenmode reach values that are near the peak values or higher than those found previously in atmospheric annular combustors [11–13]. Peak oscillation amplitudes occur for $P_H = 0.1$ and the largest $\dot{m}_a$. They reach 2% of the chamber pressure which translates to 6 kPa at the upper microphone and 8.5 kPa at the dump plane (evaluated from the multiple microphone method).

In all cases the onset of the instabilities occurs at leaner operating conditions with increasing $\dot{m}_a$. A similar trend is also found for increasing P_H.

Considering the case of $P_H = 0.1$, A increases slightly with $\dot{m}_a$. Just after the onset of the instability, the amplitude of the fundamental mode initially shows a weak but non-monotonic variation with Φ with a consistent dip in the amplitude occurring around $\Phi = 0.85$ after which further increases in Φ result in an increase in A. Overall, the amplitude variation of the higher harmonics also shows similar trends. The only notable difference being a slight decrease in A of the first harmonic for increasing Φ.

For $P_H = 0.15$, the onset of the instabilities occurs at leaner Φ, however the overall trends are similar to those observed for $P_H = 0.1$. Initially the amplitude of the excited fundamental mode is slightly lower compared to the $P_H = 0.1$ case but eventually increases to similar values. The amplitude variation with Φ shows a stronger non-monontic response and an increasingly pronounced dip in amplitude when $\dot{m}_a > 81.67\ gs^{-1}$. The location of the dip occurs at increasing equivalence ratio as $\dot{m}_a$ is increased and therefore exhibits a Strouhal number dependence (which is not shown directly here for brevity). The amplitude response of the harmonics follows the fundamental component closely. The harmonics only reach a significant amplitude when the amplitude of the fundamental mode is high. This *cut-on* behaviour is described later. It is also worth noting that at this hydrogen power fraction, self-excited instabilities appear for the lowest $\dot{m}_a$ reducing the stability window.

When P_H is increased to 0.2, the amplitudes are significantly lower compared to the previous cases. Only at stoichiometric conditions and lower mass flow rates does the amplitude of the fundamental mode surpass 1%.

While the results are not presented, at $P_H = 0.25$ the amplitudes of the instabilities continued to decrease. However, at this hydrogen power fraction occasional flashback events were observed at high Φ. For low levels of hydrogen addition, $P_H = 0 - 0.05$, the combustor was stable. Based on the large differences in amplitude for differing P_H one can see that the stability of the combustor is strongly affected by hydrogen enrichment and varying trends are observed for each distinct set of P_H cases.
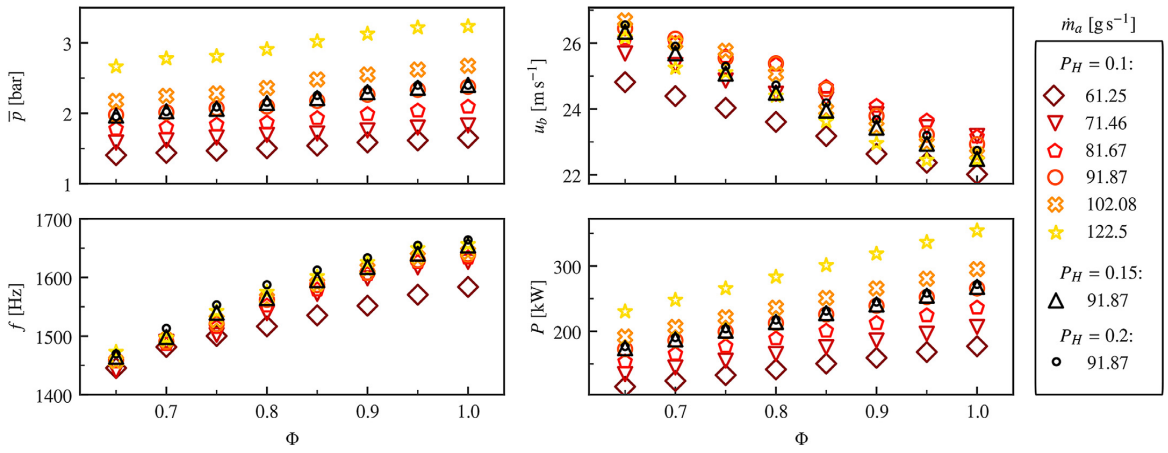
Fig. 3. Mean pressure $\overline{p}$, bulk velocity u_b, fundamental frequency of the azimuthal mode f and thermal power P as functions of $\dot{m}_a$, Φ and P_H.
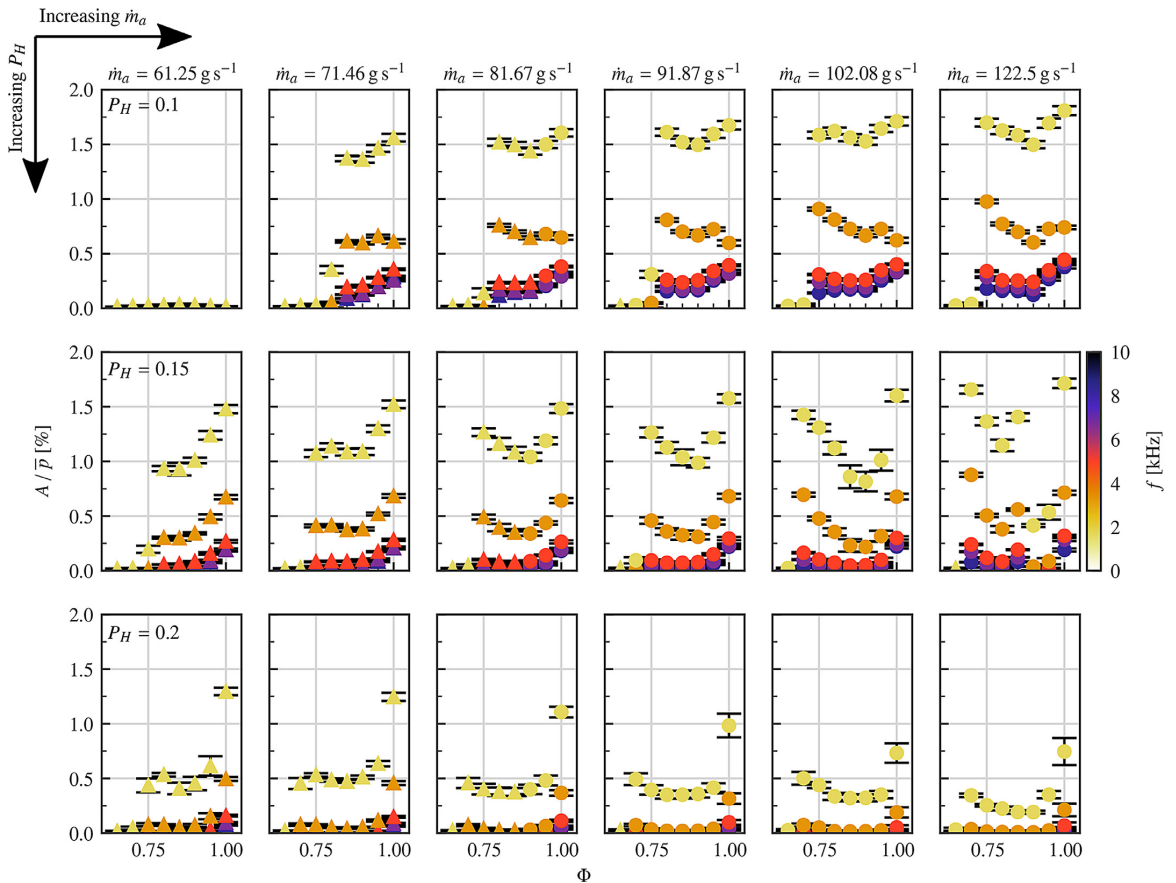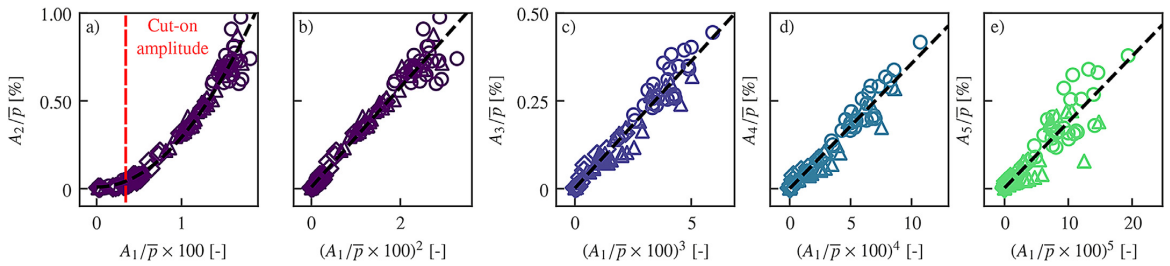

Fig. 4. Mean and standard deviation of the amplitude at the upper microphone for the azimuthal modes (order $n = 1 - 5$) as functions of $\dot{m}_a$, Φ and P_H. Color denotes the frequency. Triangular markers correspond to $\overline{p} < 1.89\ bar$, circles to choked conditions at $\overline{p} > 1.89\ bar$.

Fig. 5. Amplitude of the fundamental component $A_{n=1}$ versus amplitudes of the harmonic components $A_{n=2-5}$. Color denotes the order n of the azimuthal component and the marker P_H. Circular markers correspond to $P_H = 0.1$, triangles to $P_H = 0.15$ and diamonds to $P_H = 0.2$. Dashed lines depict the best quadratic (a) and linear (b-e) fits.

Interestingly, the general system response seems not to be altered when the choking condition is fulfilled, for example at approximately $\Phi = 0.9$ and $\dot{m}_a = 81.67\ gs^{-1}$ for all P_H. A likely reason for this is that the exit nozzle is already strongly reflecting for chamber pressures $> 1.5\ bar$ [37], thereby when the chamber pressure of 1.89 bar is approached there is not a drastic change in terms of the acoustic boundary condition.

3.2. Harmonic response

The presence of higher harmonics can indicate the presence of nonlinear dynamics. However modelling approaches such as the flame describing function (FDF) do not take them into account based on the assumption that harmonic contributions are small [38]. There are examples where harmonics can contribute significantly to the overall sound pressure level and be included within the FDF framework [39] and given the results presented so far are worth further investigation. The role of harmonics has been investigated previously for single burners under both self-excited [40] and forced conditions [41]. Until now, higher harmonics have not been observed in annular combustors at atmospheric conditions. Under pressurized conditions, their occurrence has been limited to operating conditions with strong intermittent flashback events that were coupled to large-amplitude oscillations [31]. As shown in Fig. 4, in the present work, harmonics corresponding to azimuthal modes of order $n = 2 - 5$ are excited for a wide range of operating conditions.

Fig. 5 plots the relative normalized amplitudes of the harmonics versus the fundamental and shows that there is a correlation between the amplitude of the fundamental and the amplitudes of the higher harmonics. A cut-on amplitude for the first harmonic can be identified in Fig. 5 a), which shows that the amplitude of A_2 only becomes significant when the normalized amplitude of A_1 surpasses $\approx 0.35\%$. Higher cut-on amplitudes were found for the higher harmonic contributions (not shown here). However, this cut-on behaviour cannot be solely due to the large amplitudes as significant harmonics have not been observed in atmospheric experiments with similarly large amplitude instabilities [42]. This strongly suggests that the choked exit conditions play an important role given that the acoustic reflection drops significantly with increasing frequency for an open end [43] in an atmospheric combustor. Similar to [40,41], we observe a quadratic dependence of the amplitudes of the first harmonic on the fundamental component. As shown in Fig. 5 the amplitude of the higher harmonics shows a dependence on the fundamental to the nth power although there is a notable increase in scatter with increasing order.

3.3. Nature angle and modal response

The nature angles of the self-excited modes are plotted in Fig. 6. Only data points exhibiting a normalized amplitude larger than

0.05% are included. In general, the system response near onset conditions leads to CCW spinning modes although there are some cases where standing modes occur. For conditions further away from the stability border the nature angle shows that most of the self-excited modes are strongly spinning in the CW direction over the instability range with the exception of the case where $P_H = 0.15$, $\dot{m}_a = 122.5\ gs^{-1}$ and $\Phi = 0.85$ which repeatedly features a strong CCW spinning mode with a normalized amplitude of 1.5% (see Fig. 4) and significant harmonics. For cases where $P_H = 0.2$ the nature angle shows that the predominantly CW spinning modes tend more towards mixed modes in comparison to the other cases.

The dynamics observed in these stability maps differ strongly from observations made in the atmospheric version of this combustor [11,12], which has the same dimensions except for the outlet boundary condition and the bluff bodies. In the present work, the spinning modes approach pure spinning modes which have, to date, not been typically found in *noisy* atmospheric annular combustors, which have showed a predominant tendency towards standing modes and mixed modes. A further difference is the suppression of modal dynamics [9], which we define as the instantaneous transitions between standing, spinning and mixed modes. In addition to the change in acoustic boundary conditions, these instabilities have comparably high limit-cycle amplitudes and are subsequently further away from the bifurcation point which may act to prevent instantaneous mode switching due to a larger potential barrier [16] between different attractors. Subsequently, the largest degree of switching and therefore an increased standard deviation, is observed close to the stability borders, while the mode was not observed to change nature as soon as the CW state was reached.

A handful of theoretical papers have tried to shed light on the mode selection in annular combustors [9,20,21,44,45]. Specifically, [45] showed that the ratio of the amplitude to background noise of the combustor is a key parameter that determines the nature of the mode. Thereby an increasing amplitude is expected to excite purer spinning modes. To the best of the authors' knowledge this has not been investigated experimentally. Fig. 7 shows the relation of A and χ on the fundamental and the harmonic components over the full range of operating conditions. Overall, Fig. 7 shows that as the amplitude increases the modes tend towards strongly CW spinning modes for all harmonics. Beginning with the fundamental mode, standing modes appear first at low amplitudes which then quickly transition towards CCW modes as the amplitude increases. At high amplitudes mixed/CW spinning modes become dominant. The occurrence of CCW spinning modes decreases with mode order as almost pure CW spinning states become dominant. This is related to the cut-on amplitudes observed in Fig. 5.

Fig. 7 also shows different behaviour to previous observations made in [31], where the higher order modes could have a different χ and showed a higher probability of standing modes. How-
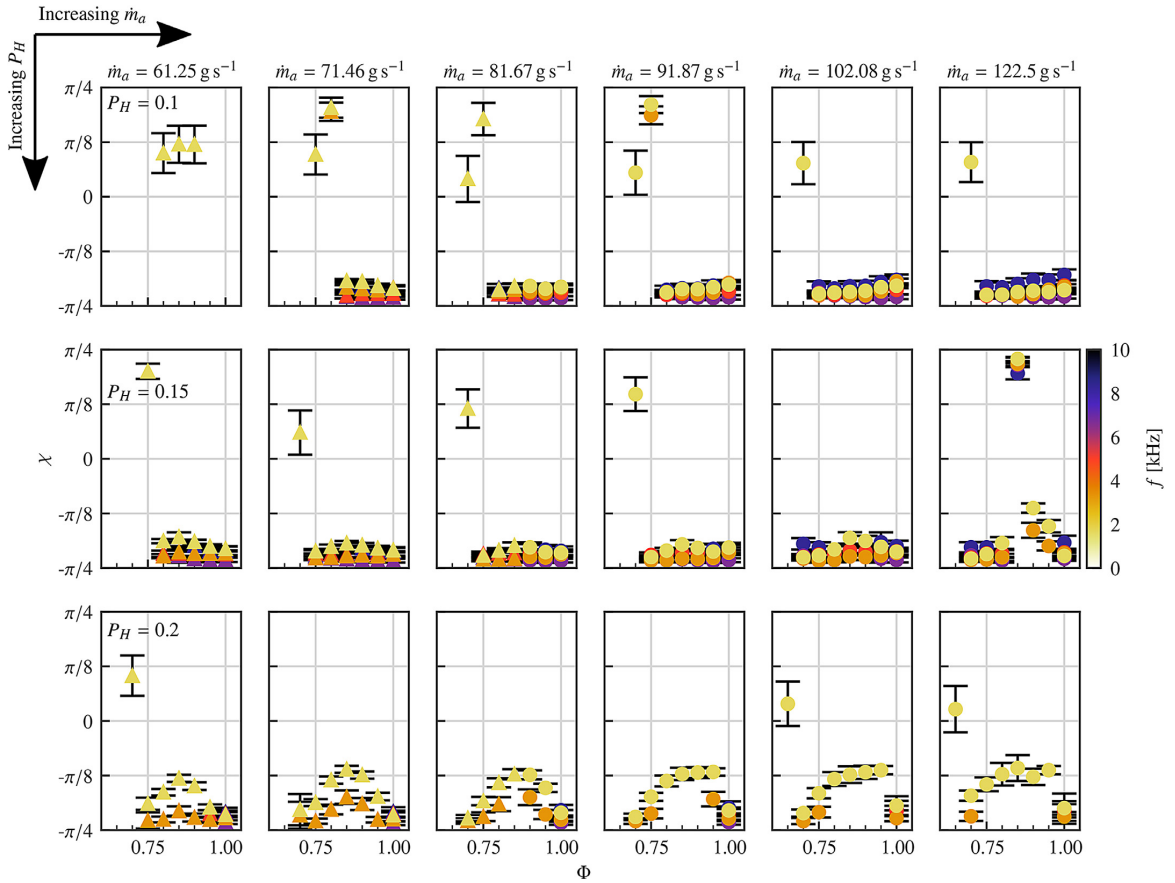
Fig. 6. Mean and standard deviation of the nature angle for the azimuthal modes (order $n = 1 - 5$) as functions of $\dot{m}_a$, Φ and P_H. Color denotes the frequency. Triangular markers correspond to $\bar{p} < 1.89$ *bar*, circles to choked conditions at $\bar{p} > 1.89$ *bar*.
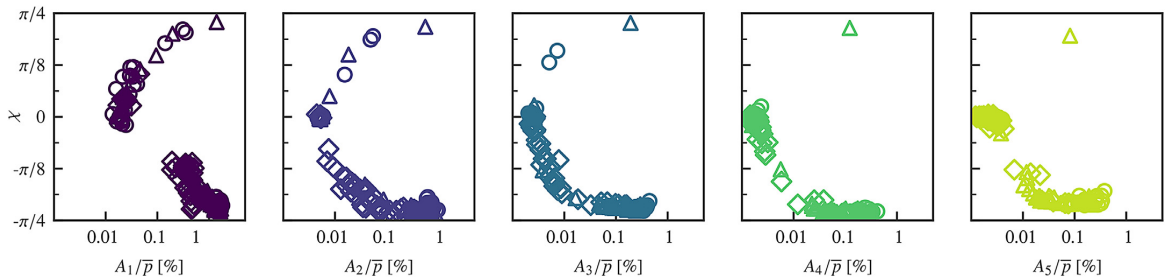
Fig. 7. Nature angle in dependence of the amplitude for the fundamental and harmonic components. Circular markers correspond to $P_H = 0.1$, triangles to $P_H = 0.15$ and diamonds to $P_H = 0.2$.

ever, that could be attributed to the occurrence of states where not all burners exhibited flashback which introduced a significant asymmetry in the heat release response over the annulus, thereby pushing the mode towards a standing mode [9,21].

Although not shown for brevity, it is worth mentioning that clearly preferred orientation angles for the pressure anti-nodes of the standing component, θ, were observed for each operating condition. While the modes are mostly strongly spinning and the standing component of the mode therefore had a minor amplitude,

a preferred θ is most likely an indicator of small geometrical asymmetries that lead to the anti-nodal line locking into a certain position [18,20]. When the harmonic components also showed a preferred orientation, the preferred nodal line position, θ_n, were not always same. For the cases studied it was often found that θ_1 and θ_2 collapsed, but that the higher harmonics preferred different orientations (see for example Fig. 9). For the $P_H = 0.1$ and 0.15 cases, θ_1 and θ_2 are centered around $20 - 30°$ but for $P_H = 0.2$ the pre-
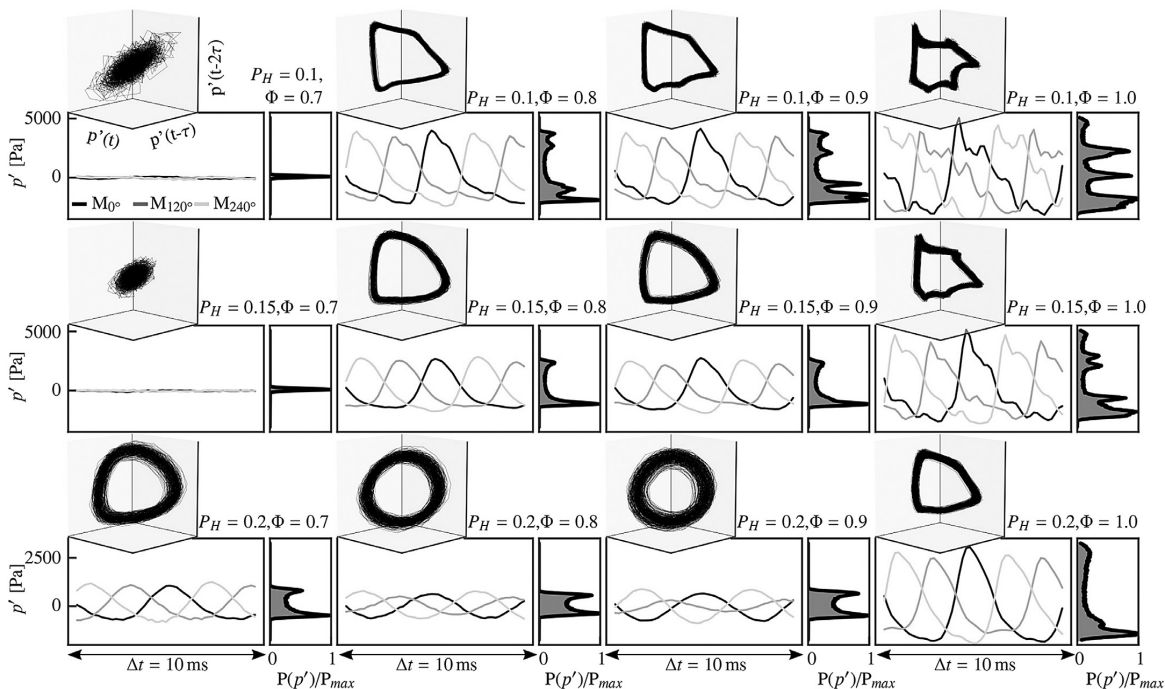
Fig. 8. Time-series, PDFs and phase space plots at $\dot{m}_a = 91.87\,gs^{-1}$ for differing Φ and P_H.

ferred anti-nodal line position transitions quasi-linearly from 60 to 30° for increasing Φ.

3.4. Time series and phase space

Fig. 8 aims to provide a more visual representation of how the harmonic contributions influence the time-series of the pressure fluctuations p'. The plotted data corresponds to $\dot{m}_a = 91.87\,gs^{-1}$ and compares the time-series (with corresponding PDFs) and the phase space plots for $P_H = 0.1 - 0.2$ (shown in rows) for different equivalence ratios, $\Phi = 0.7$, 0.8, 0.9 and 1.0 (shown in columns). The time-series data are cropped to segment lengths of 10 ms while the data used to calculate the PDFs corresponds to a segment of 5 s.

Focusing on the first row, the combustor is initially stable at $\Phi = 0.7$, which is visualized by random trajectories in phase space and the flat response of p'. At $\Phi = 0.8$ the combustor features a strong limit-cycle that has significant harmonic contributions which manifests in a distortion of the phase space and a highly asymmetric PDF which has its mean probability in the region of negative fluctuations. With increasing Φ the peak-to-peak amplitude increases along with the harmonic contribution, leading to a strongly distorted phase space and an increasing number of peaks in the PDF of p'.

As previously discussed, when P_H is increased the amplitude and the degree of harmonic contributions decrease. At $P_H = 0.15$ and $\Phi = 0.8 - 0.9$ the phase space is only slightly distorted resulting in a more sinusoidal response but still features an asymmetry in its PDF. For $\Phi = 1$ the signal is highly distorted with the PDF showing a different distribution compared to the lower hydrogen content case although the amplitude of the fundamental mode is comparable. Still, there is a higher probability of negative p' values, but two smaller peaks occur in the PDF for positive values. The

reason for this is that the amplitudes of the harmonics decrease with order. Higher harmonics are suppressed when $P_H = 0.2$ as is evident in the sinusoidal response in the pressure time-series. At $\Phi = 0.8 - 0.9$ the PDF is symmetric and the phase space shows a uniform torus which again becomes distorted for $\Phi = 1$.

Interestingly, one observes that higher harmonic contributions always lead to a deformation of the acoustic wave, such that the leading edge has a steeper slope than the trailing edge. This phenomenon is known as wave steepening and constitutes a well documented non-linear phenomenon [46].

3.5. Investigation of a high and low-amplitude instability operating condition

In this section we analyze two specific operating conditions more closely: One that features a high-amplitude mode with significant harmonics ($P_H = 0.1$, $\dot{m}_a = 91.87\,gs^{-1}$, $\Phi = 0.8$) and one featuring a low-amplitude instability ($P_H = 0.2$, $\dot{m}_a = 91.87\,gs^{-1}$, $\Phi = 0.8$) with weak harmonics. These cases were chosen as their operating conditions lead to chamber pressures which are high enough to choke the exit nozzle, while the thermal stress is still relatively low, enabling run times that bring the combustor close to thermal equilibrium. Extensive temperature measurements of these two cases are presented in Appendix C.

Fig. 9 shows the time-series, the sound pressure level (SPL) and PDFs of the three slow flow variables A, χ, and θ of the resulting modes.

The ramp procedure for both cases is identical and the onset of the instabilities occurs shortly before the target operating condition is reached. Comparing the SPLs, one can see drastic differences not only in the SPL of the fundamental component, which is more than 10 dB higher for $P_H = 0.1$ but also in the harmonic components which remain significant up to frequencies around 12 kHz.
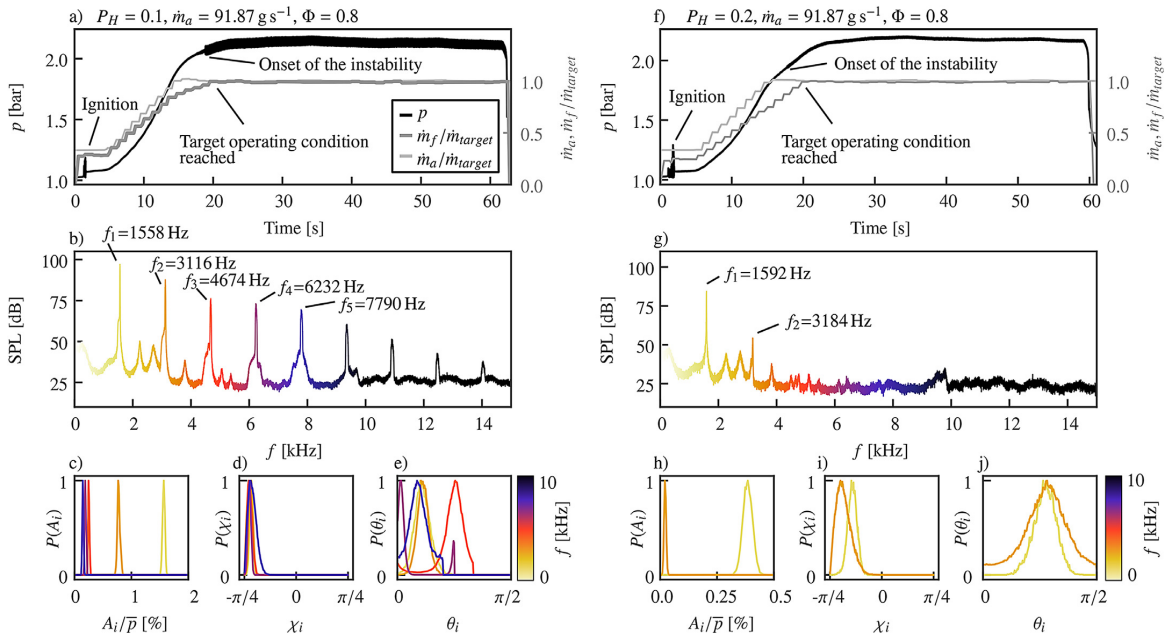
Fig. 9. Pressure time-series, sound pressure level (SPL) and PDFs of the slow flow variables for $P_H = 0.1$ (a-e) and $P_H = 0.2$ (f-j), $\dot{m}_a = 91.87$ g s^{-1}, $\Phi = 0.8$. The orientation angle θ is displayed from $[0, \pi/2]$ for viewing clarity as no occurrence of $\theta_{n=1} > \pi/2$ was observed.
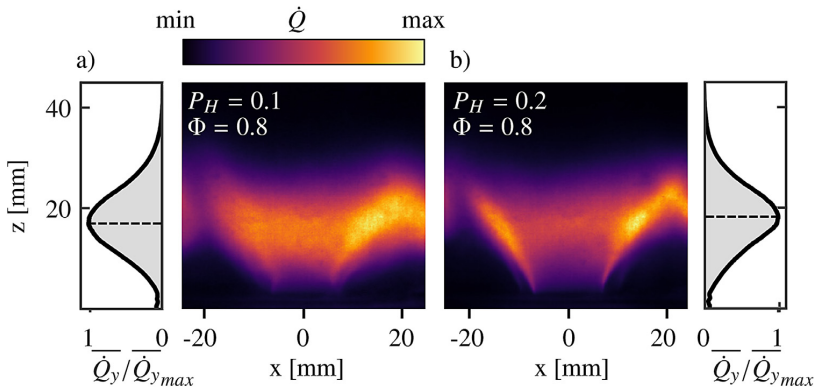
Fig. 10. Mean flame shape and corresponding streamwise distribution of the integrated heat release rate for unstable operating conditions: $\dot{m}_a = 91.87$ g s^{-1}, a) $P_H = 0.1$, $\Phi = 0.8$ and b) $P_H = 0.2$, $\Phi = 0.8$.

While both cases feature strongly CW spinning modes, χ is closer to a standing/mixed mode for $P_H = 0.2$. No major variability in χ is observed for the fundamental and the harmonic components at $P_H = 0.1$, but the nature angle of the fundamental mode is significantly lower compared to that of the first harmonic for $P_H = 0.2$.

For clarity, θ is displayed from $[0, \pi/2]$ as no occurrence of $\theta_{n=1} > \pi/2$ was observed. Generally, preferred anti-nodal line positions were observed for every n. For $P_H = 0.1$, the preferred θ for $n = 1, 2, 5$ lies at $\approx 20°$ whereas for $n = 3, 4$ it lies at $\approx 0°$ and 45° respectively. For $P_H = 0.2$, θ is only shown for $n = 1, 2$ as the amplitudes were very low for the higher harmonics. While the preferred anti-nodal line location for both orders is at $\approx 55°$, this location differs from the locations observed for $P_H = 0.1$.

For comparison to Fig. 2, the mean flame shapes for the investigated cases are shown in Fig. 10. One has to note that despite the

small differences in flame speed and temperature due to the different hydrogen mass fractions, the main difference between the two cases is the amplitude of the instability. Therefore any difference observed in the flame dynamics of the two cases is most likely related to the amplitude of the oscillation (and therefore only indirectly to P_H). During the instability, a drastic change in flame shape occurs for both cases leading to more compact flames. While the stable flames exhibit a slight asymmetry, this asymmetry is increased for the unstable flames leading to a stronger mean heat release rate on the right side of the flame. This may also be related to the effect of the spinning direction of the acoustic mode on the fluctuating heat release rate [47].

To investigate the flame dynamics of both cases, the phase-averaged responses are shown in Fig. 11. For the low-amplitude case (bottom row) flame shapes similar to the stable flames are
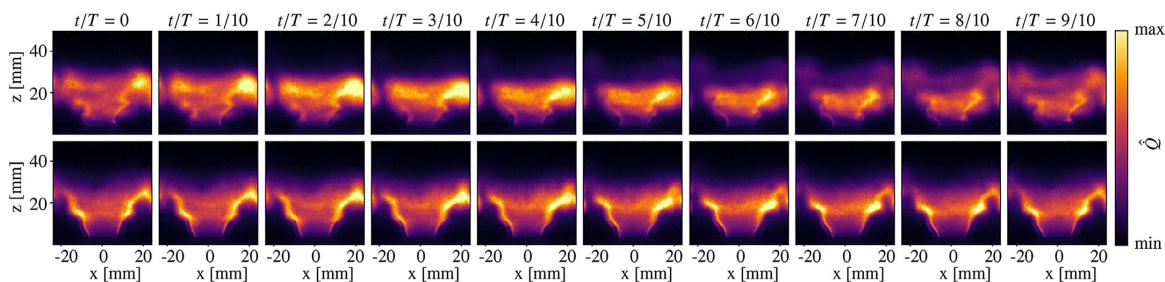
Fig. 11. Phase averaged images for $\dot{m}_a = 91.87\ gs^{-1}$ at $\Phi = 0.8$ and $P_H = 0.1$ corresponding to a high amplitude case (top row) and 0.2 corresponding to a low amplitude case (bottom row). Large modulations to the flame height and intensity are observed compared to the low-amplitude flame dynamics in the bottom row which shows the flame deformed by structures but not affecting the flame height. To calculate the phase averages, the images were divided in 20 bins based on the phase of the fundamental frequency which resulted in more than 300 images per bin.

observed and the flame height shows minimal variation over the cycle. In response to the velocity oscillations at the inlet, the shear layers roll-up leading to the formation of vortex structures which are advected downstream along the flame as can be seen by the modulations along the flame. The presence of such vortex structures is inferred, as these structures roll-up the flame, resulting in observable wrinkles in the phase average distribution. In the case of purely longitudinal velocity oscillations, distortions due to vortex-flame interactions would be axisymmetric. However, these azimuthal instabilties result in both longitudinal and azimuthal velocity oscillations, resulting in an asymmetric response, as shown by the side-to-side flapping motion. This asymmetry can be seen as a slight stagger between the wrinkles on either side of the flame. The flame roll up is also observed to be stronger on the right hand side ($t/T = 1/10 – 4/10$) which is likely the reason for the increased asymmetry in Fig. 10. This suppression of the shear layer disturbance on one side of the flame depending on the spinning direction was previously observed at atmospheric conditions in [47].

Much stronger modulations to the flame shape including a more pronounced asymmetric response appear for the high-amplitude case. This results in much stronger variation of the fluctuating heat release rate. The large pressure amplitudes manifest in strong axial and transverse motions of the flame which strongly distort the flame shape. The stronger transverse flapping motion at the base of the flame, are an indication of stronger azimuthal velocity oscillations. The resulting flame dynamics give rise to a region of peak heat-release rate on the right side of the flame where the interaction with the neighboring flame occurs.

4. Conclusion

The present work introduces an annular combustion chamber operating at elevated pressures and exhibiting self-excited combustion instabilities for a wide range of operating conditions. The largest amplitude self-excited response was found for a hydrogen content of 25% by volume while the amplitudes decreased for larger hydrogen contents. The amplitude of the instabilities showed a non-monotonic dependency on the chamber pressure (which is controlled by the air mass flow rate). While the amplitude tended to increase slightly with increasing pressure for 25% and 35% hydrogen, it decreased slightly for 43%. For all blends amplitude dips were observed at intermediate equivalence ratios. When the combustor featured a high-amplitude instability, significant harmonic contributions are observed, distinguishing these instabilities clearly from recent results in atmospheric combustors. Complex interactions between the fundamental and harmonic components were observed and a quadratic dependence between the amplitude of

a harmonic contribution and the respective lower order contribution was identified. The investigation into the harmonic contributions also revealed a cut-on amplitude at which harmonic contributions become significant. In terms of the nature of the modes, the combustor preferentially exhibited CCW spinning modes close to the stability borders, while all other modes were spinning CW. Fundamental and harmonic components were shown to have differing nature angles. These differences increased for low-amplitude instabilities. For the first time a clear trend between the amplitude and the nature of the azimuthal mode was observed, supporting recent theoretical studies [45] which predicted high-amplitude modes to be spinning while decreased amplitudes push the modes towards standing states. Time-series revealed the distortion of the pressure signals due to harmonic components which results in the leading edge of the pressure signal having a very steep slope during high-amplitude instabilities. Analysis of the flame dynamics also demonstrated the presence of significant asymmetry in the response during both low and high-amplitude instabilities, again distinguishing the response to these azimuthal modes. A thorough characterization of the setup is provided, giving a detailed description of the boundary conditions and thereby positioning this study as a possible baseline case for future simulation studies.

Declaration of Competing Interest

The authors declare that they have no known competing financial interests or personal relationships that could have appeared to influence the work reported in this paper.

Acknowledgments

Appendix A. Boundary conditions

A1. Effect of an additional upstream choking plate in the plenum

To evaluate the influence of the upstream boundary condition, a choking plate, resulting in a fully reflecting boundary condition, was introduced upstream of the glass bead section in the plenum. The choking plate consists of a 10 mm thick steel plate with 25 holes of diameter 2.2 mm. The investigated set of operating conditions is limited to $\dot{m}_a = 71.46\ gs^{-1}$. Amplitudes and nature angles
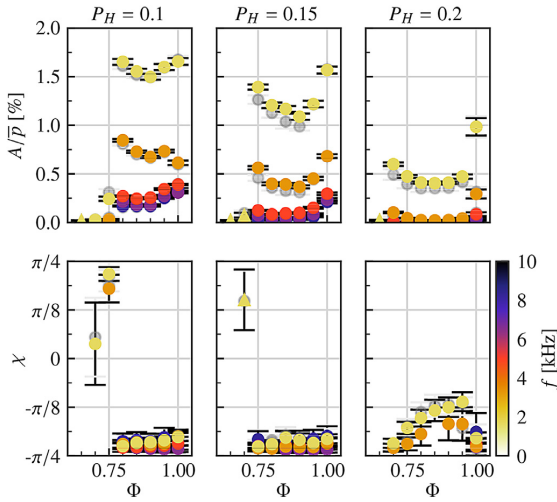
Fig. A1. Comparison of three data sets at $\dot{m}_a = 91.87\ gs^{-1}$ with (colored) and without (grey symbols) upstream choking plate.

are displayed in Fig. A1 and compared to the results without upstream choking plate (grey symbols).

Generally, few differences between the two configurations are observed. For $P_H = 0.1$ the normalized amplitudes collapse while A is slightly lower compared to cases without choking plate for $P_H = 0.15$ and 0.2. The onsets of the instabilities are identical and the nature angles show great comparability. In conclusion, the introduction of the upper choking plate does not alter the stability of the combustor in the investigated set of operating conditions. A likely reason for this is the large reflection coefficient of the sintered metal plate which effectively isolates the combustion chamber from the plenum.

A2. Acoustic characterization

Boundary conditions constitute crucial parameters for models aiming to predict the stability of a combustor. Subsequently the acoustic characterization of certain elements is essential and will therefore be presented hereafter. The framework of the scattering matrix, which this characterization is based on is well known and constitutes a convenient description to relate the acoustic interaction between two ducts. For details on the method, the interested reader is referred to [48]. In short, the scattering matrix

$$\begin{pmatrix} p_x^- \\ p_y^+ \end{pmatrix} = \begin{pmatrix} S_{11} & S_{12} \\ S_{21} & S_{22} \end{pmatrix} \begin{pmatrix} p_x^+ \\ p_y^- \end{pmatrix} \qquad (A.1)$$

which is used to characterize the element, relates the travelling wave amplitudes p^+ and p^- of two ducts x and y.

We use an impedance test rig based on two straight ducts which are equipped with microphones and connected by the investigated element. Speakers on both or one side act as an acoustic source and we use a total of five independent states. The scattering matrices for the sintered metal plate, the swirler and the glass bead section as well as a description of the setup are made available in the supplemental material S1. Figure A2 displays the S_{11} and S_{12} elements (for notation, refer to [48]) of the sintered metal plate's scattering matrix. For a frequency range up to 3kHz, $|S_{11}|$ lies between $0.7 - 0.8$ thereby describing a strongly reflective boundary which is likely to be the reason that the introduction of an upper choking plate does not alter the stability of the combustor.
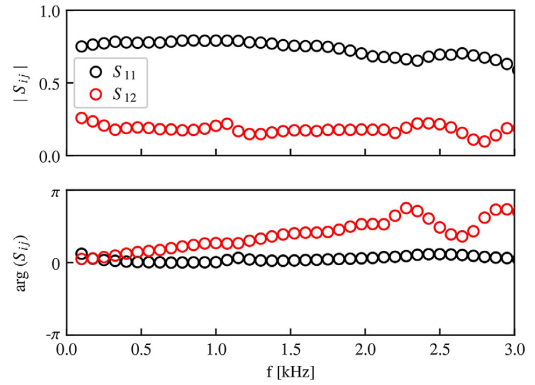

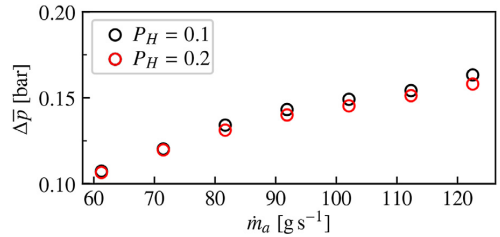**Fig. A2.** Scattering matrix of the sintered metal plate.

Fig. A3. Measured pressure drop over the sintered metal plate for $P_H = 0.1$, 0.2 and $\Phi = 0.8$.

A3. Pressure drop over the sintered metal plate

The sintered metal plate (SIKA B-100 from GKN) is made of brass, has a thickness of 22 mm and a porosity of 0.12 at a mean pore size of 183m. Figure A3 displays the measured pressure drop for all air mass flows at $\Phi = 0.8$ and $P_H = 0.1$ and 0.2.

Appendix B. Velocity exit profiles of the injectors

To investigate the exit velocity profiles, as well as the volume flow distribution over the injectors (i.e. the flow asymmetry in the combustor), hot-wire measurements were performed under atmospheric and cold flow conditions. The setup in use is a Dantec Streamline Pro-system equipped with a miniature single wire (55P11) with a probe size of 1.25 mm. The profile was measured 2 mm downstream of the dump plane and the probe was orientated both parallel and perpendicular to the traversing direction. The investigated flow rate is $\dot{m}_a = 91.87\ gs^{-1}$ and the measurements were performed in atmospheric conditions. Figure A4 shows the results for two traversing directions with the probe orientated in parallel. The profile shows a very symmetric pattern. In terms of the flow asymmetry of the full annulus, several injectors were investigated. A comparison of the mass flows calculated based on the measured velocity revealed less than 5% difference between the injectors. This indicates a very symmetric flow distribution.

Appendix C. Temperature measurements

The temperature measurements were performed with an Optris CT Laser 3MH infrared thermometer (spectral range 2.3m, temperature range 0–600°C and response time 2 ms). The measuring spot has a size of 4.5–8 mm depending on the measured location.

As the IR thermometer cannot measure temperatures through flames, the burner has to be switched off to read object temper-
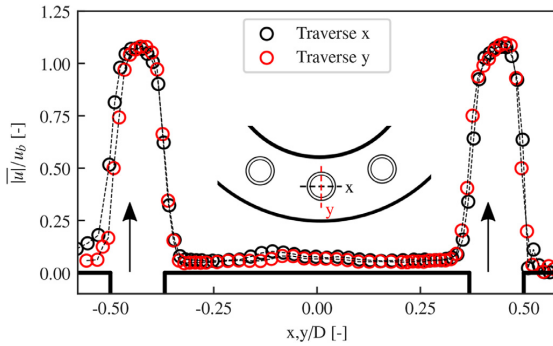
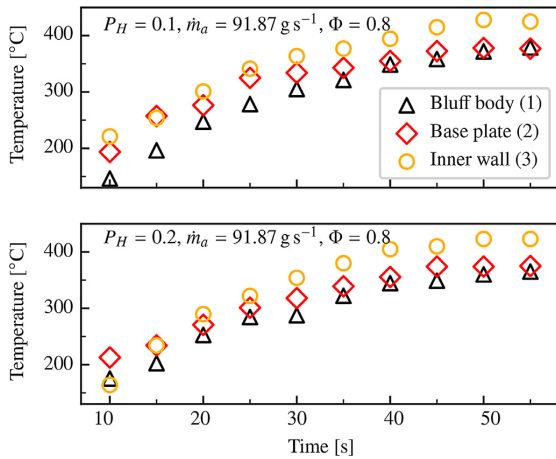**Fig. A4.** Velocity profile in x and y direction for one injector.

Fig. A5. Temperature T_1-T_3 corresponding to temperatures measured at the bluff body, base plate and inner wall for differing H_2 content.
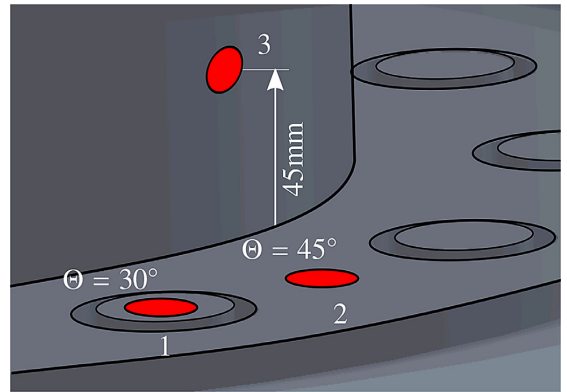

Fig. A6. Detailed view of the combustion chamber showing the measuring positions of the temperatures. Red circle depicts measuring spot.

Table D.2
Volume flow rates $\dot{V}$, inlet and outlet temperatures T_{in}, T_{out} and heat transfer P_{cool} for $\dot{m}_a = 91.87\ gs^{-1}$ at $\Phi = 0.8$ and $P_H = 0.1$ and $P_H = 0.2$.

	Circuit	$\dot{V}$ [L min^{-1}]	T_{in} [°C]	T_{out} [°C]	P_{cool} [kW]
P_H=0.1	Inner	32.9	8.1	55.6	109
	Outer	28.2	8.1	35	52.9
	Back	15.3	8.1	22.9	15.8
P_H=0.2	Inner	33	8	57.2	113.2
	Outer	28.1	8	35.2	53.3
	Back	15	8	22.8	13

ing on the condition the combustor is operated at, the outlet water temperature and thereby the heat transfer over the walls can vary significantly. For brevity, we will limit the information on the two operating conditions which were investigated in detail. The respective information can be found in Table D.2.

Appendix E

Supplementary material

Supplementary material associated with this article can be found, in the online version, at doi:10.1016/j.combustflame.2021.02.015.

atures (see approach of [49]). Subsequently for the full stability map, only the final temperatures of the bluff body were recorded. For the two operating conditions detailed in this work, more detailed measurements were performed at three locations: Bluff body ($\Theta = 30°$), back plane in between two bluff bodies ($\Theta = 45°$) and at the inner wall ($\Theta = 45°$) 45 mm above the dump plane (see Fig. A6).

To retrieve the transients, the temperatures were evaluated after different run-times, starting from the instant when the target air flow rate was reached ($t = 10\ s$). Practically, the combustor was ignited, run for a certain time, switched off and cooled down until a threshold temperature of the bluff body was reached and then ignited again. Figure A5 depicts the mean values of three runs for each run time up to 1m. One notes that the wall and bluff body temperatures start reaching thermal equilibrium after 50 s and lie at temperatures about $350 - 400°C$.

Appendix D. Water cooling

The water cooling is divided into three cooling circuits: back plate, inner wall and outer wall. The volume flow is measured by Omega FPB1400 paddle wheel meters and adjusted with control valves. For all operating conditions the flows are set to constant values: $\dot{V}_{inner} \approx 33\ Lmin^{-1}$, $\dot{V}_{outer} \approx 28\ Lmin^{-1}$, $\dot{V}_{back} \approx 15\ Lmin^{-1}$. The inlet water temperature fluctuates between 8-10°C. Depend-

References

[1] M.A. Gonzalez-Salazar, T. Kirsten, L. Prchlik, Review of the operational flexibility and emissions of gas- and coal-fired power plants in a future with growing renewables, Renew. Sustain. Energy Rev. 82 (2018) 1497–1513.

[2] M.R. Bothien, A. Ciani, J.P. Wood, G. Fruechtel, Toward decarbonized power generation with gas turbines by using sequential combustion for burning hydrogen, J. Eng. Gas Turbines Power 141 (2019) 121013.

[3] F. Halter, C. Chauveau, I. Gokalp, Characterization of the effects of hydrogen addition in premixed methane/air flames, Int. J. Hydrog. Energy 32 (2007) 2585–2592.

[4] E. Æsøy, J.G. Aguilar, S. Wiseman, M.R. Bothien, N.A. Worth, J.R. Dawson, Scaling and prediction of transfer functions in lean premixed h2/CH4-flames, Combust. Flame 215 (2020) 269–282.

[5] L. Rayleigh, The explanation of certain acoustic phenomena, Nature 18 (1878) 319–321.

[6] T. Poinsot, Prediction and control of combustion instabilities in real engines, Proc. Combust. Inst. 36 (2017) 1–28.

[7] B.T. Zinn, T.C. Lieuwen, Combustion Instabilities in Gas Turbine Engines: Operational Experience, Fundamental Mechanisms, and Modeling, The American Institute of Aeronautics and Astronautics, Inc., pp. 1–26.

[8] W. Krebs, P. Flohr, B. Prade, S. Hoffmann, Thermoacoustic stability chart for high intensity gas turbine combustion systems, Combust. Sci. Technol. 174 (2002) 99–128.

[9] N. Noiray, B. Schuermans, On the dynamic nature of azimuthal thermoacoustic modes in annular gas turbine combustion chambers, Proc. R. Soc. A Math. Phys. 469 (2013) 20120535.

[10] J.R. Seume, N. Vortmeyer, W. Krause, J. Hermann, C.-C. Hantschk, P. Zangl, S. Gleis, D. Vortmeyer, A. Orthmann, Application of active combustion instability control to a heavy duty gas turbine, J. Eng. Gas Turbines Power 120 (1998) 721–726.

[11] N.A. Worth, J.R. Dawson, Modal dynamics of self-excited azimuthal instabilities in an annular combustion chamber, Combust. Flame 160 (2013) 2476–2489.

[12] N.A. Worth, J.R. Dawson, Self-excited circumferential instabilities in a model annular gas turbine combustor: global flame dynamics, Proc. Combust. Inst. 34 (2013) 3127–3134.

[13] J.-F. Bourgouin, D. Durox, J.P. Moeck, T. Schuller, S. Candel, Self-sustained instabilities in an annular combustor coupled by azimuthal and longitudinal acoustic modes, Proceedings of the ASME Turbo Expo (2013). Paper No: GT2013–95010

[14] P. Wolf, G. Staffelbach, L.Y. Gicquel, J.-D. Mller, T. Poinsot, Acoustic and large eddy simulation studies of azimuthal modes in annular combustion chambers, Combust. Flame 159 (2012) 3398–3413.

[15] N. Zettervall, N. Worth, M. Mazur, J. Dawson, C. Fureby, Large eddy simulation of CH4-air and c2h4-air combustion in a model annular gas turbine combustor, Proc. Combust. Inst. 37 (4) (2019) 5223–5231.

[16] A. Faure-Beaulieu, T. Indlekofer, J.R. Dawson, N. Noiray, Experiments and low-order modelling of intermittent transitions between clockwise and anticlockwise spinning thermoacoustic modes in annular combustors, Proc. Combust. Inst. (2020), doi:10.1016/j.proci.2020.05.008.

[17] P. Berenbrink, S. Hoffmann, Suppression of dynamic combustion instabilities by passive and active means, Proceedings of the ASME Turbo Expo (2000). Paper No: 2000–GT–0079

[18] M. Bauerheim, P. Salas, F. Nicoud, T. Poinsot, Symmetry breaking of azimuthal thermo-acoustic modes in annular cavities: a theoretical study, J. Fluid Mech. 760 (2014) 431–465.

[19] J.R. Dawson, N.A. Worth, The effect of baffles on self-excited azimuthal modes in an annular combustor, Proc. Combust. Inst. 35 (2015) 3283–3290.

[20] N. Noiray, M. Bothien, B. Schuermans, Investigation of azimuthal staging concepts in annular gas turbines, Combust. Theor. Model. 15 (2011) 585–606.

[21] A. Faure-Beaulieu, N. Noiray, Symmetry breaking of azimuthal waves: slow-flow dynamics on the bloch sphere, Phys. Rev. Fluids 5 (2020) 023201.

[22] J.-F. Bourgouin, D. Durox, J.P. Moeck, T. Schuller, S. Candel, Characterization and modeling of a spinning thermoacoustic instability in an annular combustor equipped with multiple matrix injectors, J. Eng. Gas Turbines Power 137 (2014) 021503.

[23] J.P. Moeck, M. Paul, C.O. Paschereit, Thermoacoustic instabilities in an annular Rijke tube, Proceedings of the ASME Turbo Expo (2010). Paper No: GT2010–23577

[24] M.P. Boyce, Gas Turbine Engineering Handbook, Elsevier, 2012.

[25] M. Bauerheim, F. Nicoud, T. Poinsot, Progress in analytical methods to predict and control azimuthal combustion instability modes in annular chambers, Phys. Fluids 28 (2016) 021303.

[26] E. Freitag, H. Konle, M. Lauer, C. Hirsch, T. Sattelmayer, Pressure influence on the flame transfer function of a premixed swirling flame, Proceedings of the ASME Turbo Expo (2006) Paper No: GT2006–90540.

[27] W.S. Cheung, G.J.M. Sims, R.W. Copplestone, J.R. Tilston, C.W. Wilson, S.R. Stow, A.P. Dowling, Measurement and analysis of flame transfer function in a sector combustor under high pressure conditions, Proceedings of the ASME Turbo Expo (2003). Paper No: GT2003–38219

[28] F.D. Sabatino, T.F. Guiberti, W.R. Boyette, W.L. Roberts, J.P. Moeck, D.A. Lacoste, Effect of pressure on the transfer functions of premixed methane and propane swirl flames, Combust. Flame 193 (2018) 272–282.

[29] D. Fanaca, P.R. Alemela, F. Ettner, C. Hirsch, T. Sattelmayer, B. Schuermans, Determination and comparison of the dynamic characteristics of a perfectly premixed flame in both single and annular combustion chambers, ASME Turbo Expo (2008). Paper No: GT2008–50781

[30] D. Fanaca, P.R. Alemela, C. Hirsch, T. Sattelmayer, Comparison of the flow field of a swirl stabilized premixed burner in an annular and a single burner combustion chamber, J. Eng. Gas Turbines Power 132 (2010) 071502.

[31] M. Mazur, Y.H. Kwah, T. Indlekofer, J.R. Dawson, N.A. Worth, Self-excited longitudinal and azimuthal modes in a pressurised annular combustor, Proc. Combust. Inst. (2020), doi:10.1016/j.proci.2020.05.033.

[32] M. Philip, M. Boileau, R. Vicquelin, E. Riber, T. Schmitt, D. Durox, S. Candel, Large eddy simulations of the ignition sequence of an annular multiple-injector combustor, Proc. Combust. Inst. 35 (2015) 3159–3166.

[33] J.-F. Bourgouin, D. Durox, T. Schuller, J. Beaunier, S. Candel, Ignition dynamics of an annular combustor equipped with multiple swirling injectors, Combust. Flame 160 (8) (2013) 1398–1413.

[34] G. Ghirardo, M.R. Bothien, Quaternion structure of azimuthal instabilities, Phys. Rev. Fluids 3 (2018) 113202.

[35] J.-Y. Ren, W. Qin, F. Egolfopoulos, T. Tsotsis, Strain-rate effects on hydrogen-enhanced lean premixed combustion, Combust. Flame 124 (4) (2001) 717–720.

[36] H. Guo, B. Tayebi, C. Galizzi, D. Escudié, Burning rates and surface characteristics of hydrogen-enriched turbulent lean premixed methane–air flames, Int J Hydrog. Energy 35 (20) (2010) 11342–11348.

[37] M. Zahn, M. Betz, M. Schulze, C. Hirsch, T. Sattelmayer, Predicting the influence of damping devices on the stability margin of an annular combustor, Proceedings of the ASME Turbo Expo (2017). Paper No: GT2017–64238

[38] N. Noiray, D. Durox, T. Schuller, S. Candel, A unified framework for nonlinear combustion instability analysis based on the flame describing function, J. Fluid Mech. 615 (2008) 139–167.

[39] M. Haeringer, M. Merk, W. Polifke, Inclusion of higher harmonics in the flame describing function for predicting limit cycles of self-excited combustion instabilities, Proc. Combust. Inst. 37 (4) (2019) 5255–5262.

[40] K.T. Kim, Nonlinear interactions between the fundamental and higher harmonics of self-excited combustion instabilities, Combust. Sci. Technol. 189 (2016) 1091–1106.

[41] B.D. Bellows, Y. Neumeier, T. Lieuwen, Forced response of a swirling, premixed flame to flow disturbances, J. Propuls. Power 22 (5) (2006) 1075–1084.

[42] T. Indlekofer, A. Faure-Beaulieu, N. Noiray, J. Dawson, The effect of dynamic operating conditions on the thermoacoustic response of hydrogen rich flames in an annular combustor, Combust. Flame 223 (2021) 284–294.

[43] R. Munt, Acoustic transmission properties of a jet pipe with subsonic jet flow: I. The cold jet reflection coefficient, J. Sound Vib. 142 (3) (1990) 413–436.

[44] G. Ghirardo, M.P. Juniper, Azimuthal instabilities in annular combustors: standing and spinning modes, Proc. R. Soc. A Math. Phys. 469 (2157) (2013) 20130232.

[45] G. Ghirardo, F. Gant, Averaging of thermoacoustic azimuthal instabilities, J. Sound Vib. 490 (2013) 115732.

[46] B. Enflo, Theory of Nonlinear Acoustics in Fluids, Kluwer Academic Publishers, Dordrecht Boston, 2002.

[47] J.R. Dawson, N.A. Worth, Flame dynamics and unsteady heat release rate of self-excited azimuthal modes in an annular combustor, Combust. Flame 161 (2014) 2565–2578.

[48] M. Åbom, Measurement of the scattering-matrix of acoustical two-ports, Mech. Syst. Signal Process. 5 (1991) 89–104.

[49] Y. Ding, D. Durox, N. Darabiha, T. Schuller, Chemiluminescence of burner-stabilized premixed laminar flames, Combust. Sci. Technol. 191 (2019) 18–42.

The effect of hydrogen addition on the amplitude and harmonic response of azimuthal instabilities in a pressurized annular combustor
Supplemental material S1: Acoustic characterization

Thomas Indlekofer[a,*], Byeonguk Ahn[a], Yi Hao Kwah[a], Samuel Wiseman[a], Marek Mazur[b], James R. Dawson[a], Nicholas Worth[a]

[a]Department of Energy and Process Engineering, Norwegian University of Science and Technology, Trondheim N-7491, Norway
[b]CORIA-UMR 6641 Normandie Universit, CNRS-Universit et INSA de Rouen, Campus Universitaire du Madrillet, Saint Etienne du Rouvray, France

The acoustic characterization of several elements is done following the approach detailed in [1, 2]. The measurement setup is shown in Fig. 1. Two identical pipes with an inner diameter of 19 mm and 4 microphone ports were used. In the figure, both horn drivers are mounted however a total of five independent states was measured for each probe: left open - speaker right, left closed - speaker right, speaker left - speaker right, speaker left - right closed and speaker left - right open. The investigated frequency range was 100-3000 Hz. The method was validated by the investigation of an open pipe which resulted in the expected behavior without reflection (see Fig. 2). The result for the different elements of the combustor are shown in Figs. 3-5. Subsequently the sintered metal plate is highly reflective, practically isolating the combustion chamber from the plenum. The acoustic behavior of the swirler and the glass bead section is highly dependent on the frequency.

References

[1] M. Åbom, Measurement of the scattering-matrix of acoustical two-ports, Mech. Syst. Signal Pr. 5 (1991) 89–104.
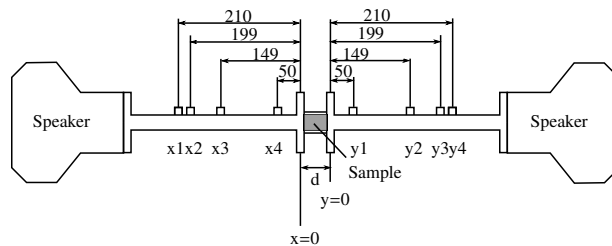[2] P. Davies, Practical flow duct acoustics, J. Sound Vib. 124 (1) (1988) 91–115.

Figure 1: Impedance measurement setup

*Corresponding author:
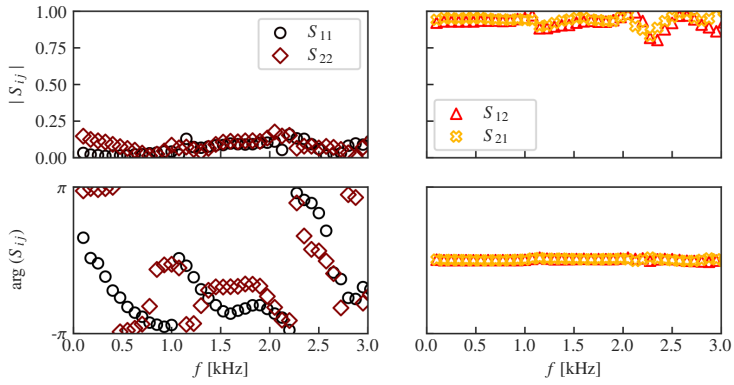Email address: thomas.indlekofer@ntnu.no (Thomas Indlekofer)

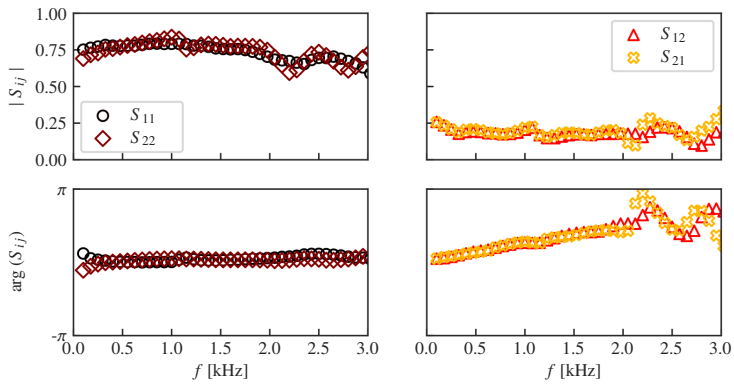Figure 2: Scattering matrix for the open pipe

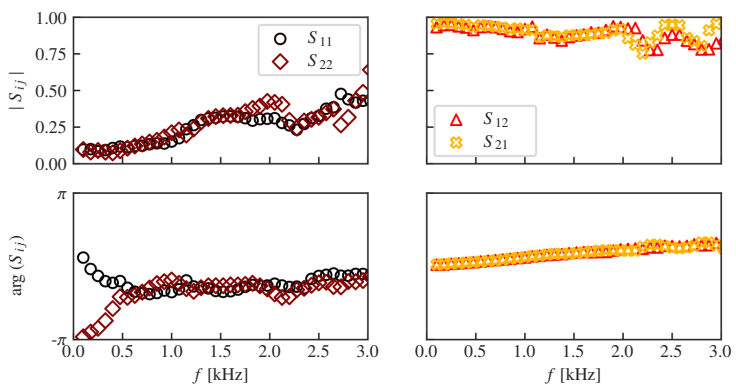Figure 3: Scattering matrix for the sintered metal plate
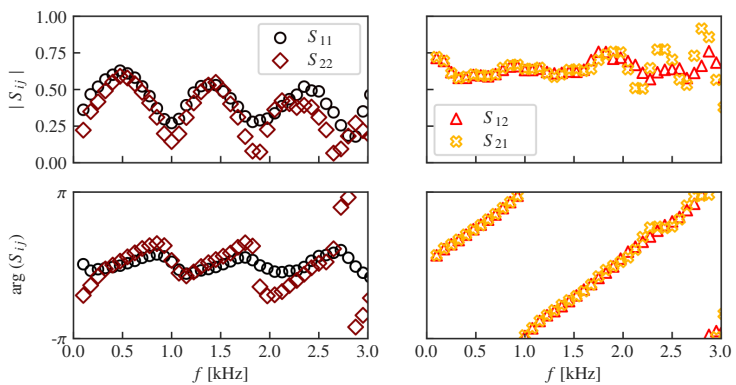
Figure 4: Scattering matrix for the swirler

Figure 5: Scattering matrix the the glass bead section

The role of fundamental and harmonic heat release rate components in self-excited azimuthal instabilities in a pressurized annular combustor with methane/hydrogen flames

Byeonguk Ahn, Thomas Indlekofer, James R. Dawson
and Nicholas A. Worth

Article VI

The effect of dynamic operating conditions on the thermoacoustic response of hydrogen rich flames in an annular combustor

Thomas Indlekofer, Abel Faure-Beaulieu, Nicolas Noiray
and James Dawson

The effect of dynamic operating conditions on the thermoacoustic response of hydrogen rich flames in an annular combustor

Thomas Indlekofer [a,*], Abel Faure-Beaulieu [b], Nicolas Noiray [b], James Dawson [a]

[a] Department of Energy and Process Engineering, Norwegian University of Science and Technology, Trondheim N-7491, Norway
[b] CAPS Laboratory, Department of Mechanical and Process Engineering, ETH Zürich, Switzerland

ARTICLE INFO

ABSTRACT

Self-excited thermoacoustic instabilities in symmetric annular combustion chambers typically give rise to spinning, standing and mixed azimuthal modes which are time-varying in nature and occur in a highly noisy environment due to turbulent combustion. We investigate the effect of linear ramps of increasing and decreasing equivalence ratio on the operating limits and thermoacoustic dynamics, from near lean blow-off to near flashback, in a laboratory scale annular combustor. The combustor features 12 lean-premixed hydrogen–methane flames at a fuel composition of 70% hydrogen and 30% methane by power. Equivalence ratio ramps were conducted for different thermal powers P=4, 6 and 8 kW per burner and three different ramp times t_{ramp}=5, 20, 60 s to simulate dynamic operation. It was found that ramping leads to self-excited instabilities that exhibit repeatable modal dynamics which depend on thermal power, ramp direction and duration. Different types of hysteresis were observed between the upward and downward ramps which affected the amplitudes and the stable operating range. The hysteresis phenomena also showed repeatable behaviour in terms of the nature and orientation angle. In one specific case, the simultaneous existence of two spinning modes was observed before the appearance of mode hopping leading to both an increase in frequency and doubling of the amplitude. High-speed OH* chemiluminescence of the flames showed that the mode hopping was accompanied by a change in the flame shape which becomes more compact and distributed.

1. Introduction

The motivation for this study stems from the recent drive by the gas turbine industry towards hydrogen combustion and dynamic operation to provide zero carbon power generation [1,2]. When operated flexibly, hydrogen fired gas turbines can play a vital role in accelerating the energy transition by providing stability to the grid through dynamic operation (varying load) enabling increased penetration of intermittent renewable power sources.

One of the main factors limiting the operating range of gas turbines are self-excited thermoacoustic oscillations [3–5]. These instabilities result from a constructive coupling between acoustics, flow, and the fluctuating heat release rate in the combustor. In annular combustion chambers, this is typically manifested by the propagation of acoustic waves in both azimuthal directions as observed in aeroengines and industrial combustors [5–7], and repro-

duced in laboratory combustors [8–10] as well as in high fidelity numerical simulations [11].

Over the last decade, the nature of azimuthal modes has received significant attention from the scientific community. The self-excited modes are generally classified as either standing modes whose nodal line remains fixed or slowly rotates around the annular chamber, spinning modes whose nodal line spins at the speed of sound, or a combination of both, forming mixed modes. A repeatable feature of azimuthally symmetric geometries with turbulent flames are time-varying changes in the azimuthal mode types resulting in instantaneous changes between spinning, standing and mixed modes at a fixed operating point [7–11]. These types of effects, which we will refer to herein as modal dynamics for simplicity, have not yet been observed in the case of laminar flames [12].

The effects of explicit symmetry breaking on azimuthal modes has also been investigated in a number of studies considering the effects of bulk swirl [8,13,14], different burner geometry [14–19] and baffles [20]. By contrast, the effects of explicit symmetry breaking on the nodal line and the orientation angle, has

not been investigated in detail except for [20]. In a symmetric annular combustor, the geometry is periodic, so counter propagating azimuthal waves with the same wavelength have no prescribed phase relationship. Therefore any observed preferred orientation of the nodal line indicates that small asymmetries are present which may be due to non-uniform geometry or flow conditions [16,18,21].

Although the occurrence of self-excited instabilities under transient operating conditions is very relevant for full-scale engines, for example during take off for aeroengines or under variable loads for power generation, it has only recently started to receive more attention. Earlier studies have shown that the presence of inherent noise from turbulence or external noise imposed by an actuator influences the thermoacoustic dynamics in the vicinity of subcritical Hopf bifurcations [22]. It has also been shown that hysteresis could be exploited to control operating limits [23]. More recently, in an afterburner configuration, an earlier onset of instability was reported for an increasing rate of change of the air flow rate [24]. Bonciolini and Noiray [25] showed that sufficiently fast ramps in equivalence ratio could bypass instability islands in a model gas turbine combustor. In a separate study by the same authors it was shown that thermal effects can also affect the system response under transient load [26]. In a multi-nozzle arrangement, both the absolute difference and the duration of the transient fuel staging affected the amplitude growth and decay of the instabilities [27].

The above mentioned studies only consider single flame configurations with the exception of the multi-nozzle array of [27], but none have been reported in symmetric annular combustors with turbulent flames which exhibit more complex modal response. Prieur et al. [28] showed that hysteresis altered the stability maps in the laminar flame matrix burner configuration of the MICCA facility at EM2C. By increasing and decreasing equivalence ratio at constant air flow, stability maps showed a "dual mode" region which depended on initial conditions. However, the paper did not consider the effects of turbulent flames or controlled linear ramps in equivalence ratio on the operating limits to simulate dynamic operation.

In this paper we characterise the system response during controlled linear ramps of increasing and decreasing equivalence ratio which features repeatable modal dynamics and hysteresis phenomena in an annular combustor with turbulent bluff body stabilised flames. The effect of different operating conditions and ramp parameters on amplitude, modal dynamics and hysteresis is investigated.

The paper is organised as follows: first we introduce the experimental setup, the operating and ramping conditions as well as the procedure to determine the nature of the azimuthal mode. Then the focus is put on the general system response to the ramping of the operating conditions before the hysteresis phenomenon is investigated in terms of the amplitude of the instabilities. Subsequently the effect of the ramping of the operating parameters on the nature of the mode and on the anti-nodal line positions is investigated before a mode hopping phenomenon is described.

2. Experimental setup, operating conditions and ramping procedure

Experiments were conducted using the atmospheric annular combustion chamber described in previous papers [8,9] with some modifications including the use of burners without swirl [29] as well as water cooled inner and outer enclosures. The setup of the annular combustor and a drawing displaying the dimensions are shown in Fig. A.1.

A premixed fuel-air mixture is fed into a cylindrical plenum that conditions and divides the flow into 12 axisymmetric burners. The burners are comprised of 150 mm long tubes with bluff bodies of 13 mm diameter equally spaced around the circumference

Table 1

Operating conditions in terms of the thermal power per injector P, the hydrogen power fraction P_H, the hydrogen volume fraction V_H, the adiabatic flame temperature of the mixture T_{ad}, the laminar flame speed of the mixture s_L, the bulk velocity $\bar{u}$, ramp direction and time, outer wall temperature when the ramps are initiated $T_{o, wall}$ and settling temperature of the cooling for the inner and outer wall $T_{i,c}/T_{o,c}$. The temperatures correspond to settling temperatures for ramps with increasing Φ.

| P [kW]	4	6	8
P_H		0.7	
V_H		0.876	
Φ	0.4–0.625	0.4–0.7	0.4–0.65
T_{ad} [K]	1376–1825	1376–1954	1376–1869
s_L [m s^{-1}]	0.076–0.513	0.076–0.706	0.076–0.575
$\bar{u}$ [m s^{-1}]	18–12	27–17	36–24
Ramp direction		Increasing and decreasing	
Ramp time [s]		5, 20, 60	
$T_{o, wall, 70}$ [°C]	420	435	455
$T_{i,c}$ [°C]	22	27	30
$T_{o,c}$ [°C]	21	23	25

of the annular combustor (30° between each injector). The outer diameter of the injector is 18.95 mm. The inner and outer walls of the chamber were 120 mm and 300 mm long respectively, with diameters of 127 mm and 212 mm. Water cooled walls were introduced to achieve long run times and achieve approximately constant wall temperatures. A separate cooling circuit for the inner and outer walls was employed. For the outer wall, chilled water flowed through four circumferentially spaced inlets near the combustor back plane which exited four outlets at the top. A similar arrangement was used for the inner wall but with 3 inlets and outlets. A schematic is shown in Fig. A.1b and c.

A summary of the operating conditions is reported in Table 1. The combustor is fueled with a perfectly premixed mixture. The fuel is composed of 87.6% hydrogen and 12.4% methane by volume. This translates to approx. 70% and 30% in terms of the power respectively (calculation based on the lower heating values given in ISO/TR 15916:2015). Each of the 12 individual burners was operated with a fixed power P of 4, 6 or 8 kW. Controlled linear ramps in terms of the equivalence ratio Φ covered the range of 0.4 to 0.625 (4 kW), 0.4 to 0.7 (6 kW) and 0.4 to 0.65 (8 kW) with the leanest conditions being near the lean blow-off limit and the richest near flashback.

The procedure for the controlled ramps was as follows: the burner was ignited near the lean blow-off limit for upward ramps and near the flashback limit for the downward ramps and remained at a fixed set point until the outer wall temperature $T_{o,c}$ reached thermal equilibrium. The air flow was then linearly increased or decreased with a ramp time t_{ramp} of 5, 20 or 60 s. After each ramp the combustor was cooled down, reignited and preheated before the next ramp was initiated. Wall temperatures were measured with up to 13 thermocouples (RS PRO Type K 1.5 mm). The cooling water flow was kept constant with an inlet water temperature of T_{in} = 10-13 °C. Depending on the operating point (P and Φ), the settling temperatures at the outlet varied slightly.

Typical temperature histories are shown in Fig. A.2(a) and (b) for one position located on the outer wall, 70 mm above the combustor back plane. The time period between the red lines denotes the ramping interval. Ramping cycles for increasing Φ were started 60 s after ignition, as shown in Fig. A.2(a). Ramping cycles for decreasing Φ were started 30 s after ignition to avoid long operation of the combustor close to the flashback limit.

The temperatures listed in Table 1 correspond to the temperatures that were reached when the increasing equivalence ratio ramps are initiated. It is important to appreciate that the temper-
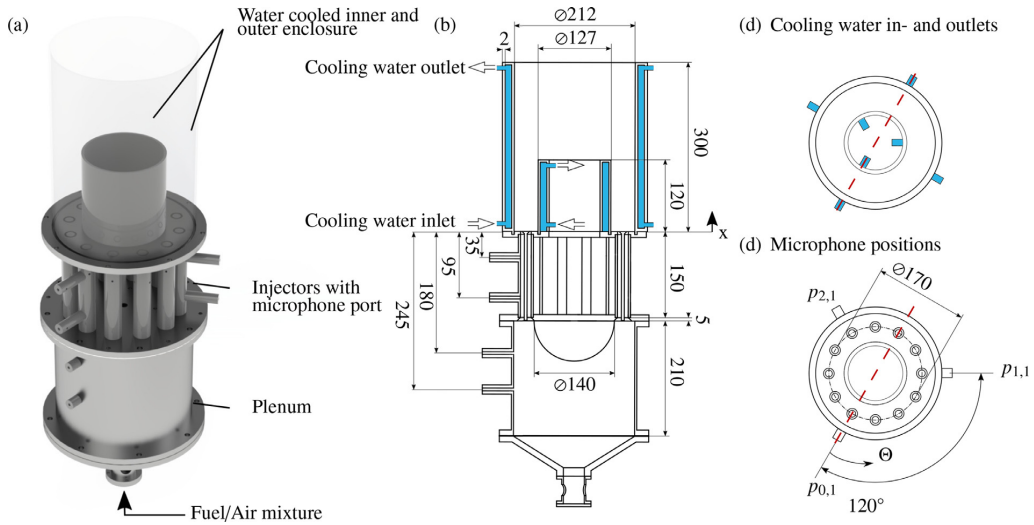
Fig. A.1. (a) Experimental setup of the model annular gas turbine combustor with 12 bluff body stabilised flames, (b) technical drawing, (c) detailed view displaying the in- and outlets of the cooling walls and (d) top view highlighting the azimuthal position of the microphones.
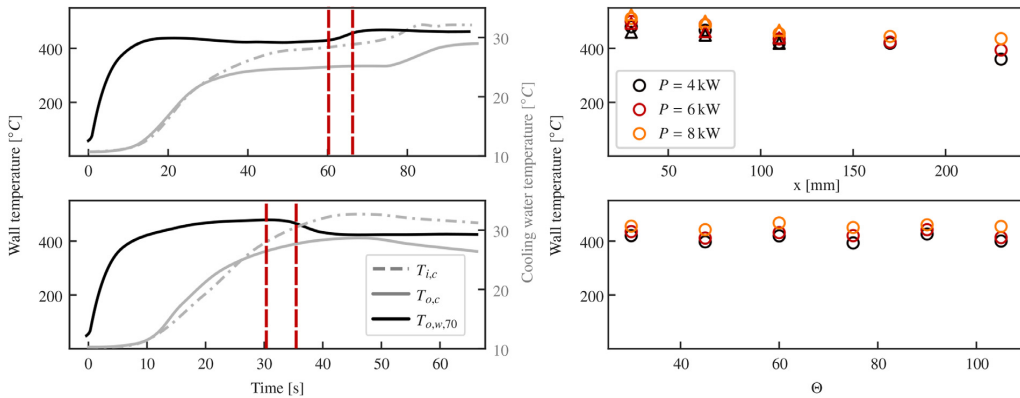
Fig. A.2. Outer wall temperature $T_{o,w}$ at $x_{T3} = 70$ mm and $\Phi = 30°$, cooling water temperature of the inner wall $T_{i,c}$ and of the outer wall $T_{o,c}$ for an (a) increasing and (b) decreasing equivalence ratio ramp with $P = 8$ kW and $t_{ramp} = 5$ s. (c) Longitudinal (at $\Theta = 30°$) and (d) circumferential (at $x = 70$ mm) wall temperature distribution at $t = 60$ s. Circular markers describe the outer wall, triangular markers the inner wall. (For interpretation of the references to color in this figure, the reader is referred to the web version of this article.)

atures change as a result of the ramping procedure and do not remain constant.

Figure A.2 (c) and (d) shows the longitudinal (at $\Theta = 30°$) and circumferential (at $x = 70$ mm) temperature profiles. The wall temperatures are clearly dependent on the power and decrease in downstream direction. Small differences between the wall temperature of the inner and outer wall were observed. In circumferential direction one notices that the temperatures differ for positions next to a burner or between two burners. The mean temperature variation in the azimuthal direction is approximately 10–20 °C and symmetric on a sector by sector basis which reasonably suggests that heat transfer does not have a significant impact on symmetry breaking.

To characterise the acoustic modes, 8 Kulite (XCS-093-05D) pressure transducers were mounted at three azimuthal ($\Theta = 0, 120, 240°$) and up to four longitudinal positions (see Fig. A.1). The signals were recorded with a sampling frequency of 51.2 kHz and digitised using a 24-bit DAQ system (NI model 9174).

Fluctuations in the heat release rate, $\dot{Q}(t)$, were obtained using a high-speed camera (Phantom V2012) with intensifier and UV filter ($\lambda = 310$ nm, FWHM 10 nm). The camera captures the OH*-chemiluminescence of the full annulus from the top (via a cooled mirror) or from the side. If images are acquired from the side, a shortened outer wall segment was placed on top of a quartz glass segment, thereby resembling the length of the cooled outer walls.

There was a small delay time between a decreased/increased mass flow through the mass flow controllers (MFC) and the actual mixture composition in the burner. Considering the wide range of flow velocities, this delay time was not constant but was estimated to be below 0.3 s for all cases.

3. Mode determination

To analyse the modes, we use the quaternion ansatz proposed in [30] that fully describes the acoustic pressure field associated azimuthal eigenmodes in annular combustion chambers. It
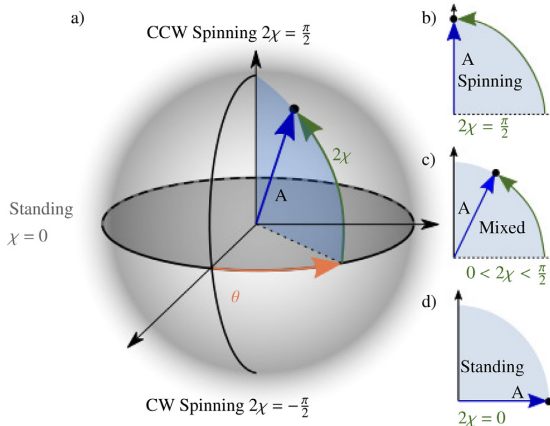
Fig. A.3. (a) Bloch sphere representation of the state of an azimuthal eigenmode, (b–d) illustrate the 3 types of states: pure spinning, pure standing and mix of the latter two states.

provides a set of four variables (Amplitude A, nature angle χ, orientation angle θ and temporal phase φ) which vary slowly with respect to the acoustic time-scale and constitutes a well-defined description of the state of the azimuthal thermoacoustic eigenmode. Using this notation, the acoustic pressure field corresponding to the first azimuthal mode (which is the subject of the experiments in this work) can be represented as

$$p(\Theta, t) = A \cos(\Theta - \theta) \cos(\chi) \cos(\omega t + \varphi) + A \sin(\Theta - \theta) \sin(\chi) \sin(\omega t + \varphi). \tag{1}$$

where θ is the slowly varying real-valued angular position anti-nodal line between $-\pi$ and π. It is important to note that at any instant, a state whose orientation angle is θ is the same as the state defined by $\theta + \pi$ and θ is therefore plotted between 0 and π. The slowly varying real-valued angle $\chi(t)$ indicates whether the azimuthal eigenmode is a standing wave ($\chi = 0$), a pure clockwise (CW) or counterclockwise (CCW) spinning wave ($\chi = \mp\pi/4$) or a mix of both for $0 < |\chi| < \pi/4$. The nature angle is directly related to the more commonly used spin ratio s by $s = \tan(\chi)$. Finally, the variable φ is the temporal phase which is related to slow and small changes of the instantaneous frequency. Even though φ is needed to fully describe the pressure field based on the quaternions, we will concentrate on A, χ and θ in this work. The reason for this is that φ does qualitatively not provide additional insight into the nature of the instability. For constant operating conditions φ shows a flat PDF without a preferential value and $\dot{\varphi}$ is centered around 0, indicating very little drift relative to the instability frequency. During the equivalence ratio ramp itself the frequency changes. This leads to constant rotation of φ which nonetheless exhibits a flat PDF but $\dot{\varphi}$ is not centered around zero any more.

While a comprehensive description of the quaternion formalism is available in [30], we provide details of how we handle and post-process the pressure signals in Appendix A.

A useful representation of the state of the thermoacoustic mode in terms of the first three slow-flow variables A, θ and 2χ at a given instant t is illustrated by Bloch sphere shown in Fig. A.3. The amplitude corresponds to the sphere radius A. The nature angle 2χ defines the latitude and the anti-nodal line direction θ is the longitude. Thermo-acoustic states positioned at the poles correspond to spinning modes, standing modes are located along the equatorial plane and mixed modes are located at intermediate longitudes between the equator and the poles.

4. Overview of the system response

Figure A.4 plots representative spectrograms for typical $t_{ramp} = 20$ s ramps and 3 different powers with the dominant self-excited modes shown on the left hand side. The self-excited modes were characterised using dynamic pressure measurements from 8 locations shown in Fig. A.1 and the corresponding dominant modes calculated from an acoustic solver [31] using an approximated temperature field divided into a burnt region in the combustor volume and unburnt region everywhere else. While the solver identifies multiple modes in the relevant frequency range, the number of modes can be reduced by comparing with reconstructed modes from the pressure measurements using the multiple microphone method which showed that the observed mode was of first azimuthal order (see Suppl. material for more information). The predicted frequencies, longitudinal and azimuthal components were in good agreement. Similar to earlier studies of combustion instabilities in annular combustion chambers open to atmosphere (e.g. [32]), the amplitude of the mode is relatively low in the combustion chamber as instability is driven by the acoustics of the injection unit. Note that in contrast to earlier investigations [8,29], the frequency was comparably lower due to a combination of factors including different fuels and operation at very lean equivalence ratios resulting in lower temperatures.

For $P = 4$ kW the instability frequency slowly increases during the ramp. The combustor becomes unstable after around 70 s initially having a frequency of 881 Hz which increases to 900 Hz at the final operating condition and corresponds to the mode 1A1L, with first azimuthal and first longitudinal orders. For $P = 6$ kW, initially a low-amplitude 1A2L mode with a frequency between 1100 and 1150 Hz is unstable and switches to the high-amplitude 1A3L mode which has a frequency around 1330–1370 Hz. Note that both modes coexist for a short time; the features of this mode hopping process are presented later. Only the 1A3L mode ($f = 1370$ Hz) is self-sustained when the power is increased to $P = 8$ kW. The predicted frequencies of the passive acoustic simulation (solution of the Helmholtz equation with non-uniform temperature field without active flame element) were 836 Hz, 1124 Hz and 1327 Hz respectively.

Figure A.5 plots the effect of upward and downward ramps on the time-series of p', A, χ and θ when the burners are operated at 4 kW. Upward and downward ramps are shown on the left and right hand sides of the figure respectively. During the upward ramp the transition from a stable state to a limit cycle is accompanied by a linear increase in A beginning at approximately $t > 105$ s.

The evolution of χ, shows that the self-excited mode initially transitions from a low-amplitude standing mode to a switching spinning mode whose spinning direction switches periodically, to a mixed clock-wise (CW) mode and back to the quasi-periodic switching of the spinning direction. The angular position of the anti-nodal line also follows a clear trend remaining constant during intervals where χ is not switching. However, when the modes are regularly switching their spinning direction, the anti-nodal line switches between $\theta = 60°$ which is coincident with a burner and $\theta = 135°$ which is in between two burners. The switching of θ occurs simultaneously with maxima and minima of χ, as shown in the detailed views provided on the right hand side of Fig. A.5 and in the joint PDFs in Fig. A.6.

The periodic evolution of χ manifest itself with a beating phenomenon in the acoustic signals of the individual microphones with amplitude oscillations of around 200 Pa. Figure A.6 shows that the modal dynamics follow a very clear pattern with one switching cycle (from 1 to 5 in Fig. A.6) taking around 0.75 s. The slight asymmetry in the joint PDFs also shows that the amplitude is larger when the mode spins in CW direction and that a CCW spinning direction is preferred. Preference for different spinning
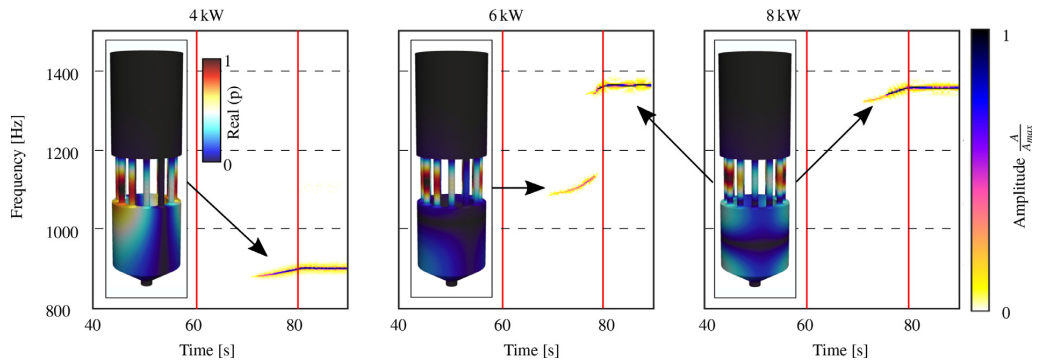
Fig. A.4. From left to right: typical spectrograms at $P = 4$ kW, $P = 6$ kW and $P = 8$ kW. All spectrograms correspond to ramps with $t_{ramp} = 20$ s. Color denotes the amplitude and the red lines show the start and end of the equivalence ratio ramps. The left side of each subplot shows the result of a passive acoustic simulation depicting the corresponding mode shapes: 1A1L, 1A2L and 1A3L. (For interpretation of the references to color in this figure, the reader is referred to the web version of this article.)
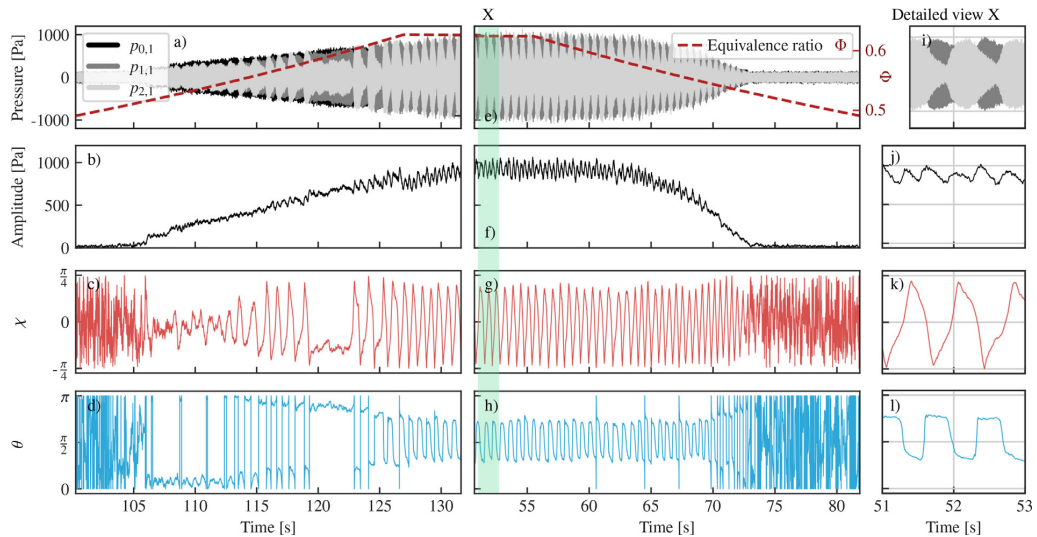
Fig. A.5. Comparison of an increasing (a)–(d) and decreasing (e)–(h) equivalence ratio ramp with $t_{ramp} = 60$ s at $P=4$ kW. The plot highlights the ramp from an equivalence ratio of 0.5 to the 0.625. (a) and (e) show the raw pressure signals corresponding to the upper microphones at 0, 120 and 240° ($p_{0,1} - p_{2,1}$). The dashed red line indicates the equivalence ratio. (b) and (f) indicate the amplitude, (c) and (g) the nature angle and (d) and (h) the orientation angle of the azimuthal mode. (i) to (l) correspond to detailed views at instants indicated by the shaded green area.
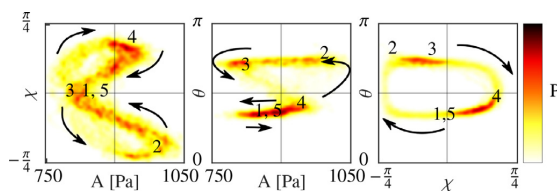

Fig. A.6. Joint PDF of amplitude, nature angle and orientation angle for the high-amplitude switching mode at $P=4$ kW and $\Phi = 0.65$.

directions was previously observed in a similar set-up by Mazur [29] which was attributed to small imperfections in the azimuthal symmetry.

The system dynamics during the downward ramp is distinctly different. As Φ is linearly decreased, A remains approximately con-

stant while the spinning-direction-switching dynamics persist several seconds before starting to decrease. Instead of a linear decrease in A, a power law decay to stable conditions is observed. A further difference is that the system does not return to the low-amplitude standing modes observed near the bifurcation point during the upward ramp. Neither does it return to the mixed CW mode with a constant nature and orientation angle.

A likely reason for the different system response to the ramping direction are the different initial conditions. Ramping up from stable conditions the flames responds linearly to finite perturbations which excite standing modes near the bifurcation point. As A increases to limit-cycle conditions, the system favours spinning modes, in particular a state where spinning modes switch direction. On the downward ramps the initial conditions begin in the switching state under limit-cycles. Therefore, the flames do not respond linearly to changes in Φ resulting in hysteresis and changing the stable operating limits as discussed in the next section.
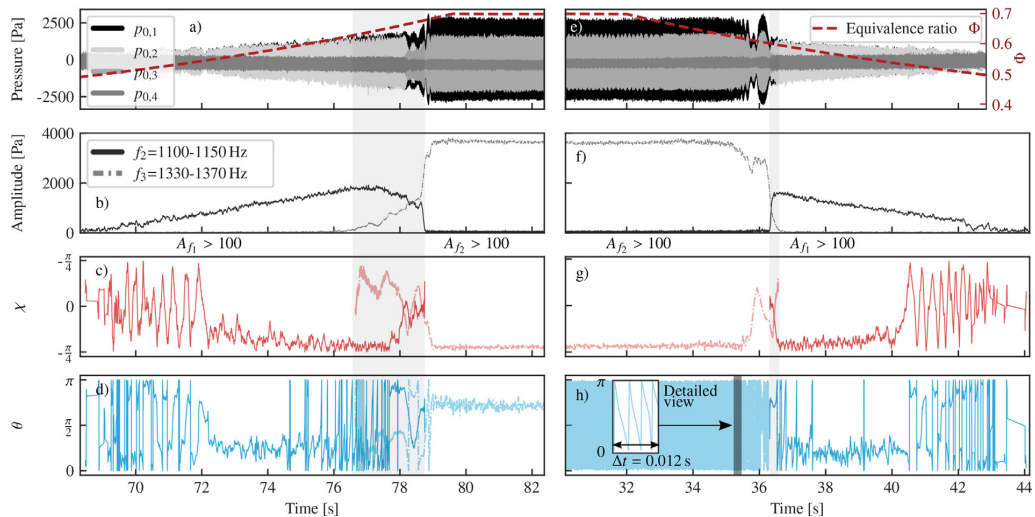
Fig. A.7. Comparison of an increasing (a)–(d) and decreasing (e)–(h) equivalence ratio ramp with $t_{ramp} = 20$ s at $P=6$ kW. The plot highlights the ramp from an equivalence ratio of 0.48 to the 0.7. (a) and (e) show the raw pressure signals corresponding to the four longitudinally spaced microphones at $0°$ ($p_{0,1} - p_{0,4}$). The dashed red line in (a) and (e) indicates the equivalence ratio. (b) and (f) indicate the amplitude, (c) and (g) the nature angle and (d) and (h) the orientation angle of the azimuthal mode. The solid lines show the mode at $f_3=1330–1370$ Hz, the dashed lines the mode at $f_2=1100–1150$ Hz.

Although the cooled walls minimise thermal inertia, as shown in Fig. A.2, they may still have a non-negligible effect on the system response.

Figure A.7 shows upward and downward ramps for $P=6$ kW. During the upward ramp, the 1A2L is first unstable, transitioning rapidly to the 1A3L mode resulting in a frequency jump from approximately $f_2 = 1150$ Hz to $f_3 = 1350$ Hz. The mode change occurs when Φ exceeds 0.6 (see the corresponding spectrogram in Fig. A.4). During the upward ramp, an 1A2L mode with a frequency f_2 becomes unstable, showing first a switching behavior before it becomes a predominantly CW spinning mode at ≈ 73 s until the ramp reaches $\Phi = 0.6$ when the 1A3L mode becomes unstable. These two modes of different longitudinal acoustic pressure distribution coexist, with no preferred θ. At $t=76$ s, these modes spin in opposite direction, then they become quasi-standing modes at around 78 s. After $t > 79$ s, the first mode disappears and the higher frequency mode dominates, resulting in a higher amplitude limit-cycle as an almost pure CW spinning mode.

A very similar evolution of the transient thermoacoustic dynamics is found during the downward ramp. The main difference is a reduced interval when both eigenmodes coexist. Interestingly, θ is significantly different for both ramp directions during the high-amplitude spinning mode which is expected to result from the different initial conditions. The combustor is ignited under stable conditions for the upwards ramp, which develops a clearly preferred orientation angle for the high amplitude spinning mode. For the downwards ramp tests, the combustor is ignited at a condition exhibiting a very robust, quasi perfectly spinning mode and then ramped down. During the first phase of the ramping down, the 1A3L mode remains quasi-perfectly spinning with a relatively fast drift of the preferred direction, at about 250 Hz, which is not that slow compared to the 1350 Hz of the acoustic time scale. The signature of this precession of the instantaneous state in the immediate vicinity of the pole of the Bloch sphere is hardly noticeable from the acoustic time traces. An interesting difference to Fig. A.5 is that the 1A2L mode shows a similar linear growth for both ramp directions.

Figure A.8 plots $t_{ramp} = 5$ s ramps for 8 kW and shows different behaviour. The combustor becomes thermoacoustically unstable, with a transient growth of the 1A3L mode from $\Phi=0.5$ and shows an irregular amplitude growth in contrast to the approximately linear growth observed for $P = 4$ and 6 kW. Initially, the limit cycle is a standing mode and the anti-nodal line has a clearly preferred position around $\theta = 60°$. The standing mode undergoes a jump in amplitude at $t=63.7$ s which lasts 0.5 s until the mode suddenly becomes a CW spinning mode following a second amplitude jump. The standing wave component of the CW spinning mode shows a preferred anti-nodal line position at $\theta = 120°$, which corresponds to a burner location.

On the downward ramp, a CW mode having a similar amplitude self-oscillates but the preferred anti-nodal line position has moved to a location between two burners at $\theta = 135°$. When Φ is decreased the amplitude of this CW mode persists for a couple of seconds before decaying. The high amplitude standing mode observed in the upward ramp does not appear and the amplitude shows two main decay rates compared with the stepped amplitude profile of the upward ramp. The transition to a standing mode at an amplitude of 2000 Pa is accompanied with a switch to the same preferred anti nodal line position as during the increasing ramp.

5. Hysteresis of the thermoacoustic amplitude

The effect of different t_{ramp} and P on the operating limits is shown by the plots A versus Φ in Fig. A.9. The ramp times of 5, 20 and 60 s are colour coded with the thickness of the lines representing the standard deviation from a minimum of 7 runs for each case.

Figure A.9 (a) plots the effect of ramp times and direction for $P = 4$ kW. All upward and downward ramp sequences show hysteresis effects demonstrated by the shift in the bifurcation points for the different ramp time and directions. During upward ramps, the combustor becomes unstable at around $\Phi = 0.5$ for slow ramp times but remains stable until approximately $\Phi = 0.52$ for the fast ramp time. During the downward ramps there is a clear distinction
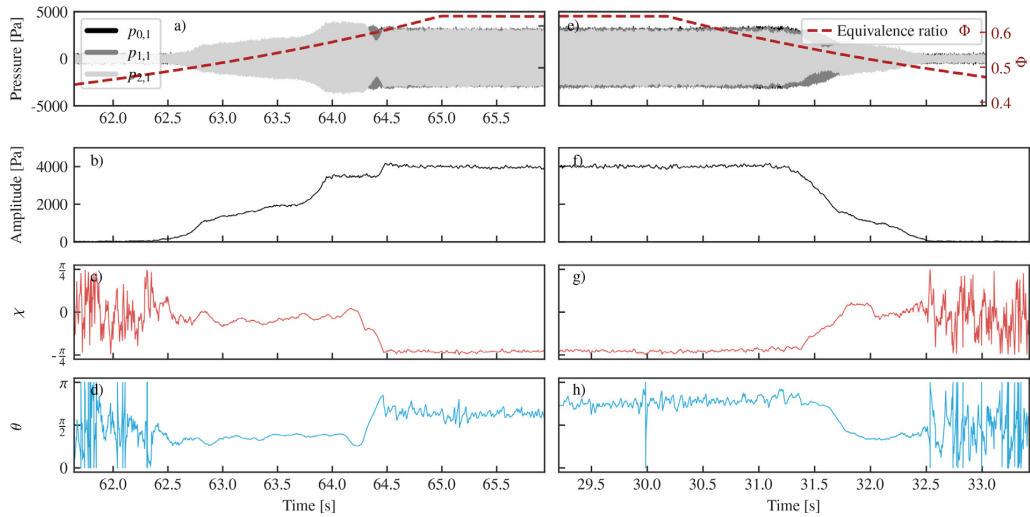
Fig. A.8. Comparison of an increasing (a)–(d) and decreasing (e)–(h) equivalence ratio ramp with t_{ramp} = 5 s at P=8 kW. The plot highlights the ramp from an equivalence ratio of 0.48 to the 0.7. (a) and (e) show the raw pressure signals corresponding to the upper microphones at 0, 120 and 240° ($p_{0,1} - p_{2,1}$). The dashed red line in (a) and (e) indicates the equivalence ratio. (b) and (f) indicate the amplitude, (c) and (g) the nature angle and (d) and (h) the orientation angle of the azimuthal mode.
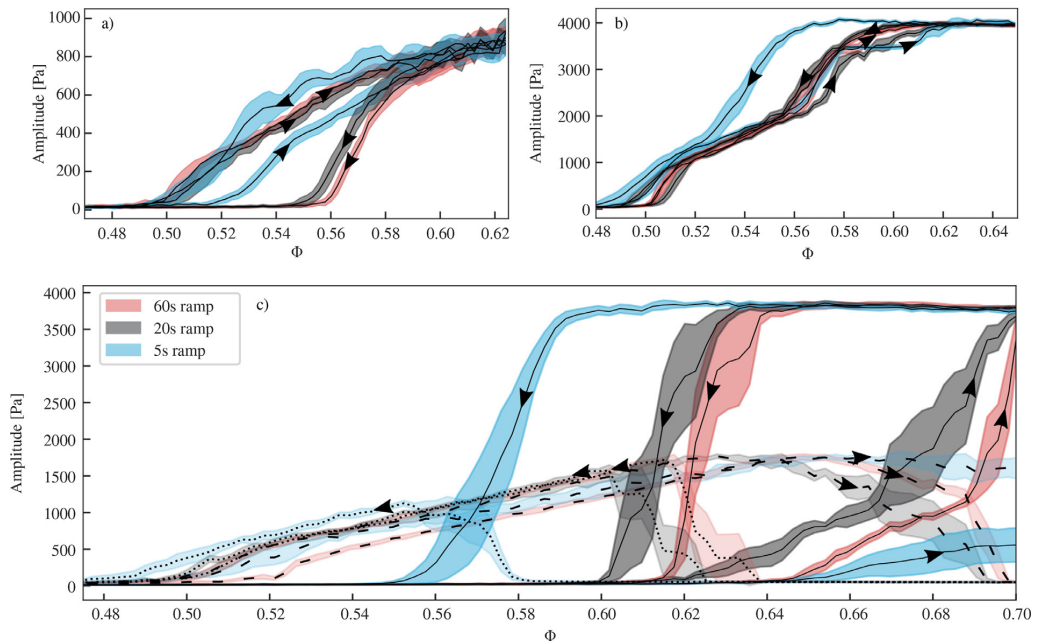
Fig. A.9. Mean amplitude (line) and standard deviation (shaded) during the ramping procedure at (a) P=4 kW, (b) P=8 kW and (c) P=6 kW for three different ramp times (5 s ▬, 20 s ▬ and 60 s ▬) and both directions. Arrowheads indicate the ramp direction. In (c) solid lines correspond the mode at f_3=1330–1370 Hz and the dashed (increasing Φ) and dotted (decreasing Φ) lines to the mode at f_2=1100–1150 Hz. Each data set corresponds to 7 ramps per ramp time and direction. (For interpretation of the references to color in this figure legend, the reader is referred to the web version of this article.)

in the hysteresis between the fast and slow ramp sequences. During the fast upward and downward ramps, A remains higher on the downward ramp relative to the upward ramp resulting in a small reduction in the stability range. This type of hysteresis, where the downward ramp reduces the operating limits relative to the upward ramp, has been observed previously in a number of single flame or Rijke tube experiments [3,25,33,34] and will be referred to as positive hysteresis, which can happen during transient varia-

tion of the bifurcation parameter, not only for subcritical Hopf bifurcations but also for supercritical ones as it was shown in [33].

Surprisingly, a different behavior is observed for the slower ramps which show that the downward ramps increase the stability limits relative to the upward ramps (negative hysteresis). During the slow upward ramps the system becomes unstable at around Φ = 0.5 whilst slow downward ramps reach stable conditions between Φ = 0.55 and 0.56. This type of hysteresis behaviour, where

the down ramp increases the stability limits compared to the up-ward ramp, differs from previously reported behaviour and to the best of the authors knowledge, this is the first time this type of hysteresis behaviour has been observed in flames.

Different behaviour is observed for the 8 kW cases as shown in Fig. A.9(b). Overall, they feature weaker hysteresis than the 4 kW cases but have instability amplitudes 4 times greater. Generally, two different hysteresis regions exist. One at lower A between $\Phi = 0.48$ and 0.52 and a second one at higher A between $\Phi = 0.56$ and 0.62. Focusing on the longer 20 and 60 s ramp sequences first, positive hysteresis is observed for both ramp times in the higher Φ region. However the extents of these hysteresis regions differs with the 60 s ramps exhibiting a very weak hysteresis. Below approximately $\Phi = 0.6$, the slow downward ramps do not exhibit hysteresis as shown by the collapse in both ramping directions. However, below $\Phi = 0.52$ and when A drops below 1000 Pa, the 20 s ramp shows a second positive hysteresis. The fast ramp sequences exhibit different behaviour. A large positive hysteresis, is present on the downward ramp, occurring between $\Phi = 0.52$ and 0.62. This corresponds to the observed plateau where the high amplitude standing mode occurs during the ramp up, which is not present during the ramp down.

Figure A.9 (c) plots the stability limits for the 6 kW ramping sequences where the frequency jump occurs from f_2 to f_3 due to the change in the mode from 1A2L to 1A3L denoted by the broken and solid lines respectively. A larger plot is used due to the extra complexity in the hysteresis behaviour due to the presence of the frequency/mode hop. The upward ramps show the 1A2L mode becomes unstable between $\Phi = 0.5$ and 0.52 and grows linearly for all three ramp speeds. The mode/frequency hop occurs between $\Phi = 0.62$ and 0.68 which shows both an increase in A of the 1A3L mode with a simultaneous decrease of A in the 1A2L mode. As soon as the amplitude of the 1A3L mode surpasses the amplitude of 1A2L, it rapidly increases to limit-cycle conditions. Strong positive hysteresis effects for the 1A3L mode are observed for all ramp speeds. The 1A3L mode maintains its high-amplitude limit-cycle over a larger range of operating conditions for decreasing ramp time. The complex interaction between the two modes shows that the decay in the 1A3L mode coincides with the reestablishment and growth of the 1A2L mode but the interval where both modes coexist is considerably shortened during the ramp down. The amplitude of the 1A2L mode then decays in a linear manner exhibiting considerably smaller hysteresis than the high amplitude 1A3L mode.

This type of hysteresis involving switch from one mode to another is typical of dynamic flame non-linearities induced by a flame response to acoustic perturbation that has a delay which depends on the oscillation amplitude. Such situation was investigated in [33] using a describing function analysis and is in line with the change of mean flame length that is observed in the present experiments as explained in the last section.

Overall, the longer ramp sequences of 20 s and 60 s show similar bifurcation points and hysteresis behaviour. The short ramp sequence 5 s shows a different bifurcation point and hysteresis behaviour. A potential explanation may be a time-scale effect related to thermal inertia of the combustor which is sensitive to the rate of change of temperature, such that at suitably fast ramp times the thermal inertial time-scale is much slower then the time scale of the equivalence ratio ramp. We note this is a conjecture and a larger range of ramp times are needed to further elucidate the dominant mechanisms at play.

6. Hysteresis of the nature and orientation angle

The hysteresis phenomenon is also manifested in θ and χ. First, the 4 kW cases are investigated in Fig. A.10. In terms of

χ, the slowest upward ramps transition from a standing mode to a switching spinning mode where χ oscillates between either spinning directions. From this periodically switching state, the mode evolves to stable spinning mode occurring for a short time around $\Phi = 0.55$ (see $t=119$–123 s in Fig. A.5) before returning to a switching spinning mode. During faster ramps up, the switching mode tends to be replaced by a CW mixed mode, and the transition to a switching mode always occurs but tends to be delayed to higher Φ. The hysteresis on the downward ramp shows a direct transition from the switching mode to stable bypassing the occurrence of the CW spinning mode. Except for the differences in the amplitudes, θ and χ follow the same path for all downward ramp times for decreasing Φ until stable conditions are reached.

The nodal line position shown on the right hand side of Fig. A.10 follows clear, repeatable trends for all of the seven runs, with small differences in the 5 s, which clearly indicates the presence of weak symmetry breaking in the system, due to small asymmetries in the geometry, the cooling system, the flow or the flame shapes for example.

In absence of switching modes, a very clear and reproducible path for both θ and χ is observed (see Fig. A.11) for all ramping sequences when the power is increased to 8 kW. The unstable modes show that on upward ramps standing modes become unstable as the amplitude grows and saturate to spinning modes. Figure A.11 also shows that the ramp time affects the saturation to spinning modes which occurs at lower Φ for decreasing upward ramp times. The opposite trend is observed for downward ramps. The orientation angle also closely follows the trends in χ.

While the 4 kW cases showed a clear tendency towards CW spinning modes, both spinning directions are observed for the 8 kW cases. The standing and the spinning mode do have the same preferred θ as the switching mode reported earlier: $\Theta = 60°$ is positioned on a burner for the standing mode and $\Theta = 135°$ positioned in between two burners for the spinning modes. Joint PDFs of θ and χ for the 6 kW cases are not presented here for brevity. Defined trends for θ and χ were observed when either of the two unstable modes were present. However, no discernible trends were observed during the coexistence of two modes.

7. Mode hopping

We now further investigate the mode hopping from the 1A2L to the 1A3L mode which occurs during the 6 kW ramps by investigating the flame dynamics. An additional measurement campaign was undertaken to obtain high-speed OH* chemiluminescence imaging at 10 kHz to provide side views of the flame as shown in Figs. A.12 and A.13. To provide optical access, a shorter version of the outer wall was placed on top of a short quartz segment. This will slightly change the thermal state but the modal behaviour and amplitude for the self-excited modes was found to be repeatable and closely matched the cooled-wall behaviour presented in previous sections. It is therefore reasonable to expect that the resulting flame dynamics are representative of the mode hopping.
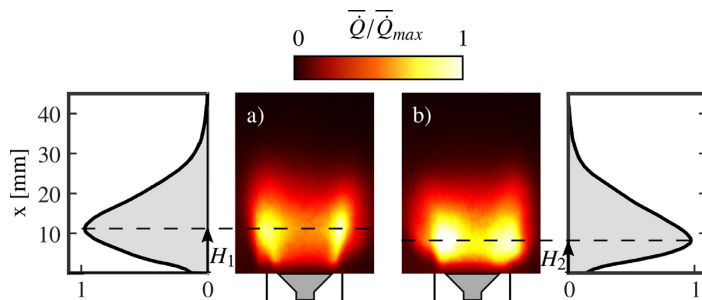
The mean flame shapes for $\Phi = 0.65$ and 0.7 are shown in Fig. A.12 corresponding to a 1A2L CCW spinning and a 1A3L CW spinning mode respectively. As Φ is increased, it is accompanied by an increase in flame temperature as well as heat transfer to the bluff body which causes the mode to hop from the 1A2L mode to the 1A3L mode. This more than doubles the acoustic velocity amplitude, $u'/\langle U \rangle = 0.3$ to 0.65 evaluated from the multiple microphone method. This leads to a significant change in the mean flame shape and therefore the phase response of the flame. This is supported by the fact that the 1A3L mode is the only mode excited when the power is increased to 8kW (see Fig. A.4). The flame shape for the 1A2L mode is anchored at the edge of the bluff body with distinct flame brushes depicted by the elongated
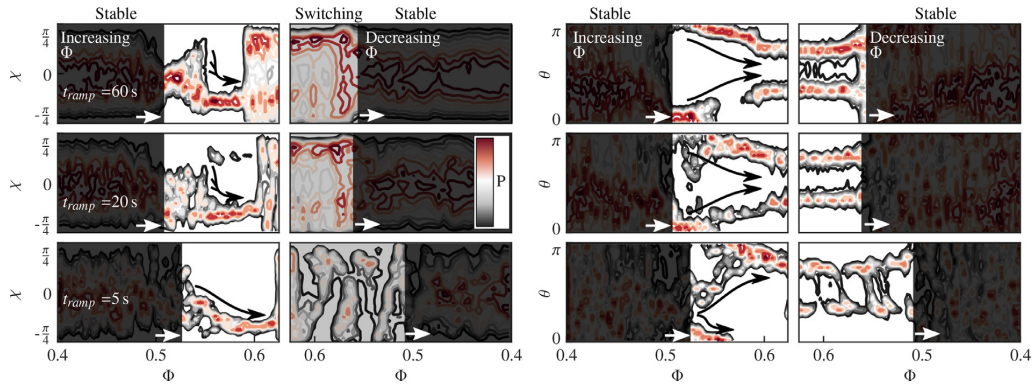
Fig. A.10. Comparison of the joint PDFs of the nature and orientation angle for different ramping speeds and directions at P=4 kW. Each graph corresponds to 7 ramps. The first two columns represent the nature angle for increasing and decreasing equivalence ratio. The orientation angle is shown in the 3rd (increasing Φ) and 4th column (decreasing Φ). The ramp times are 60 s (1st row), 20 s (2nd row) and 5 s (3rd row). The region where the amplitude is below 100 Pa is masked.
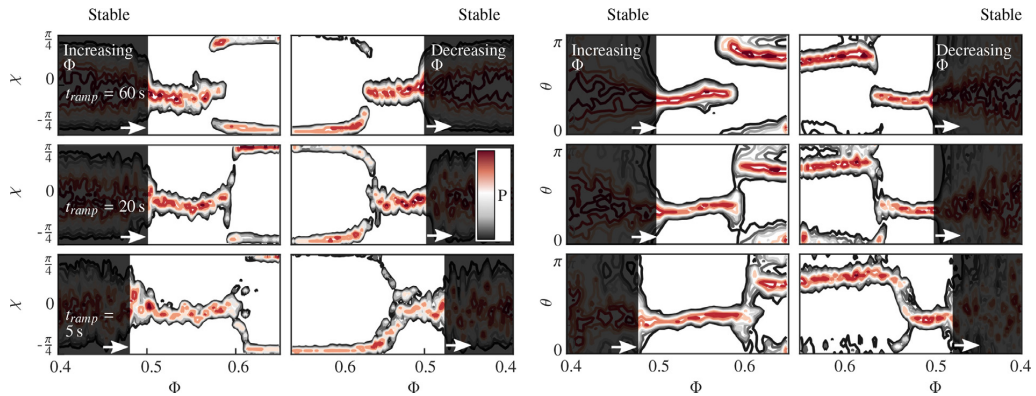
Fig. A.11. Comparison of the joint PDFs of the nature and orientation angle for different ramping speeds and directions at P=8 kW. Each graph corresponds to 7 ramps. The first two columns represent the nature angle for increasing and decreasing equivalence ratio. The orientation angle is shown in the 3rd (increasing Φ) and 4th column (decreasing Φ). The ramp times are 60 s (1st row), 20 s (2nd row) and 5 s (3^{rdxs} row). The region where the amplitude is below 100 Pa is masked.


Fig. A.12. Images of the mean flame shape at P=6 kW for $\Phi = 0.65$ (a) and $\Phi = 0.7$ (b) with the stream-wise distribution of heat release rate.

yellow to white regions. The mean flame shape of the 1A3L mode is distinctly different in two main ways: firstly, the flame is more compact and secondly, the heat release rate is more distributed as shown by the increase in OH* intensity in the wake region (reduced gradient of OH* across the flame). Comparing the stream-wise distribution of the integrated heat release rate (grey plots on the adjacent sides of the mean flame images) shows that the location of peak heat release rate has moved upstream. It is plausible to assume that this change in the flame shape will induce changes

to the FTF delay. The shorter time-lag leads to the higher frequency instability associated with the higher longitudinal mode. It is important to note that the 1A3L mode is approaching the flashback condition $\Phi = 0.72$.

The phase-averaged flame response over the limit cycles for each mode are plotted in Fig. A.13. The azimuthal spinning directions are indicated by the white arrows. Also, note that the flame is completely isolated from neighbouring flames (no flame-flame interaction) and oscillates strongly in axial direction for both
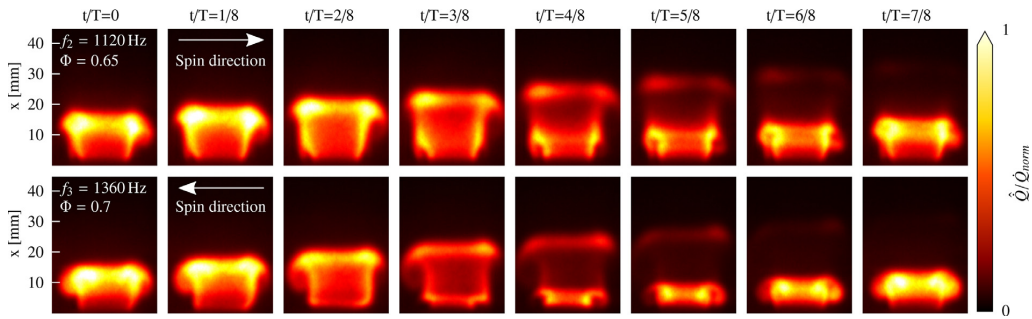
Fig. A.13. Phase averaged OH* chemiluminescence from the side at $\Theta = 0$, at $P = 6$ kW. The data was gathered during single runs at the specified Φ and the phase averages are based on 7000 images. $\dot{Q}_{norm} = 0.9 \dot{Q}_{max}$.

operating conditions. In both cases, asymmetries in the flame response are shown relative to the direction of the azimuthal modes, which results in slight tilting to the right in the CCW direction for $\Phi = 0.65$ and to the left in the CW direction for $\Phi = 0.7$ as shown previously in [35]. For the 1A2L mode, this results in asymmetric shedding of the top part of the flame brush between $t/T = 3/8$ to $t/T = 5/8$ with increased $\dot{Q}$ on the left hand side of the flame relative to the right hand side. The latter four panels also show a more pronounced flame roll-up on the left hand side relative to the right hand side.

Overall, similar dynamics of the 1A3L mode are observed but with some differences. Most notable is the flame roll-up process at $t/T = 4/8$ to $t/T = 5/8$ which occurs closer to the bluff body resulting from the reduced time-lag associated with the increased frequency of the longitudinal component. Since the flame is close to flashback conditions, it almost propagates back into the injector pipe as shown by the low value levels of $\dot{Q}$ at $t/T = 3/8$. The asymmetric flame response of the flame due to the CW spinning mode is shown by slight tilting to the left hand side and the slight advancing of $\dot{Q}$ on the right hand side. Due to the increased compactness and more distributed flame the peak values of $\dot{Q}$ are closer to the bluff-body as found in the mean flame shape.

8. Conclusion

This work presents experimental observations during equivalence ratio ramps in an annular combustion chamber. Exhibiting self-sustained azimuthal combustion instabilities the system features phenomena that can only partially be explained by existing models in the literature or have not been reported before. The presented data condenses to several key observations:

- Both positive and negative hysteresis in terms of the amplitude during equivalence ratio ramps are observed. Thereby, the negative hysteresis phenomenon increased the stability range of the combustor, while the positive hysteresis decreased it. Generally, the hysteresis phenomena are heavily dependent on the ramping speed and direction, as well as the power the burner is operated at. In all cases, reducing the ramping time increased the amplitude difference between the upwards and the downwards ramps.
- A quasi-periodically switching spinning mode leading to beating of the acoustic signals amplitude is observed. The joint PDFs show a very repetitive but slightly asymmetric pattern.
- Though the study features a nominally symmetric setup, the anti-nodal line location of the standing component follows a clear, repeatable pattern path. The system clearly exhibits two preferred nodal line positions. This indicates that even nominally symmetric combustor can exhibit small asymmetries that

do alter and can dominate the response of the system. The source of the asymmetry remains unknown.
- At the largest equivalence ratio (and amplitude, far from the bifurcation) only spinning modes (switching for 4 kW) were observed while low amplitude instabilities close to the bifurcation tend to exhibit dynamics around a standing mode.
- For 6 kW case, a small increase in equivalence ratio resulted in the 1A2L mode hopping to the slightly higher frequency 1A3L mode. This was accompanied by more than a doubling of the acoustic velocity amplitude which modified the mean flame shape by making it more compact. A possible explanation is that this length change has the effect of inducing a change in the FTF delay and the linear stability of the system to favour the 3L longitudinal component of the mode.

This work provides a valuable experimental data set with several interesting phenomena that are related to modal dynamics in annular combustors under transient operation.

Declaration of Competing Interest

The authors declare that they have no known competing financial interests or personal relationships that could have appeared to influence the work reported in this paper.

Acknowledgements

Appendix A. Calculation of the slow-flow variables

This section aims to shed light onto the post processing routine to calculate the slow flow variables.

We take the three azimuthally distributed pressure signals $p_{0,1}$, $p_{1,1}$ and $p_{2,1}$ as a starting point and use a FFT to determine the dominant mode. This is without exception the mode with azimuthal mode order $n = 1$ in the present work. Each pressure time series is then bandpass-filtered with a bandpass width of $\Delta f = 100$ Hz around the corresponding peak frequency f to remove noise components.

The spatial pressure field $p(\Theta, t)$ is 2π-periodic because of the annular shape of the chamber. It can therefore be written as a Fourier series for the azimuthal coordinate Θ, and this series is truncated to the 1st order terms because the filtering allowed us

to get rid of the higher order components:

$$p(\Theta, t) = \xi_1(t) \cos(\Theta) + \xi_2(t) \sin(\Theta). \tag{A.1}$$

The projected signals ξ_1 and ξ_2 are obtained from the filtered microphone timetraces by inverting the system

$$\begin{bmatrix} p_{0,1} \\ p_{1,1} \\ p_{2,1} \end{bmatrix} = \begin{bmatrix} \cos(\Theta_0) & \sin(\Theta_0) \\ \cos(\Theta_1) & \sin(\Theta_1) \\ \cos(\Theta_2) & \sin(\Theta_2) \end{bmatrix} \begin{bmatrix} \xi_1 \\ \xi_2 \end{bmatrix} \tag{A.2}$$

where Θ describes the azimuthal position of the microphones. In the present study $\Theta_0 = 0$, $\Theta_1 = 2\pi/3$ and $\Theta_2 = 4\pi/3$. This system is overdetermined and is inverted in a least square sense. The corresponding complex analytic signals of ξ_1 and ξ_2 are

$$\xi_{a,1}(t) = \xi_1(t) + j\mathcal{H}(\xi_1(t)) \ \ \xi_{a,2}(t) = \xi_2(t) + j\mathcal{H}(\xi_2(t)) \tag{A.3}$$

where $\mathcal{H}$ is the Hilbert transform and j the second quaternion imaginary unit. The quaternion analytic signal of $\xi(t)$ is defined as

$$\begin{aligned} \xi_a(t) &= \xi_{a,1} + i\xi_{a,2} \\ &= \xi_1 + i\xi_2 + j\mathcal{H}(\xi_1(t)) + k\mathcal{H}(\xi_2(t)) \end{aligned} \tag{A.4}$$

with i, j, k as the quaternion imaginary units. From this point, the slow-flow variables A, χ, θ, φ are extracted from ξ_a with the method presented in the appendix of [30].

Supplementary material

Supplementary material associated with this article can be found, in the online version, at doi:10.1016/j.combustflame.2020.10.013.

References

[1] M.R. Bothien, A. Ciani, J.P. Wood, G. Fruechtel, Toward decarbonized power generation with gas turbines by using sequential combustion for burning hydrogen, J. Eng. Gas Turb. Power 141 (2019) 121013.
[2] G. Glenk, S. Reichelstein, Economics of converting renewable power to hydrogen, Nat. Energy 4 (2019) 216–222.
[3] T. Lieuwen, V. Yang, Combustion Instabilities In Gas Turbine Engines: Operational Experience, Fundamental Mechanisms, and Modeling, American Institute of Aeronautics and Astronautics, Inc., 2005.
[4] T. Poinsot, Prediction and control of combustion instabilities in real engines, Proc. Combust. Inst. 36 (2017) 1–28.
[5] W. Krebs, P. Flohr, B. Prade, S. Hoffmann, Thermoacoustic stability chart for high intensity gas turbine combustion systems, Combust. Sci. Tech. 174 (2002) 99–128.
[6] J.R. Seume, N. Vortmeyer, W. Krause, J. Hermann, C.-C. Hantschk, P. Zangl, S. Gleis, D. Vortmeyer, A. Orthmann, Application of active combustion instability control to a heavy duty gas turbine, J. Eng. Gas Turb. Power 120 (1998) 721–726.
[7] N. Noiray, B. Schuermans, On the dynamic nature of azimuthal thermoacoustic modes in annular gas turbine combustion chambers, Proc. R. Soc. A-Math. Phys. 469 (2013) 20120535.
[8] N.A. Worth, J.R. Dawson, Modal dynamics of self-excited azimuthal instabilities in an annular combustion chamber, Combust. Flame 160 (2013) 2476–2489.
[9] N.A. Worth, J.R. Dawson, Self-excited circumferential instabilities in a model annular gas turbine combustor: Global flame dynamics, Proc. Combust. Inst. 34 (2013) 3127–3134.
[10] J.-F. Bourgouin, D. Durox, J.P. Moeck, T. Schuller, S. Candel, Self-sustained instabilities in an annular combustor coupled by azimuthal and longitudinal acoustic modes, ASME Turbo Expo (2013) Paper No: GT2013–95010.
[11] P. Wolf, G. Staffelbach, L.Y. Gicquel, J.-D. Müller, T. Poinsot, Acoustic and large eddy simulation studies of azimuthal modes in annular combustion chambers, Combust. Flame 159 (2012) 3398–3413.
[12] J.-F. Bourgouin, D. Durox, J.P. Moeck, T. Schuller, S. Candel, Characterization and modeling of a spinning thermoacoustic instability in an annular combustor equipped with multiple matrix injectors, J. Eng. Gas Turb. Power 137 (2014) 021503.
[13] A. Faure-Beaulieu, T. Indlekofer, J.R. Dawson, N. Noiray, Experiments and low-order modelling of intermittent transitions between clockwise and anticlockwise spinning thermoacoustic modes in annular combustors, Proc. Combust. Inst. (2020), doi:10.1016/j.proci.2020.05.008.
[14] M. Bauerheim, M. Cazalens, T. Poinsot, A theoretical study of mean azimuthal flow and asymmetry effects on thermo-acoustic modes in annular combustors, Proc. Combust. Inst. 35 (2015) 3219–3227.
[15] A. Morgans, S. Stow, Model-based control of combustion instabilities in annular combustors, Combust. Flame 150 (2007) 380–399.
[16] M. Bauerheim, P. Salas, F. Nicoud, T. Poinsot, Symmetry breaking of azimuthal thermo-acoustic modes in annular cavities: a theoretical study, J. Fluid Mech. 760 (2014) 431–465.
[17] P. Berenbrink, S. Hoffmann, Suppression of dynamic combustion instabilities by passive and active means, ASME Turbo Expo (2000) Paper No: 2000-GT-0079.
[18] N. Noiray, M. Bothien, B. Schuermans, Investigation of azimuthal staging concepts in annular gas turbines, Combust. Theor. Model. 15 (2011) 585–606.
[19] J.P. Moeck, M. Paul, C.O. Paschereit, Thermoacoustic instabilities in an annular Rijke tube, ASME Turbo Expo (2010) Paper No: GT2010–23577.
[20] J.R. Dawson, N.A. Worth, The effect of baffles on self-excited azimuthal modes in an annular combustor, Proc. Combust. Inst. 35 (2015) 3283–3290.
[21] G. Ghirardo, M.P. Juniper, J.P. Moeck, Weakly nonlinear analysis of thermoacoustic instabilities in annular combustors, J. Fluid Mech. 805 (2016) 52–87.
[22] T.C. Lieuwen, Experimental investigation of limit-cycle oscillations in an unstable gas turbine combustor, J. Propul. Power. 18 (2002) 61–67.
[23] P. Knoop, F. Culick, E. Zukoski, Extension of the stability of motions in a combustion chamber by nonlinear active control based on hysteresis, Combust. Sci. Tech. 123 (1997) 363–376.
[24] S. Manikandan, R. Sujith, Rate dependent transition to thermoacoustic instability via intermittency in a turbulent afterburner, Exp. Therm. Fluid Sci. 114 (2020) 110046.
[25] G. Bonciolini, N. Noiray, Bifurcation dodge: avoidance of a thermoacoustic instability under transient operation, Nonlinear Dyn. 96 (2019) 703–716.
[26] G. Bonciolini, D. Ebi, U. Doll, M. Weilenmann, N. Noiray, Effect of wall thermal inertia upon transient thermoacoustic dynamics of a swirl-stabilized flame, Proc. Combust. Inst. 37 (2019) 5351–5358.
[27] W. Culler, X. Chen, J. Samarasinghe, S. Peluso, D. Santavicca, J. O'Connor, The effect of variable fuel staging transients on self-excited instabilities in a multiple-nozzle combustor, Combust. Flame 194 (2018) 472–484.
[28] K. Prieur, D. Durox, T. Schuller, S. Candel, A hysteresis phenomenon leading to spinning or standing azimuthal instabilities in an annular combustor, Combust. Flame 175 (2017) 283–291.
[29] M. Mazur, H.T. Nygård, J.R. Dawson, N.A. Worth, Characteristics of self-excited spinning azimuthal modes in an annular combustor with turbulent premixed bluff-body flames, Proc. Combust. Inst. 37 (2019) 5129–5136.
[30] G. Ghirardo, M.R. Bothien, Quaternion structure of azimuthal instabilities, Phys. Rev. Fluids 3 (2018) 113202.
[31] JulHoltz, Julia package for handling various wave equations and (nonlinear) eigenvalue problems. https://github.com/JulHoltzDevelopers/WavesAndEigenvalues.jl.
[32] D. Laera, T. Schuller, K. Prieur, D. Durox, S.M. Camporeale, S. Candel, Flame describing function analysis of spinning and standing modes in an annular combustor and comparison with experiments, Combust. Flame 184 (2017) 136–152.
[33] G. Bonciolini, D. Ebi, E. Boujo, N. Noiray, Experiments and modelling of rate-dependent transition delay in a stochastic subcritical bifurcation, R. Soc. Open Sci. 5 (2018) 172078.
[34] E.A. Gopalakrishnan, R.I. Sujith, Effect of external noise on the hysteresis characteristics of a thermoacoustic system, J. Fluid Mech. 776 (2015) 334–353.
[35] J.R. Dawson, N.A. Worth, Flame dynamics and unsteady heat release rate of self-excited azimuthal modes in an annular combustor, Combust. Flame 161 (2014) 2565–2578.

Transient thermoacoustic responses of methane/hydrogen flames in a pressurized annular combustor

Byeonguk Ahn, Thomas Indlekofer, James R. Dawson
and Nicholas A. Worth

Accepted for publication at
ASME Turbo Expo 2021

This article is not included due to copyright